

DEVELOPING HIGH-CAPACITY COMPOSITE ADSORBENTS FOR GOLD MILL PROCESSES

Ahmad Sadeghi Chevinli

A Thesis

in the Department of
Chemical and Materials Engineering

Presented in Partial Fulfillment
of the Requirements for the Degree of
Master of Applied Science (Chemical Engineering)

Concordia University
Montreal, Quebec, Canada

August 2023

© Ahmad Sadeghi Chevinli, 2023

CONCORDIA UNIVERSITY
School of Graduate Studies

This is to certify that the thesis prepared

By: Ahmad Sadeghi Chevinli

Entitled: **Developing high-capacity composite adsorbents for gold mill processes**

and submitted in partial fulfillment of the requirements for the degree of

Master of Applied Science (Chemical Engineering)

complies with the regulations of the University and meets the accepted standards with respect to originality and quality.

Signed by the final examining committee:

Supervisor, Dr. Zhibin Ye,
Department of Chemical and Materials Engineering

Examiner and Chair, Dr. Nhat Truong Nguyen,
Department of Chemical and Materials Engineering

Examiner, Dr.,
Department of Chemical and Materials Engineering

External Examiner, Dr. John Oh
Department of Chemistry and Biochemistry

Approved by

Graduate Program Director, Dr. Sana Jahanshahi-Anbuhi

Month day, year

Dean, Dr. Mourad Debbabi

Abstract

Developing high-capacity composite adsorbents for gold mill processes

Ahmad Sadeghi Chevinli

Addressing the existing problems in the gold mining industry, two types of high-capacity adsorbents have been developed to improve the economics and efficiency of the industrial gold extraction processes, as well as to reduce their environmental impact. In the first sub-project, high-performance lignin-polyethylene composite adsorbents have been developed for extraction of solubilized gold complexes from gold mill leaching solutions that show fast, high selectivity gold capturing from very low concentration of gold leachate solutions. In the second sub-project, high-capacity Mg–Fe layered double hydroxide-graphene oxide (LDH-GO) nanocomposite adsorbents have been developed to remove arsenic as a most toxic and carcinogenic element often present in gold sulfide ores, from gold mill effluent streams, to reduce both the adverse environmental impact of the gold mining activities and the environmental impact of the mining operations.

In our design of both types of composite adsorbents, we employ cost-effective active materials (lignin and magnesium/iron-based LDHs, respectively) of high adsorption capacity towards gold and arsenic species, respectively. Meanwhile, robust support/matrix materials (polyethylene and graphene oxide, respectively) are employed for the effective loading/encapsulation of the active materials. The composition and structure of both classes of composite adsorbents are tuned to achieve optimum adsorption performance. The adsorption properties of the composites have been evaluated towards the adsorption of gold and arsenic, respectively, from simulated waters under different conditions such as pH, contact time and initial concentration in batch process. The results show that the composites are highly effective in removing arsenic and capturing gold. The success of this research is expected to improve the economics and efficiency of the industrial gold extraction processes, and meanwhile make them safer and more environmentally responsible.

Acknowledgment

I would like to acknowledge my supervisor, Professor Zhibin Ye, for his role in overseeing my thesis project.

I would like to express my appreciation to my friend and labmate, Jalal Rahmatinejad. I am fortunate to have had him as a supportive colleague during this important phase of my academic career.

Throughout my academic career, my father has always supported, encouraged, and believed in me. Thank you, father, for everything you have done for me. Thanking my mom for all she has done for me.

Dedicated to the brave women of Iran.

#Woman_life-freedom

Dedication

Dedicated to the brave women of Iran.

#Woman_life-freedom

Contribution of Authors

Thesis format: This thesis is organized in a paper-based format. Chapter 3 and Chapter 4 are adapted, respectively, from the following two papers that are currently in the submission process.

- **Ahmad Sadeghi Chevinli**, J. Rahmatinejad, Denis Rodrigue, Nuri Hmidi, Zhibin Ye, “Lignin-Polyethylene Composite Adsorbents for Gold Capturing”. (under review)
- **Ahmad Sadeghi Chevinli**, J. Rahmatinejad, Nuri Hmidi, Denis Rodrigue, Zhibin Ye, “Mg–Fe Layered Double Hydroxide-Graphene Oxide Nanocomposite Adsorbents for Arsenic Removal”. (under review)

Declaration of Author Contributions:

Ahmad Sadeghi Chevinli (Main Author) was actively involved in designing and conducting experiments, analyzing results and data, and writing draft of research papers and the thesis.

Jalal Rahmatinejad (Second Author) played a crucial role as the second author of papers, primarily focusing on some characterizations of the synthesized composites (XRD, TGA, FTIR) in both projects.

Denis Rodrigue (Collaborative Member) contributed as a collaborative member by actively participating in the production of lignin-polyethylene composite adsorbents for the first project. Furthermore, his insights and meticulous review greatly enriched the quality of the papers.

Nuri Hamidi (Collaborative Member) provided valuable input as a collaborative member, assisting in shaping the project objective and formulating research questions.

Zhibin Ye (Supervisor) played a pivotal role as the supervisor of this thesis, offering guidance, expertise, and mentorship throughout its development. His supervisory support ensured the rigorous academic and methodological standards in this research.

In addition to the above papers, the following conference poster presentation was delivered on the basis of the results from the thesis.

- **Ahmad Sadeghi Chevinli**, J. Rahmatinejad, Zhibin Ye, “Layered Double Hydroxide-Graphene Oxide Nanocomposite Adsorbents for Arsenic Removal”, Canadian Chemistry Conference and Exhibition, Vancouver, Canada (CSC 2023)

All authors reviewed the final manuscript and approved of the contents.

Table of Contents

List of Figures	xi
List of Tables.....	xiv
Acronyms	xv
Chapter 1 Introduction.....	1
1.1 Background	1
1.2 Adsorbents for gold capturing from gold mill leaching solution	1
1.3 Adsorbents for arsenic removal from gold mill effluents	2
1.4 Thesis Outline.....	3
Chapter 2 Literature Review	4
2.1 Introduction.....	4
2.2 Gold mining.....	6
2.3 Adsorption.....	9
2.3.1 Adsorption Isotherm.....	10
2.3.1.1 Langmuir Isotherm	11
2.3.1.2 Freundlich Isotherm.....	12
2.3.1.3 Temkin Isotherm.....	12
2.3.2 Adsorption kinetics and mechanisms	13
2.3.2.1 Pseudo-first order model.....	14
2.3.2.2 Pseudo-second order model.....	15
2.3.2.3 Intra-particle diffusion model.....	16
2.3.2.4 Elovich.....	17
2.3.3 Adsorption parameters.....	17
2.3.3.1 Point of zero charge	18

2.3.3.2	Solution pH.....	18
2.3.3.3	Solution temperature	19
2.3.3.4	Adsorbent properties.....	20
2.3.4	Porous material adsorbents.....	21
2.4.	Arsenic	22
2.4.1	Arsenic Removal Methods	24
2.4.1.1	Adsorption and ion exchangers	25
2.4.2	Adsorbents.....	26
2.4.2.1	Activated Alumina.....	26
2.4.2.2	Titanium Oxides	27
2.4.2.3	Magnesium Oxides	27
2.4.2.4	Iron Oxide Nanostructures	29
2.4.2.5	Binary Metal Oxides.....	31
2.4.2.6	Layer Double Hydroxide Composites	33
2.4.2.7	Metal Organic Framework (MOF)	35
2.4.2.8	Graphene Oxide Composites	37
2.4.3	Challenges and Prospect of Adsorbents.....	41
Chapter 3 Lignin Polyethylene Composite Adsorbents for Gold Capturing		44
3.1	Abstract.....	44
3.2	Introduction.....	44
3.3	Experimental	46
3.3.1	Materials	46
3.3.2	Preparation of adsorbent pellet.....	46
3.3.3	Characterization.....	47
3.3.4	Gold adsorption.....	48

3.4	Result and Discussion.....	49
3.5	Conclusion	60
Chapter 4 Mg–Fe Layered Double Hydroxide-Graphene Oxide Nanocomposite		
Adsorbents for Arsenic Removal		62
4.1	Abstract.....	62
4.2	Introduction	63
4.3	Experimental Section	65
4.3.1	Chemicals and Materials	65
4.3.2	Synthesis of Graphene Oxide	65
4.3.3	Synthesis of nanocomposite adsorbents.....	66
4.3.4	Characterization.....	68
4.3.5	Arsenic adsorption.....	68
4.4	Result and discussion.....	70
4.4.1	Synthesis and Characterizations of Nanocomposite Adsorbents	70
4.4.2	Arsenic adsorption.....	77
4.5	Conclusion	85
Chapter 5 Conclusion		87
5.1	Project on lignin-PE composite adsorbents for gold capturing.....	87
5.2	Project on LDH-GO composite adsorbents for arsenic removal	88
References		91
Appendix		107

List of Figures

Figure 2-1: Schematic speciation of arsenic in oxidation states 5, 3, 0 and -3 in acidic and basic solutions [32].	23
Figure 2-2: Classification of different NMs used for water and wastewater treatment [39].	25
Figure 2-3: (a) Schematic illustration of the influence of annealing temperature on the structures of Mg(OH) ₂ -MgO@rGO nanocomposites (I) before and (II) after hydration. (b) As(III) sorption capacity of Mg(OH) ₂ -MgO@rGO nanocomposites as a function of the content of MgO (gMgO) and the annealing temperature (200-700 C) [57].	28
Figure 2-4: The schematic diagram for the synthesis of C-MgO micro-rods [59].	29
Figure 2-5: MgO-MnO ₂ synthesis schematic.	32
Figure 2-6: A schematic illustration of the As removal mechanism using a LDH.	35
Figure 2-7: adsorption kinetics and cycles result for As(V) and As (III) [81].	36
Figure 2-8: Major classification of graphitic materials [84].	37
Figure 2-9: Schematic synthesis of FeO _x -GO nanocomposites [86].	38
Figure 2-10: adsorption capacity of and FTIR spectra of (a) Fe-Mg (hydr)oxide (b) GO and (c) Fe-Mg (hydr)oxide@GO.	39
Figure 2-11: Fabrication process of MgO/GO [88].	40
Figure 2-12: Raman spectra obtained from pure GO and GO-Fe nanocomposite for 25, 35, 40, and 45 h [89].	40
Figure 2-13: XRD patterns: (a) Graphite and Graphene Oxide, (b) GO/MgO NCs for ratios 1:5, 1:1, and 5:1[91].	41
Figure 3-1: Schematic production of lignin-PE composite pellets and pellet dimensions.	47
Figure 3-2: Wide-angle XRD patterns of L40-PE60, pure lignin and PE.	50
Figure 3-3: FTIR spectra of L40-PE60, pure lignin and PE.	51
Figure 3-4: TGA curves for pure lignin, PE and pellet composites in the air atmosphere.	52
Figure 3-5: Gold adsorption capacity and capturing percentage for various adsorbents towards the adsorption of Au(III) at adsorbent dosage of 100 mg L ⁻¹ , Au(III) initial concentration of 515 mg L ⁻¹ and pH = 6.	53

Figure 3-6: Effects of dosage of L40-PE60 on the adsorption capacity and percent removal of Au(III) at initial Au(III) concentration of 12 mgL ⁻¹ Au(III) and pH 6.....	54
Figure 3-7: Effects of pH on the adsorption capacity and percent removal of Au(III) with L40-PE60 at initial Au(III) concentration of 6 mg L ⁻¹ and adsorbent dosage of 100 mg L ⁻¹ .	55
Figure 3-8: (a) Adsorption kinetics with L40-PE60 for Au(III) at initial Au(III) concentration of 10 mg L ⁻¹ , adsorbent dosage of 100 mg L ⁻¹ dosage, and pH of 6 and (b) fitting of the kinetic curves with the pseudo-second-order model.	56
Figure 3-9: (a) Adsorption isotherms of L40-PE60 for both Au(III) at pH 6, and (b) fitting with Freundlich model.....	58
Figure 3-10: First and second cycle gold adsorption by L40-PE60 in different initial concentration, 100 mg L ⁻¹ dosage and pH=6.	60
Figure 4-1: Schematic synthesis of LDH-GO, α-Fe ₂ O ₃ -GO, and Mg(OH) ₂ -GO nanocomposite adsorbents.	67
Figure 4-2: (a) Wide-angle XRD patterns, (b) FTIR spectra, (c) Raman spectra, (d) TGA curves and (e) differential curves, (f) N ₂ sorption isotherms, and (g) NLDFT meso-/macro-pore size distribution curves of GO and representative LDH-GO, α-Fe ₂ O ₃ -GO and Mg(OH) ₂ -GO composites.....	72
Figure 4-3: Transmission electron microscopy of GO (a, b,), F80-GO20 (c, d), M80-GO20 (e, f), and the LDH-GO composite LDH0.42-80-GO20 (g, h). Dark field scanning transmission electron microscopy (DF-STEM) image (i) and the corresponding C (j), O (k), Fe (l) and Mg (m) elemental maps of LDH0.42-80-GO20.....	77
Figure 4-4: Adsorption capacity for composites for As(III) and As(V) removal at adsorbent dosage of 1 mg mL ⁻¹ and pH of 6.8.	79
Figure 4-5: (a) Effects of the dosage of LDH0.42-80-GO20 on equilibrium adsorption capacity and percent removal of As(V) at the initial concentration of 248 mg L ⁻¹ ; (b) effects of pH on adsorption capacity of LDH0.42-80-GO20 towards As(III) and As(V) at the initial arsenic concentration of 141 mg L ⁻¹ and adsorbent dosage of 0.5 mg mL ⁻¹ ; (c) effects of pH on zeta potential of LDH0.42-80-GO20, F80-G20, and M80-GO20.	80
Figure 4-6: (a) Adsorption isotherms of LDH0.42-80-GO20 for both As(III) and As(V) at pH 6.8, and fitting with Freundlich model for (b) As(III) and (c) As(V).	82

Figure 4-7: (a) kinetic data for adsorption of As(III) and As(V) with LDH0.42-80-GO20 at initial arsenic concentration of 568 and 645 mg L⁻¹, respectively; (b) fitting of the kinetic curves with the pseudo-second-order model.....84

Figure 4-8: Residual arsenic concentration in the water containing different co-existing ions following adsorption with LDH0.42-80 -GO20 at the initial arsenic concentration of around 250 µg L⁻¹ at pH of 6.8 and co-existing anion concentration at 100 mg L⁻¹.....85

Figure A-1: Fitting of the adsorption kinetics of L40-PE60 with different kinetic models: (a) pseudo second order, (b) Elovich, (c) intraparticle diffusion, (d) pseudo first order models. The adsorption took place at initial Au(III) concentration of 10 mg L⁻¹, adsorbent dosage of 100 mg L⁻¹, and pH=6.8. 107

Figure A-2: Fitting of the adsorption isotherm of L40-PE60 toward Au(III) with different models: (a) Langmuir, (b) Freundlich, (c) Temkin. The isotherm was obtained at the adsorbent dosage of 100 mg L⁻¹ and pH of 6.8..... 109

Figure A-3: N₂ sorption isotherms of α-Fe₂O₃-GO (a), Mg(OH)₂-GO (c), LDH-GO composites (e, g) and their NLDFT meso-/macro-pore size distribution curves(b, d, f, h). 110

Figure A-4: Fittings of the As(III) adsorption isotherm of LDH0.42-80-GO20 with (a) Langmuir, (b) Freundlich, and (c) Temkin models..... 112

Figure A-5: Fittings of the As(V) adsorption isotherm of LDH0.42-80-GO20 with (a) Langmuir, (b) Freundlich, and (c) Temkin models..... 112

Figure A-6: Fitting of As(III) adsorption kinetics of LDH0.42-80-GO20 with (a) pseudo second order, (b) Elovich, (c) intraparticle diffusion, and (d) pseudo first order models. 114

Figure A-7: Fitting of As(V) adsorption kinetics of LDH0.42-80-GO20 with (a) pseudo second order, (b) Elovich, (c) intraparticle diffusion, and (d) pseudo first order models. 115

List of Tables

Table 2-1: Comparison of arsenate adsorption among prevalent adsorbents	43
Table 3-1: List of adsorption kinetic models.....	57
Table 3-2: List of adsorption isotherm models	58
Table 3-3: Effects of interfering metal ions on the adsorption capacity of L40-PE60 for Au(III).	59
Table 4-1: BET surface area, pore volume, and average pore size of representative composites and GO.....	75
Table 4-2: BET Comparison of maximum arsenic adsorption capacities reported for various nanocomposite adsorbents.....	82
Table A-1: Fitting parameters of Au(III) adsorption kinetic of L40-PE60 with different models	108
Table A-2: Fitting parameters of Au(III) adsorption isotherms with L40-PE60.....	108
Table A-3: BET surface area, adsorption capacity, and zeta potential of representative composites and GO.....	111
Table A-4: List of adsorption isotherm models.....	112
Table A-5: Fitting parameters of arsenic adsorption isotherms with LDH0.42-80-GO20..	112
Table A-6: List of adsorption kinetic models.	113
Table A-7: A summary of the fitting parameters of As adsorption kinetic with LDH0.42-80-GO20.....	113
Table A-8: Effects of interfering ions on the adsorption capacity of LDH0.42-80-GO20 for arsenic	115

Acronyms

As	Arsenic
BET	Braunauer-Emmett-Teller
CIL	Carbon-in-Leach
CIP	Carbon-in-Pulp
DI	Deionized water
FTIR	Fourier-Transformed Infrared
Au	Gold
GO	Graphene Oxide
ICP-MS	Inductively Coupled Plasma Mass Spectrometry
F	Iron Hydroxide
LDH	Layer Doubled Hydroxide
L	Lignin
M	Magnesium Hydroxide
PE	Polyethylene
pH	Potential of Hydrogen
TGA	Thermogravimetric Analysis
XRD	Wide-angle X-ray Diffraction

Chapter 1 Introduction

1.1 Background

Gold is the most economically important mined mineral in Canada with a production value of \$13.7 billion in 2021. Canada was the fourth-largest global producer of gold in 2021 with 223 tonnes produced by Canadian miners. A total of 223 tonnes of gold was produced by Canadian mines in 2021, an increase of 98% over gold production in 2012 and a 29% increase over gold production in 2020 [1]. Economic, efficient, yet safe and environmentally responsible gold extraction is vital to Canada's dynamic economy and environment, as well as the global competitiveness of Canada's gold mining industries. Adsorption, as an important unit operation, is widely used in the industrial gold extraction processes and plays a crucial role in determining the efficiency, economics, and environmental safety of the industrial processes. In the first project, adsorbent pellets are used for the capture of solubilized gold complex leached from gold ores in the leaching. In second project, adsorbents are used extensively for the removal of arsenic from gold mill effluents before their discharge into the environment, in both projects, developing advanced adsorbent technologies of improved performance and high capacity is key to improve the existing adsorption processes.

1.2 Adsorbents for gold capturing from gold mill leaching solution

Conventional industrial gold extraction processes often employ coarse particles of activated carbon as the adsorbents for capturing solubilized gold complex leached from gold ores with a cyanide solution. This is followed by stripping of the gold cyanide complex from the adsorbents, collected by screening, in a stripping column by contacting them with a hot caustic solution to render a concentrated gold solution for ultimate recovery by electrowinning. However, activated carbon is brittle and susceptible to attrition, generating

carbon fines within the process. This is problematic as the carbon fines are often laden with gold and can end up passing through screens to the tailings, resulting in a loss of gold. Furthermore, the presence of carbon fines in the stripping column will also plug the column and make the stripping process inoperable, thus requiring more expensive smelting process for ultimate gold recovery by incineration of the carbon [2].

To avoid the problem with activated carbon, surface-functionalized polystyrene beads, which are produced by chemical treatment of raw polystyrene beads, have also been developed for gold cyanide adsorption [3]. Though abrasion resistant with better selectivity, these functionalized polystyrene beads are more expensive compared to activated carbon and are restricted mainly for applications at low temperatures (60-70 °C) to avoid loss of functional groups. Recently, polystyrene beads coated with activated carbon on the surface have been further developed [2]. However, due to the low content of activated carbon on the surface, gold adsorption capacity of such beads is quite low. Meanwhile, because of the low softening temperature of polystyrene (around 100 °C), agglomeration of the beads tends to occur easily in the stripping column that is often operated at about 100-150 °C for fast stripping, leading to clogging of the column and burying of the gold-containing carbon fines within the beads; so the outcome is gold loss and low reusability of the beads.

1.3 Adsorbents for arsenic removal from gold mill effluents

Arsenic is a common, relatively abundant element in the earth's crust and is frequently a significant component in gold-containing sulfide ores [4]. Due to this, arsenic is often present in industrial gold mill wastewater [5]. Arsenic is one of the most toxic and carcinogenic elements, and is classified in Group 1 of the Priority Substances List by Health Canada [6]. With the increasingly stringent environmental regulations, the capture and safe disposal of arsenic present in gold mill effluents before their release to the environment is

critical for the mining industry to comply with the government regulations and to lessen the environmental impact of the mining activities. Among various techniques for arsenic removal, adsorption is most economical and efficient especially in the low concentration range [7]. Among the various adsorbents developed, iron oxide-based adsorbents in particular have been most attractive due to their high affinity towards arsenic[8]. However, existing iron oxide-based adsorbents often have various complications, such as high cost, low adsorption capacity, low arsenic selectivity, difficulty in separation, etc. In 2015, Developing low-cost high-capacity adsorbents featured with ease in separation, high arsenic adsorption capacity, and high selectivity has been an important drive-in industry for cost-saving and environmental reasons.

1.4 Thesis Outline

The general objective of the project is to develop high-capacity adsorbents of improved performance for applications in industrial gold mill processes, which will lead to improved efficiency, economics, and the environmental safety of the industrial processes. Two sub-projects are defined: one will target at developing high-performance lignin-polyethylene composite adsorbents for the adsorption of solubilized gold complexes from gold mill leaching solutions, while the other will target at developing high-capacity LDH-graphene oxide nanocomposite adsorbents for arsenic removal from gold mill effluents.

Chapter 2 Literature Review

This chapter examines and investigates the recent research on the adsorption of gold and arsenic. The purpose of this study is to gain a thorough understanding of the mechanisms and factors that affect gold and arsenic adsorption. The methods used in these investigations range from theoretical models to experimental methods. Several adsorbents have also been evaluated for their efficiency in gold and arsenic cleanup and their potential application. A critical analysis of the existing research will help us identify knowledge gaps and possible areas for future research, thereby advancing gold and arsenic adsorption science.

2.1 Introduction

Gold, a chemical element with the symbol Au and atomic number 79, is one of the most precious and valuable metals in the world. Its unique properties and versatility make it a sought-after material in a variety of industries, including electronics, medicine, jewelry, and finance. The demand for gold has grown significantly in recent years, driven by a range of factors, including geopolitical risks, economic growth, and increasing interest in gold as an investment. The price of gold is a key factor in determining its demand, with changes in price affecting both consumers and producers of gold. The price of gold is influenced by a range of factors, including supply and demand dynamics, geopolitical risks, and monetary policy [1]. When demand for gold is high, prices tend to rise, and when demand is low, prices tend to fall. However, the supply of gold is also an important factor in determining its price, with gold mining taking place on both small and large scales in countries around the world. The gold mining industry faces a range of challenges, including declining ore grades, increased regulation and environmental concerns, and rising costs. The declining ore grades mean that the amount of gold contained in each tonne of ore is decreasing, making it more difficult

and expensive to extract the metal. The increased regulation and environmental concerns mean that gold mining companies must navigate a complex and rapidly evolving regulatory landscape, while also taking steps to reduce their environmental impact. Rising costs, including energy costs, labor costs, and the costs of equipment and supplies, are also putting pressure on gold mining companies. Despite these challenges, gold remains an important and valuable commodity, with growing demand for its unique properties and versatility [3]. Gold is a highly conductive metal, making it essential in electronics, particularly in the manufacture of computer components and other high-tech devices. Its resistance to corrosion and biocompatibility also makes it valuable in medical applications, such as in the production of dental implants and other medical devices. The combination of physical and chemical properties of gold, including its density, malleability, and ductility, make it a versatile material that can be used in a range of applications, from jewelry and coins to high-tech electronics and medical devices [1].

Capturing gold from ore is a challenging process, and new methods and technologies are constantly being developed to improve gold extraction and processing. It is often found in association with other metals such as copper, silver, and lead. The traditional method of gold extraction is cyanide leaching, which involves mixing crushed ore with a sodium cyanide solution to dissolve the gold. Other common methods for gold extraction include froth flotation and gravity separation, and new technologies, such as bioleaching and heap leaching, are being developed and tested to make gold extraction more efficient, sustainable, and environmentally friendly. In recent years, there has been a growing interest in alternative methods for gold extraction, including the use of bacteria to extract gold, and the use of renewable energy sources, such as solar power, to reduce the environmental impact of gold mining. The development of new technologies and methodologies for gold extraction will be an important factor in determining the future of the gold market and could help to overcome the challenges and limitations of traditional gold mining methods [2].

2.2 Gold mining

Gold mining and use have a history that is as old as human civilization. With the development of technology, numerous gold recovery techniques have been developed. Currently, cyanide and chloride leaching are the most popular techniques. Cyanide leaching is less prevalent than chloride leaching due to the toxicity of cyanide and its inefficiency in refractory ores and concentrates [9][10]. There are many unique physical and chemical properties associated with gold, as well as its original currency function and decorative value. The use of gold in high-tech industries today is widespread, including electronics, telecommunications, aerospace, chemical engineering, and medicine [11][12]. Gold consumption in high-tech industries will continue to increase in the future. In recent years, gold prices have increased steadily due to the increasing demand for natural gold resources and the decreasing supply. Due to its enormous economic value and prospective uses, recovering gold has always been a topic of attention. The recovery of gold employs a variety of techniques, including solvent exchange [13], adsorption [14], precipitation [15], and ionic resins [16]. Superior capacity, selectivity, and cost-effectiveness are still being developed, nevertheless [17]. The solubility of gold in natural fluids is minimal; nonetheless, complexation is caused by halides (such as chloride, bromide, and iodide), cyanide, sulphide, thiosulphate, thiocyanate, and natural organic matter (such as humic and fulvic acid). Additionally, Au(I) and Au(III) chloride complexes predominately exist in halide forms in high chloride concentration environments like the saline supergene waters prevalent in Australia [17]. High grade mines have a gold content of 10 g t^{-1} to 35 g t^{-1} and low-grade mines have a gold content of 4.5 g t^{-1} to 10 g t^{-1} . Gold milling is typically carried out by crushing, grinding, leaching, and adsorption, then by stripping, electrowinning, and recovering the gold. Mining can be done in open pits or underground. Crushing, grinding, gravity concentration, leaching, carbon elution, reactivation, electrowinning, refining, and cyanide destruction are some of the processes that go into the milling of gold. Jaw and cone

crushers are used to reduce the ore to the proper sizes before adding it to the grinding circuit. After crushing, the ore is crushed in rod or ball mills to release the gold particles in the following phase. Water and chemicals are introduced to the grinding circuit to ground the ore to the correct size for leaching [2].

The most common method of extracting gold is through cyanide leaching, which involves using a solution of sodium cyanide to extract gold from ore. Cyanide leaching is a commonly used method of extracting gold from ore. The process involves dissolving gold from ore or concentrate by mixing it with a cyanide solution. The cyanide reacts with the gold, forming a soluble gold-cyanide complex that can be easily separated from the rest of the ore. The cyanide leaching process can be carried out using several methods, including heap leaching, vat leaching, and agitation leaching. In heap leaching, the ore is piled into a heap and a cyanide solution is sprayed onto the heap, allowing the cyanide to percolate through the ore and dissolve the gold. In vat leaching, the ore is placed in large vats and cyanide solution is added, allowing the solution to circulate through the ore and dissolve the gold. In agitation leaching, the ore is finely ground and mixed with cyanide solution in tanks. Agitation is used to keep the ore and solution well mixed, and the gold is dissolved over time. Cyanide leaching is a widely used process for extracting gold because it is relatively low-cost and efficient. However, it is also potentially dangerous due to the toxicity of cyanide. The use of cyanide in mining operations is heavily regulated to minimize the risk of environmental and health impacts. Proper management and disposal of cyanide-containing waste is critical to minimize these risks. After the gold is dissolved, the solution is separated from the ore and the gold is recovered from the solution by several methods, including adsorption onto activated carbon, precipitation using zinc or aluminum, and electrowinning [2].

The amount of total lignin biomass was estimated to be about 300 billion tons in 2012. Around 20 billion tons of lignin are formed every year. Lignin is one of the three essential components from wood and one of the most abundant biopolymers next to cellulose and

chitin. The chemical structure of lignin is complex [18]. Only 2% of the lignin produced is used for uses that add value; the remainder is burned as fuel in the same businesses that produce it [19][20]. Lignin is a natural polymer derived from plant materials that is widely used in industrial biomass waste production [21]. During kraft pulping, the lignin is separate from the cellulose fibers. The cellulose that is generated from the pulping process is used for paper production, and the lignin and hemicellulose are recovered. Several technologies have been developed for separating lignin from black liquor over the past few years, and commercial quantities are readily available today. Methoxy, hydroxyl, carboxyl, and aldehyde groups are only a few of the functional groups that make up the complex three-dimensional aromatic structure of lignin. These characteristics of lignin indicate that it may be exploited as a potential adsorption material in the elimination of heavy metals from wastewater [22]. In actuality, heavy metal ions from aqueous effluents have been removed using lignin. In the past, lignin from wood was separated and combined with phenol to create lignophenol, which showed tremendous promise for the efficient recovery of Au(III). It was determined that using this industrial byproduct for the adsorptive recovery of precious metals, such as gold, would not only be an effective strategy for the potential recovery of this valuable metal but also offer a cost-effective and environmentally friendly way to transform the waste products of pulping industries into sorption active materials [23]. Based on surface characterization and metal ion adsorption, a quantitative and mechanistic description of the adsorption of the metal ions Cr (VI) [22] Pb(II), Cu(II), Cd(II), Zn(II), and Ni(II) on lignin was investigated. Due to their high adsorption capacities, lignin has the potential to be used as adsorbents to remove metals from water [24]. Ferric lignin was loaded onto PE film to create PE-FeLs, a novel iron-containing adsorbent that aimed to remove arsenic from polluted soils [25].

2.3 Adsorption

Adsorption is a process that involves the accumulation of a substance at the interface between two phases, namely the liquid-solid interface or gas-solid interface. The adsorbate is the substance that accumulates at the interface, while the adsorbent is the solid on which the adsorption process takes place. Physical adsorption, which is characterized by weak van der Waals forces between the adsorbates and the adsorbent, is reversible in most cases, while chemical adsorption, which is characterized by strong chemical associations between the molecules of the adsorbate and the adsorbent surface, is usually irreversible. The efficiency of physical adsorption is determined by the adsorption capacity of the adsorbents, selectivity for specific compounds, durability, and regenerability of the adsorbents. Compared to other decontamination techniques, adsorption has been found to be superior due to its low cost, wide range of applications, simplicity of design, easy operation, insensitivity to toxic pollutants, low harmful secondary products, and easy regeneration of the adsorbents [26].

The removal of contaminants through adsorption is based on the ability of a porous adsorbent to selectively adsorb compounds. This means that substances containing suitable size and shape can easily have access to the pores of the solid sorbents and, therefore, can be eliminated through adsorption. The physical forces that control the adsorption process include van der Waals forces, hydrogen bonds, polarity, dipole-dipole, and π - π interaction [26]. Factors that influence the adsorption efficiency include adsorbate-adsorbent interaction, adsorbent surface area, adsorbent to adsorbate ratio, adsorbent particle size, temperature, pH, and contact time. A variety of porous adsorbents such as activated carbons, zeolites, waste materials (like fly ash), mesoporous materials, metal complexes and MOFs have been studied for adsorptive removal of hazardous substances. For efficient adsorptive removal, porosity, pore geometry, and specific adsorption sites are required. Furthermore, active species such as different functional groups (acidic or basic), metal ions,

and metal oxides are typically incorporated into the framework of the porous adsorbents to enable them selectively to adsorb harmful components through common interactions like acid-base, complexation, electrostatic interaction, and hydrogen bonding [26].

There are several popular modification techniques, including post-synthetic modification, functionalization, ion exchange, impregnation, and loading of porous adsorbents, which have been extensively investigated to improve the adsorption efficiency. Adsorption provides an attractive alternative, especially if the adsorbent has low cost and does not require additional pre-treatment before its application. The efficiency of adsorption can be described by adsorption equilibrium isotherms as well as kinetic models.

2.3.1 Adsorption Isotherm

Adsorption is a type of separation process that occurs at the interface between two phases, and it is governed by equilibrium principles. In order to understand the interaction between the adsorbed molecules and the adsorbent surface, scientists use adsorption isotherms to analyze the process. These isotherms show the relationship between the amount of material adsorbed and the concentration of the adsorbate in the equilibrium state, per unit mass of adsorbent. In adsorption experiments, the mass balance is defined as below when a particular mass of adsorbent reaches equilibrium by a specific volume of solution at a specific concentration of a pollutant.

$$q_e = \frac{C_0 - C_e}{m} V$$

where q_e (mg/g) is the equilibrium adsorption capacity, C_0 (mg L⁻¹) and C_e (mg L⁻¹) are the initial and equilibrium concentration of adsorbate ion, V (L) is the total volume of the solution and m (g) is the adsorbent weight.

The adsorption isotherms provide valuable information about the adsorbent capacity, which is an important factor in determining the efficiency of the adsorption process. By studying

the equilibrium data, scientists can determine the adsorption isotherms and the constant values associated with them. These constant values are related to the surface properties and affinity of the adsorbents, and they help to predict the extent of adsorption in various applications. It is important to understand the relationship between equilibrium data and theoretical or practical equations to be able to interpret and predict the extent of adsorption in specific applications. This understanding helps scientists to optimize the adsorption process and improve its efficiency. Among the various types of adsorption isotherms used for the adsorption process, Langmuir and Freundlich models are the most commonly used because of their simplicity and their ability to describe experimental results over a wide range of concentrations. These models provide valuable insights into the adsorption process and help scientists to optimize the process for maximum efficiency. However, it is important to note that there are other adsorption isotherms that can also be used depending on the specific properties of the adsorbent and the adsorbate [23].

2.3.1.1 Langmuir Isotherm

For the adsorption on a homogeneous surface, the Langmuir isotherm is frequently used. This model assumes that the adsorbent's structure is homogeneous and that the energies of the adsorption sites are equal. On the surface of the adsorbent, adsorbed molecules are considered to create a monolayer as part of the adsorption process. Three key assumptions are considered in the Langmuir adsorption equation. At first, all adsorption sites have a same amount of adsorption energy. Second, adsorption takes place at specific locations without any interaction between the molecules being adsorbed. Third, a maximum monolayer is where the highest adsorption is obtained. This model is described by the following equation:

$$q_e = \frac{q_m K_L C_e}{1 + K_L C_e}$$

where q_m is the saturated/maximum adsorbed capacity (mg g^{-1}) and K_L is the Langmuir constant that directly relates to the energy adsorption (L mg^{-1}) and C_e is the equilibrium concentration (mgL^{-1}). Plotting $1/C_e$ vs $1/q_e$ can be used to depict the Langmuir model constants [15].

2.3.1.2 Freundlich Isotherm

Langmuir's model assumes that adsorption energy is the same for all adsorption sites, but real surfaces are heterogeneous, and thus adsorption energy may differ. Therefore, Freundlich adsorption models are introduced to account for heterogeneity.

$$q_e = K_F C_e^{1/n}$$

where C_e is the equilibrium concentration in solution, K_F is the equilibrium constant indicative of sorption strength and n is the degree of non-linearity. A linear form of the above equation can be obtained by taking logarithms and rearranging the relationship:

$$\ln q_e = \ln K_F + \left(\frac{1}{n}\right) \ln C_e$$

where K_F ($\text{mg}^{1-1/n} \text{L}^{1/n} \text{g}^{-1}$) and n are the Freundlich adsorption isotherm constants. K_F and $1/n$ values can be calculated from the intercept and slope of the linear plot of $\log C_e$ versus $\log q_e$. In the adsorption process, Freundlich constants can be used to define favorable adsorption. n is an indication of deviation from linearity of the adsorption and can be applied to determine different kinds of adsorption. When n is less than unity, the adsorption is a chemical process; when n is greater than unity, it demonstrates a favorable adsorption and a physical process. An adsorption that is linear occurs when n equals unity [18].

2.3.1.3 Temkin Isotherm

In the Temkin isotherm, the heat of adsorption decreases linearly rather than logarithmically, while ignoring extremely low and very high concentrations. In addition, it

assumes a uniform distribution of bounding energy up to a certain maximum. This can be expressed by Eq.

$$q_e = B \ln A + B \ln C_e$$

Where q_e is the amount of adsorbate adsorbed at equilibrium (mg g^{-1}); C_e is the concentration of adsorbate in solution at equilibrium (mg L^{-1}). B is a constant related to the heat of adsorption and it is defined by the expression $B = RT/b$, where b is the Temkin constant (J mol^{-1}), T is the absolute temperature (K), R is the gas constant ($8.314 \text{ J mol}^{-1} \text{ K}^{-1}$), and A is the Temkin isotherm constant (L g^{-1}). From the plot of q_e vs. $\ln C_e$, B and A can be calculated from the slopes (B) and intercepts ($B \ln A$), respectively [23].

2.3.2 Adsorption kinetics and mechanisms

Adsorption is a complex process that involves the accumulation of particles or molecules on a solid surface. To gain a deeper understanding of this process, kinetic studies are often conducted to determine the rate of adsorption and to identify the underlying mechanisms involved. The kinetics of adsorption are typically modeled using mathematical equations that can help predict the behavior of the system under different conditions. The rate of adsorption is influenced by various factors, including the concentration of the adsorbate, the surface area of the adsorbent, and the temperature of the system. Understanding the kinetics of adsorption is crucial in determining the feasibility of using a particular adsorbent in practical applications, such as water treatment, air purification, and wastewater management.

The adsorption mechanism can be broken down into three stages: film diffusion, pore diffusion, and adhesion of solute molecules to the adsorbent surface. In the film diffusion stage, the adsorbate molecules move through the films surrounding the surface of the adsorbent particle. During the pore diffusion stage, the molecules penetrate the pores of the

adsorbent to reach the adsorption site. Finally, during the adhesion stage, the adsorbate molecule attaches itself to the surface of the adsorbent. The extent to which each of these stages occurs depends on various factors, such as the size and shape of the adsorbate molecule, the pore size and distribution of the adsorbent, and the chemical nature of the adsorbate-adsorbent interaction.

Various mechanisms are involved in adsorption, including electrostatic interactions, hydrogen bonding, π - π interactions, ion exchange and hydrophobic interactions. The simultaneous occurrence of multiple interactions is also possible. Electrostatic interactions is the most common pathway of adsorptive removal of contaminants from water. Surface charges on adsorbents are created when they encounter polar environments like water. pH in water can affect the surface charge of adsorbents. An additional adsorption mechanism is hydrogen bonding, which occurs during the adsorption of pollutants, particularly organic compounds. The uptake of As(V) was attributed to ion-exchange and H-bond interaction[26].

2.3.2.1 Pseudo-first order model

Lagergren's kinetics equation, also known as the pseudo-first order equation, is a widely used model for studying the kinetics of an adsorption system. This equation describes the rate of adsorbate uptake over time, which is directly proportional to the difference between the equilibrium concentration and the concentration at any given time, as well as the amount of solute uptake during that time period:

$$\frac{dq_t}{dt} = K_1(q_e - q_t)$$

It is important to note that at the beginning of the adsorption process, the concentration of the solute is zero, i.e., $q_t=0$ at $t=0$. By integrating the above equation, we can derive the following relationship:

$$\log(q_e - q_t) = \log q_e - \frac{K_1 t}{2.303}$$

Here, q_t (in units of mg g^{-1}) represents the amount of adsorbed molecules per unit mass of adsorbent at time t , which is the contact time (in minutes). k_1 is the pseudo-first order rate constant (in units of min^{-1}) and can be calculated by plotting $\log(q_e - q_t)$ versus t .

This equation is widely used for studying the kinetics of adsorption because it provides a simple way to determine the rate constant and to predict the amount of adsorbate uptake over time. Additionally, it assumes that the rate of adsorption is proportional to the number of unoccupied sites on the adsorbent surface, which is often a reasonable approximation for many adsorption systems. It is important to note, however, that this model may not be appropriate for all adsorption systems, particularly those that exhibit complex kinetics or interactions between the adsorbate and adsorbent. In such cases, alternative models may be needed to accurately describe the adsorption process [23].

2.3.2.2 Pseudo-second order model

The relationship for the pseudo-second order model is expressed as follows:

$$\frac{dq_t}{dt} = K_2(q_e - q_t)^2$$

where k_2 represents the rate constant of the pseudo-second order model (in units of $\text{g mg}^{-1} \text{min}^{-1}$). This model assumes that the rate of adsorption is proportional to the square of the difference between the equilibrium concentration and the concentration at any given time.

By integrating the above equation and rearranging it into a linear form, we get the following relationship:

$$\frac{t}{q_t} = \frac{1}{k_2 q_e^2} + \frac{t}{q_t}$$

Here, t is the contact time (in minutes), and q_t represents the amount of adsorbed molecules per unit mass of adsorbent at time t (in units of mg g^{-1}). The values of k_2 and q_e can be determined by plotting t/q_t against t .

The pseudo-second order model is a useful tool for studying the adsorption kinetics of many systems, as it considers the influence of both surface coverage and diffusion processes. It is

particularly useful for systems in which the adsorbate concentration is high, as it provides a more accurate representation of the kinetics than the pseudo-first order model [18].

2.3.2.3 Intra-particle diffusion model

Weber and Morris developed the intra-particle diffusion model to explain adsorption mechanisms in terms of diffusion. Adsorption can be controlled by mass transfer rate in the liquid phase or mass transfer inside the particles. The intra-particle diffusion resistance effect on adsorption can be expressed by the following formula:

$$q_t = C + K_D t^{0.5}$$

Here, kD is the intra-particle diffusion rate constant (in units of $\text{mg g}^{-1} \text{min}^{-0.5}$), and C represents the thickness of the boundary layer. The intra-particle diffusion rate constant can be determined from the slope of the linear plot of q_t versus $t^{0.5}$. If diffusion is controlled by intra-particle diffusion, the plot is linear and passes through the origin. A larger intercept value represents a greater boundary layer effect.

The adsorption process involves several stages that can be identified through the plot of adsorbate uptake against time. Typically, these plots show three stages, each with its own unique characteristics. The first stage is the initial portion of the curve where the uptake rate is high and it is due to external mass transfer. Here, the adsorbate molecules have to pass through a solute film before being adsorbed onto the surface of the adsorbent particle. This results in resistance to the mass transfer process. The second stage is the intermediate linear portion of the curve which is attributed to the intra-particle diffusion process. This stage occurs when the external mass transfer resistance is overcome and the adsorbate molecules start to penetrate into the interior of the adsorbent particles. The third stage is the plateau region where the uptake rate becomes almost constant. This is because the intra-particle diffusion process starts to slow down due to a small driving force caused by a low adsorbate concentration difference between the solution medium and within the pores [73].

2.3.2.4 Elovich

It is a widely used model to describe the adsorption kinetics of gases, liquids or solids onto solid surfaces. The model is named after the Soviet chemist Yakov Elovich, who proposed it in 1962. The Elovich model assumes that the rate of adsorption decreases as the surface becomes increasingly covered with adsorbate, which is a common feature of most adsorption systems. Mathematically, the model is expressed as a pseudo-first-order equation that takes into account both surface coverage and activation energy:

$$q_t = \frac{1}{\beta} \ln(\alpha\beta) + \frac{1}{\beta} \ln(t)$$

where q is the amount of adsorbate adsorbed at time t , β is the initial adsorption rate, and α is a constant related to the activation energy of the process.

The Elovich model has been successfully applied to a variety of adsorption processes, including the adsorption of dyes, heavy metals, and organic compounds onto different types of adsorbents. It provides a useful tool for analyzing adsorption kinetics and designing adsorption processes [38].

2.3.3 Adsorption parameters

The ability of various adsorbents to adsorb substances is influenced by several factors, which can be attributed to the characteristics of the adsorbent itself, such as surface area, pore structure, and functional groups, as well as the properties of the substance being adsorbed, including molecular size, functional groups, polarity, and aqueous solubility. Additionally, it should be acknowledged that the conditions of the adsorption process, such as solution pH, temperature, and ionic strength, can also impact the interactions between the adsorbent and adsorbates.

2.3.3.1 Point of zero charge

The point of zero charge (pzc) is a crucial parameter that helps to describe the electrokinetic properties of a surface. It represents the pH value at which the surface has a neutral charge. This parameter is particularly useful for systems where the potential determining ions are H^+ and OH^- . It is worth noting that the presence of functional groups such as OH^- can influence the adsorption of cationic or anionic dyes at different pH values. At pH levels above the pzc, the surface charge becomes negative due to the presence of OH^- functional groups. Consequently, cationic complex adsorption is favored. Conversely, at pH levels below the pzc, the surface charge becomes positive, and anionic complex adsorption is preferred. Therefore, understanding the pzc is essential for explaining the adsorption mechanism of different adsorbates at the solid-water interface.

Moreover, zeta measurements are critical for comprehending the adsorption mechanism of both organic and inorganic molecules at the solid/solution interface. These measurements also play a significant role in determining the stability of colloids. Overall, the pzc and zeta measurements provide valuable insights into the surface chemistry of different adsorbents and are important tools for designing and optimizing adsorption processes [28].

2.3.3.2 Solution pH

The pH level of a solution is a crucial factor that has an impact on the adsorption performance. Alterations in the pH conditions of a solution can cause changes in the chemical characteristics of the adsorbent surface, as well as the forms of the adsorbate molecules. The interaction of acidic or basic species with the surface groups of the adsorbent can modify its surface chemistry, leading to changes in its adsorption capacity. It's important to note that the behavior of the surface functional groups of the adsorbent, as well as their interactions with water molecules, depend on the pH level of the adsorption environment. These interactions may result in the transformation of active sites. When the pH of a solution

increases, the number of negatively charged sites increases, which can decrease the adsorption of negatively charged molecules due to electrostatic repulsion.

The alteration of pH levels can affect the surface ionic charge of both adsorbate molecules and adsorbent materials, which in turn affects the zeta potential and electrostatic interactions during the adsorption process. Additionally, pH conditions can impact the solubility and dissociation of adsorbate and adsorbent in the solution. The pH level of the solution also influences the surface charge of the adsorbent and the ionization of the adsorbate molecules [28].

2.3.3.3 Solution temperature

The temperature of a solution plays a crucial role in the process of adsorption due to its impact on the adsorption of water and the hydration degree of molecules. Increasing the temperature leads to an increase in the adsorption capacity, which can be attributed to the stronger bonds between adsorbate molecules and the adsorbent surface at higher temperatures. Furthermore, an increase in temperature results in a reduction in the viscosity of the solution, leading to an increase in the diffusion rate of the adsorbate molecules in both the external boundary layer and the internal pores of the adsorbents. Additionally, the equilibrium capacity of adsorbents for specific adsorbates changes with changes in temperature. The impact of temperature on adsorption processes is often expressed through the following relationships:

$$\Delta G^{\circ} = \Delta H^{\circ} - \Delta S^{\circ} T$$

$$\Delta G^{\circ} = -RT \ln K_C$$

The van't Hoff equation can be derived by combining the above relationships:

$$\ln K_C = \Delta S^{\circ} R - \Delta H^{\circ} RT$$

Here, K_C is the equilibrium constant, defined as the ratio of the metal equilibrium concentration on the adsorbent to the metal equilibrium concentration in solution. R is the

ideal gas constant ($8.314 \text{ J mol}^{-1}\text{K}^{-1}$), and T is the adsorption temperature in Kelvin. By plotting $\ln K_c$ against $1/T$, a linear line can be drawn, and the values of $\Delta H^\circ (\text{kJ mol}^{-1})$ and $\Delta S^\circ (\text{J mol}^{-1}\text{K}^{-1})$ can be calculated from the slope and intercept of the van't Hoff plot [42].

2.3.3.4 Adsorbent properties

To effectively remove compounds from solvents, adsorbent materials must possess a high internal volume accessible to the target compounds. The adsorption process is highly influenced by the surface area, pore size distribution, and nature of the pores in the adsorbent material. Additionally, mechanical properties such as strength and resistance to destruction are crucial for an adsorbent's efficacy. The chemical properties of the adsorbent, including ionization degree, functional group types, and variations when in contact with a solution, also play a key role in determining the adsorption capacity. Chemical interactions resulting from active functional groups on the adsorbent surface can have effects different from physical adsorption and are less reversible [24].

Various adsorbent materials, such as activated carbon, clay minerals, zeolites, metal oxides, agricultural wastes, biomass, and polymeric materials, have been used for water treatment, particularly for removing heavy and toxic metal ions. Pore size and distribution, surface area, surface chemistry, and mineral content are the main parameters influencing the adsorption process. The pore size distribution must be suitable to provide adsorption sites and channels for transporting adsorbates. Access to micropores depends on the size of the adsorbate molecules, with smaller molecules accessing micropores, natural organic compounds accessing mesopores, and bacteria accessing macropores.

Various modification methods, including acidic and base treatment, impregnation, microwave treatment, ozone treatment, and plasma treatment, have been used to increase the adsorption capacity of activated carbon for various pollutants. Activated carbon has functional groups or atoms bonded to its structure, such as carboxyl, carbonyl, phenols,

lactones, and quinones, which are responsible for adsorption of contaminants. These functional groups can be obtained or modified using activation processes, precursors, thermal treatment, and post-chemical treatments. Porous materials have unique properties that make them suitable for adsorption applications, and an understanding of their structures and properties is essential for designing and selecting appropriate adsorbents for specific applications, such as water treatment.

2.3.4 Porous material adsorbents

Porous materials are of great interest from both scientific and technological perspectives due to their ability to interact with atoms, ions, and molecules at the surface and within the bulk of the material. As a result, they have found widespread applications in ion exchange, adsorption, and catalysis, particularly for environmental purposes. The pores of solids are classified based on their sizes, with micropores referring to pore sizes below 2 nm, mesopores between 2 nm and 50 nm, and macropores above 50 nm. The effectiveness of porous materials in specific applications is determined by the distribution of pore sizes, as well as the shapes and volumes of the void spaces within the porous structure. In addition to pore size, the atoms within the solids are crucial to their applications. For instance, hydrophobic molecular sieves, such as pure silica, can adsorb organic compounds from water, while hydrophilic molecular sieves containing aluminosilicate can adsorb water from organic solvents. Activated carbons' surface chemistry and chemical characteristics are determined by heteroatoms, or atoms other than carbon. Oxygen, in particular, is a significant heteroatom that exists in the form of carboxylic acid groups, phenolic, hydroxyl groups, and quinone carbonyl groups. The formation of carboxylic acid and phenolic hydroxyl groups explains the acidic nature of activated carbons. The presence of π -electrons on the condensed polyaromatic sheets is associated with the basic characteristics of activated carbons. The elimination of oxygen from the surface of activated carbon by heat

treatment in an inert atmosphere results in the formation of these electron-rich Lewis base sites, which attract and localize π -electrons of condensed polyaromatic sheets. The elimination of oxygen-containing functional groups from the surface of activated carbon makes the surface more basic and less polar. This is highly favorable for the adsorption of organic pollutants from aqueous solutions. Heat treatment in an inert environment can also remove oxygen-containing functionalities from activated carbon surfaces and create highly reactive sites. Water molecules can adsorb on oxygen-containing functional groups via hydrogen bonding, and additional water molecules can cluster at these sites. The water clusters can prevent pollutant access to hydrophobic areas on activated carbon, decrease the interaction energy between contaminants and the surface of the adsorbent, and block the contaminant molecules from accessing the micropores, as studies have shown [7].

2.4. Arsenic

Arsenic is a rare crystal element comprising about 0.00005% of the earth's crust and the average concentration of arsenic in igneous and sediment rocks is 2 mg kg⁻¹. The concentration of arsenic in unpolluted fresh waters typically ranges from 1–10 mg L⁻¹, rising to 100–5000 mg L⁻¹ in areas of sulfide mineralization and mining [27]. There is a massive epidemic of arsenic poisoning spread by groundwater contamination in South and South East Asia. Approximately 60 million people drink groundwater contaminated with arsenic above 10 ppb [28]. As(V) and As(III) are the two main forms of arsenic found in natural water [29]. Arsenic might be co-precipitated with iron hydroxides and sulfides in sedimentary rocks. Iron deposits, sedimentary iron ores and manganese nodules were rich in arsenic. Arsenic naturally occurs in over 200 different mineral forms, of which approximately 60% are arsenates, 20% sulfides and sulfosalts and the remaining 20% includes arsenides, arsenites, oxides, silicates and elemental arsenic (As). Various forms of inorganic and organic arsenic species (arsenicals) are found in food, water, and other environmental media. In terms of toxicity, arsenic's chemical forms and oxidation states matter more [30]. In

comparison to As(V), As(III) is more toxic and more difficult to remove from water due to its weaker affinity to the surface of adsorbents. As a result, many adsorbents have little capacity to remove As(III). A redox condition, pH level and the presence of complex ions in water influence As(III) and As(V) removal capacities. Consequently, pre-treatment processes such as oxidizing As(III) to As(V) and adjusting pH levels are often necessary for effective removal of arsenic. However, these pre-treatment processes are expensive and time-consuming, and may result in secondary contamination [27][31]. The level of toxicology is also affected by physical state, particle size and state of a gas, solution, or powder, rate of absorption and elimination of the toxic compound, nature of any chemicals in the toxic compound, as well as the pre-existing state of the individual. There are several health effects associated with chronic exposure to inorganic arsenic, including effects on the gastrointestinal tract, respiratory tract, skin, liver, cardiovascular system, hematopoietic system, nervous system, etc. [27]. The speciation of arsenic is sensitive to both the redox state and pH of the chemical environment. The most stable redox states are -3 (arsine gas, AsH_3), -1 (alkyl arsenic), 0 (zero-valent, elemental arsenic), $+3$ (the arsenites) and $+5$ (the arsenates), and these latter two states dominate aqueous arsenic solutions [32]. Figure 2-1 shows schematic specification of arsenic in oxidation states. As(V) appears in a negative ionic form (H_2AsO_3^-) under most pH values, whereas As(III) exists in a nonionic form (H_3AsO_4) [28].

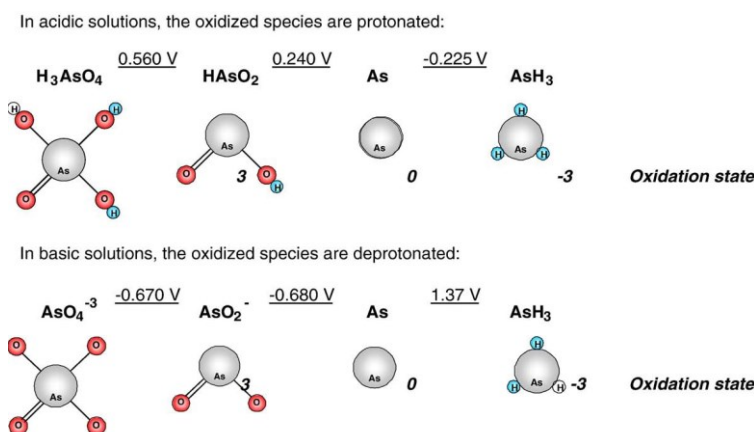


Figure 2-1: Schematic speciation of arsenic in oxidation states 5, 3, 0 and -3 in acidic and basic solutions [32].

2.4.1 Arsenic Removal Methods

Detecting and removing toxic substances from contaminated water is one of the objectives of decontamination, since widely distributed substances, such as arsenic, are known to cause harm to humans and the environment. So, it remains a challenging problem to effectively eliminate arsenic from water systems [33]. In the majority of reported cases, As is found as As(III). Oxidation of As(III) to As(V) is considered necessary to obtain satisfactory As removals [29]. A number of conventional methods exist for removing arsenic. Coagulation, flocculation [34], precipitation [35], adsorption and ion exchange are among the methods used for this purpose. The removal of arsenic is also accomplished through alternative methods like ozone oxidation, solar oxidation techniques [36] bioremediation, and electrochemical treatment [7][37]. Filtration and coagulation are the most common methods. Although ion exchange resins are effective in removing arsenate. Hence, resin may not be an appropriate method for removing arsenic from raw water sources that are high in As(III). to other methods, membranes [7] are expensive to use for arsenic removal. In the emerging field of arsenic removal, iron oxide-coated sand and other iron oxide-coated or loaded materials are effective at removing arsenic from water [38]. Figure 2-2 shows classification of different nano materials for water treatment.

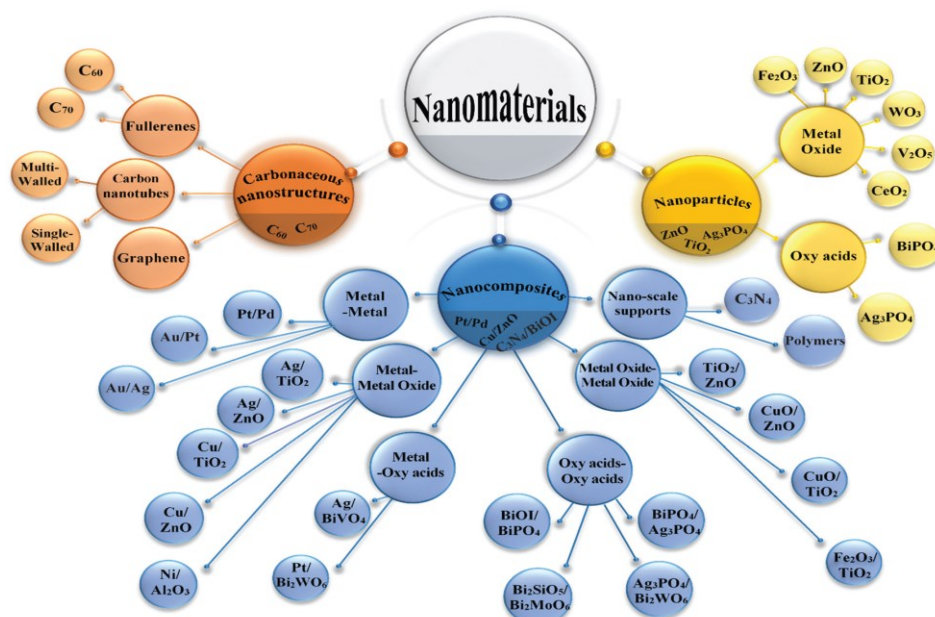


Figure 2-2: Classification of different NMs used for water and wastewater treatment [39].

2.4.1.1 Adsorption and ion exchangers

The adsorption process is prevalent in most natural physical, biological, and chemical systems. Industrial applications use adsorption operations, such as utilizing solids such as activated carbon, metal hydrides and synthetic resins, for purification of water and wastewater. Adsorption occurs mainly due to van der Waals forces and electrostatic forces between molecules adsorbate and atoms composing the adsorbent surface. Hence, the first property of an adsorbent is its surface area and polarity. In order to remove arsenic, an ion exchange resin that is usually loaded with chloride ions is placed in vessels. When the contaminated water passes through the vessels, the arsenic "exchanges" with the chloride ions. Arsenic levels are lower when the water exits the vessel, but chloride levels are higher. When the resin has reached exhaustion, all or most of the "exchange sites" that were previously occupied by chloride ions become occupied by arsenic or other anions. On the resin, the chloride ions were exchanged for anions that were present in the water being treated, including arsenic [30]. For red mud adsorbent showed exothermic adsorption of

As(III), whereas As(V) adsorption was endothermic [40]. In arsenic treatment process generally use activated carbon as a material to increase arsenic adsorption and researchers treated carbon with various metal ions such as iron oxide. Higher As(III) and As(IV) concentrations were found in activated carbon impregnated with iron oxide (V). Because of its financial mater, commercial activated carbon is not appropriate for developing nations so preparation of low-cost adsorbent for water purification and wastewater treatment has been reviewed by Pollard et al. [41] agricultural wastes like rice husk [42], coconut husk [43], amine modified coconut coir [44], orange juice residues [45], iron oxide-coated biomass [38] and waste tea fungal biomass [46] and Cellulose Loaded with iron oxyhydroxide [47]. In comparison to activated carbon, iron oxides have been widely used as sorbents to remove pollutants from wastewater. Hydrated amorphous like aluminum hydroxides, iron(III), and manganese oxyhydroxides are more effective at adsorbing arsenates than more crystalline materials, however the low pH values are desire for adsorption [48]. More than 90% of the adsorption took place within the first 10 min with a kinetic rate constant of 3.5 mg min^{-1} [7].

2.4.2 Adsorbents

Metal oxide base adsorbents like activated alumina, iron oxides, zirconium oxides, titanium oxides, cerium oxide and binary metal oxides is use to remove arsenic from wastewater [33].

2.4.2.1 Activated Alumina

There are a number of adsorbents based on aluminium, including activated alumina, gibbsite (a mineral $\text{Al}(\text{OH})_3$), aluminium hydroxide precipitated from aluminium salts, and layered double hydroxides. While arsenic(V) is well known to be strongly adsorbed by aluminum hydroxides, arsenic(III) is considerably less readily adsorbed [49]. When the pH of wastewater was slightly acidic and competing, activated alumina successfully removed arsenic [50]. An advantage of activated alumina is its simple and long-term operation, even for up to 3 months before it needs to be regenerated. Regenerating via a combination of

NaOH and H₂SO₄ is also disadvantageous. For an activated alumina adsorbent, its pores should be accessible and interconnected, and its surface area should be high, along with its chemical or physical stability. According to the Langmuir isotherm, the maximum adsorption capacity of arsenic (As(V)) at neutral pH is 36.6 mg g⁻¹ [51].

2.4.2.2 Titanium Oxides

Compared to fumed TiO₂ (Degussa P25) and granular ferric oxide, nanocrystalline TiO₂ had a higher adsorption capacity for As(V) and As(III) [33]. Experimental results revealed that more than 98% of the As(V) was removed by TiO₂ in the pH range of 4 to 9.5. As the pH increased to 11.8 the As(V) adsorption decreased significantly. Compared with As(V), As(III) removal increased from 72 to 95% after increasing the pH from 4.5 to 9.5. At approximately pH 9.5, As(III) uptake is greatest [52]. Since TiO₂ has a high surface area to volume ratio, corrosion resistant, non-toxic and stable, these nanomaterials and nanocomposites are proven to be more suitable for both forms of arsenic [53].

2.4.2.3 Magnesium Oxides

To remove toxic ions and organic pollutants from water, magnesium oxide was used as a sorbent. An adsorption capacity of 506.6 mg g⁻¹ was observed for the MgO adsorbents in aqueous solutions for the removal of As(III). By interacting with water, MgO nanoflakes produced Mg(OH)₂ in situ, resulting in high As(III) adsorption capacity. Upon formation of Mg(OH)₂, magnesium-arsenite compounds can be formed, which contributes to the high affinity of As(III) in aqueous [33]. mesoporous MgO hollow spheres (MgO-HS) with high specific surface area (175 m² g⁻¹ is prepared by using mesoporous hollow carbon spheres as templates and ultra-high maximum As(III) adsorption capacity of 892 mg g⁻¹ was achieved in batch As(III) removal study with Adsorption kinetic 6 times faster commercial MgO adsorbent [54]. The phase transformation of dense Mg(OH)₂ nanoflakes into porous ones was achieved by converting dense MgO nanoflakes by using a hydrothermal process and a

calcination step. The sorption capacity of these MgO nanoflakes is 506.6 mg g⁻¹ [55]. MgO adsorbs large amounts of arsenic at pH ranges 10-12 under batch conditions [56]. Figure 0-3 shows annealing temperature and sorption capacity MgO.

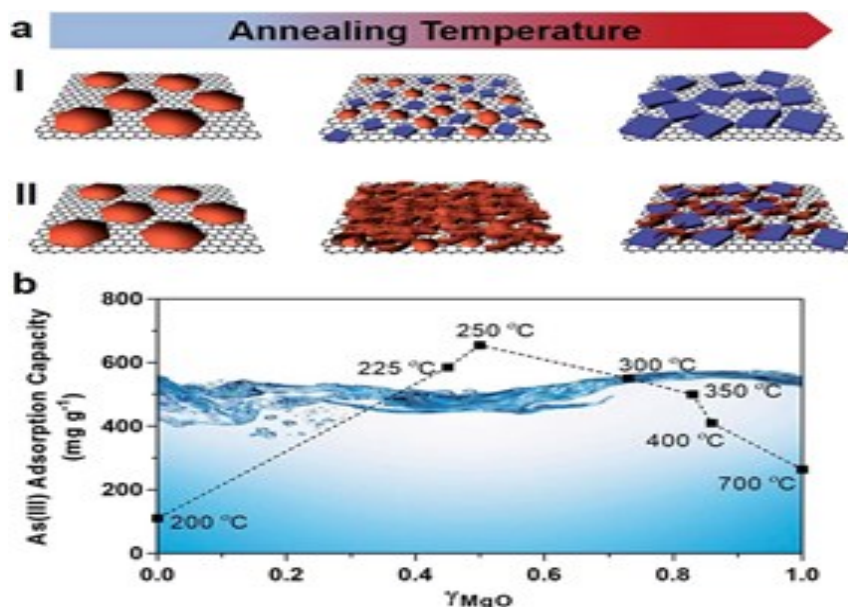


Figure 0-3: (a) Schematic illustration of the influence of annealing temperature on the structures of Mg(OH)₂-MgO@rGO nanocomposites (I) before and (II) after hydration. (b) As(III) sorption capacity of Mg(OH)₂-MgO@rGO nanocomposites as a function of the content of MgO (γ_{MgO}) and the annealing temperature (200–700 C) [57].

The characteristics of the reaction product of MgO are affected by the initial concentration of aqueous As. aqueous As removal and MgO-reaction products that contain As are affected by seawater. MgO reacted more strongly with arsenic as the salinity of seawater increased [58]. Using an economical precipitation-calcination method, the carbon supported MgO particles were prepared with a porous structure that allowed better adsorption than regular MgO particles. An analysis of the microstructure of the particles indicates they have a rod-like shape and are coated in carbon [59]. Figure 2-4 shows the procedure of synthesis C-MgO micro rods.

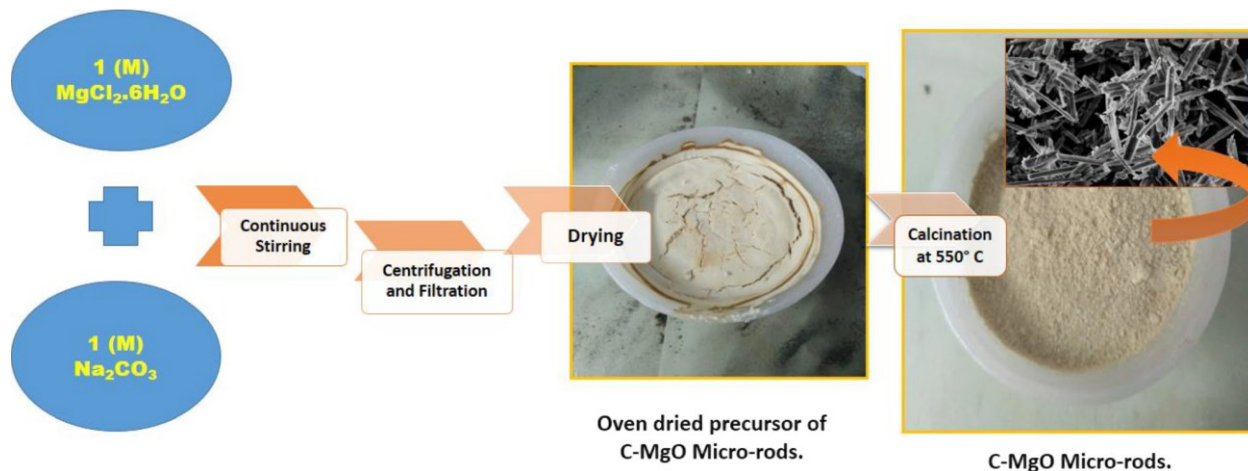


Figure 2-4: The schematic diagram for the synthesis of C-MgO micro-rods [59].

2.4.2.4 Iron Oxide Nanostructures

Iron is one of the most common elements on the planet [33]. For removal arsenic from water, iron oxide-coated sand adsorbent was investigated through a simple synthesis procedure [60]. Also, for both laboratory scale and natural waters, The ultrafine $\alpha\text{-Fe}_2\text{O}_3$ nanoparticles were synthesized to eliminate arsenic ions from water. In this highly porous structure with surface area about $162 \text{ m}^2\text{g}^{-1}$, these $\alpha\text{-Fe}_2\text{O}_3$ nanoparticles were clumped together and, on the surface, high-affinity hydroxyl groups were coated. The adsorption capacities of $\alpha\text{-Fe}_2\text{O}_3$ nanoparticle adsorbent for As(III) and As(V) wastewater sample were 95 mg g^{-1} and 47 mg g^{-1} , respectively, at pH of 7. This adsorption capacity occurs even in very high competing anion concentrations. Furthermore, these $\alpha\text{-Fe}_2\text{O}_3$ nanoparticles could successfully remove both As(III) and As(V) from a polluted natural lake water sample without peroxidation and/or pH modification [61]. In other research, to remove As(V) ions, flower-like hierarchical iron oxides adsorbent were employed. Many factors can impact self-assembly of adsorbent, including crystal-face attraction, electrostatic and dipolar fields associated with the aggregate, van der Waals forces, hydrophobic interactions, and hydrogen bonds. [62]. With all three types of iron oxides ($\alpha\text{-Fe}_2\text{O}_3$, $\gamma\text{-Fe}_2\text{O}_3$, and Fe_3O_4), an As(V) adsorption

capacity of 5.3 mg g^{-1} was reported, which was approximately ten times greater than that of a commercial iron oxide sample (0.46 mg g^{-1}) [33].

The pH value affects arsenate adsorption on iron oxy-hydroxides. Hematite and goethite may adsorb more than 80% of arsenic at pH levels corresponding to natural pH water, regardless of the initial concentration. However, depending on the contamination rate, goethite for high contamination levels and hematite for low contamination levels should be considered [63]. Because of their magnetic characteristics, $\gamma\text{-Fe}_2\text{O}_3$ and Fe_3O_4 might be recovered efficiently using a simple magnetic separation process. Surface complexation and ion exchange between the iron oxide surface and the hazardous ions in the aqueous solution were proposed as mechanisms for eliminating the metal and anionic pollutant. The rate of arsenate adsorption is affected by pH and initial arsenic concentrations. Adsorption of arsenate is enhanced at acidic pH values and reduces fast in a basic media. At $500 \text{ }\mu\text{g L}^{-1}$ As(V), adsorption reactions are effective over a more limited pH range. The rate of arsenate adsorption is proportional to the iron content of the adsorbents, and it rises in the following order: goethite < hematite < magnetite < ZVI. The Langmuir model is appropriate for most all adsorbents (hematite, goethite, ZVI), confirming monolayer adsorption, according to empirical modelling of adsorption isotherms. At high arsenic concentrations, hematite is the best adsorbent over natural pH (pH 6–9). Arsenic was shown to be more strongly bound to hematite than other adsorbents (goethite or magnetite) in desorption isotherms [63]. As(V) appears in a negative ionic form (H_2AsO_3^-) under most pH values, whereas As(III) exists in a nonionic form (H_3AsO_4). The point of zero charge (pH_{PZC}) of the adsorbent helps explain the pH value relation of arsenic ions adsorption onto adsorbent. The adsorbent surface is positively charged when the $\text{pH} < \text{pH}_{\text{PZC}}$, and negatively charged when the $\text{pH} > \text{pH}_{\text{PZC}}$ [28]. In the presence of adsorbed ions, the pH_{zpc} of the adsorbent was evaluated by measuring the pH_{iep} of the surface. $\text{pH}_{\text{zpc}} = 6.5\text{--}8.5$ was determined for Fe_3O_4 , $\alpha\text{-FeOOH}$, $\gamma\text{-Fe}_2\text{O}_3$, and amorphous $\text{Fe}(\text{OH})_3$ [64]. Due to the highly greater specific surface area, pore volume, and

pore diameters of the mesoporous γ -Fe₂O₃ structures, their adsorption uptake (73.2 mg g⁻¹) is at least double what as that of the aggregated γ -Fe₂O₃ nanoparticles (32.3 mg g⁻¹). As a consequence, the as-prepared mesoporous γ -Fe₂O₃ structures have a high capability for removing arsenic ions when compared to aggregated γ -Fe₂O₃ nanoparticles [65]. According to Babu et al., the adsorbed arsenic on magnetic Fe₃O₄ core-shell nanorods was completely removed by magnetic separation and recovered by acid treatment, resulting in a 99% arsenic removal rate [66]. an environmentally safe hydrothermal method is used to produce superparamagnetic acid-coated Fe₃O₄ nanoparticles with a high specific surface area, which had a maximum adsorption capacity of 16.56 mg g⁻¹ for arsenic(V) and 46.06 mg g⁻¹ for arsenic (III). The diameter of the ascorbic acid-coated Fe₃O₄ nanoparticles as generated is less than 10 nm, resulting in a high specific surface area of roughly 179 m² g⁻¹, which is even more than that of well-defined mesoporous structures [67]. iron-oxide coated natural rock (IONR) adsorbent remove 98.5% As(III) within 6 h of contact time and at a dose of 13 g L⁻¹ from wastewater at room temperature, when the initial concentration was 0.6 mg L⁻¹ [68].

2.4.2.5 Binary Metal Oxides

Binary oxides on the basis of two or more metals (or elements) may be a more effective way to remove arsenic from contaminated water than single metal oxides [33]. The ultrafine Fe-Mg nano crystals were synthesized using a solvent thermal process. Both laboratory and natural water samples showed highly enhanced adsorption of arsenic as a result of magnesium doping of the nano crystallites. This is due mainly to an enhanced surface area, extensive dispersion, and contact with arsenic species in water. The development of a simple, efficient, and one-step treatment method for arsenic-contaminated water could reduce the demand for pre- and post-treatments necessary for most industrial processes [69]. Based on the Mn/Fe ratio of the binary oxide, As(V) retention, As(III) oxidation, and sorption were different. By increasing Mn/Fe, more As(V) is retained, with the maximum retention occurring at approximately 1:6 Mn/Fe. Likewise, the maximum uptake of As(III) occurred at

a Mn/Fe ratio of 1:3. Furthermore, the Fe – Mn binary oxides could absorb much more As (III) than As (V). As discussed in the sorption study, arsenic may be retained much more readily in sediments and soils where Mn and Fe (hydr)oxides coexist, since As(III) is easier to retain than As(V) [70]. Using impregnation-coprecipitation-calcination, active carbon was modified by MgO-MnO₂. A significant increase in Rhodamine B removal was observed on MgO-MnO₂-AC, and the maximum adsorption amount of RB was found to be 30.30 mg g⁻¹ at 25°C [71]. Figure 2-5 shows the procedure of synthesis MgO-MnO₂-AC.

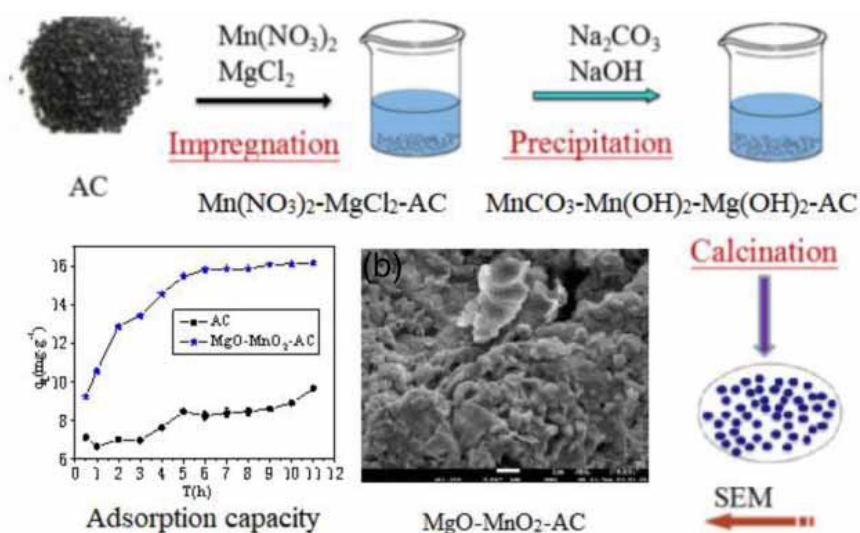


Figure 2-5: MgO-MnO₂ synthesis schematic.

Fe-Zr binary oxide is environmentally friendly and easy to prepare. As(V) and As(III) could be effectively removed by this adsorbent with maximum adsorption capacities of 46.1 and 120.0 mg g⁻¹ at pH 7.0, respectively, with large surfaces and pseudo-second order equations. The Fe-Zr binary oxide adsorbs arsenic in spite of competing anion species. Phosphate was the most dominant anion against which arsenic could bind [72]. With 2.0 M alkali solution, the arsenic sorbed material could be regenerated (80%)[73]. There are significantly higher adsorption capacities of mesoporous Magnesium-Aluminum Oxide for As(V) and As(III) at pH 3 and pH 7, compared to other reported adsorbents. Even in the presence of co-existing anion species, As(V) retained with high selectivity despite its

superior adsorption capacities. By increasing Mg/Al ratio, the hexagonal structures of the mesopores have evolved into wormhole-like structures [31]. another two-metal oxide adsorbent (Fe-Ce system) displayed considerable arsenic adsorption capability by doping cerium ions into the Fe II/III system [74]. Using Fe(Magnetic)-Mn particles (0.1 g/L) with an adsorption capacity of 47.76 mg g⁻¹, As(III) concentrations of 200 mg L⁻¹ at pH 7.0 could be decreased to below 10 mg L⁻¹ in 20 minutes and adsorption and desorption efficiencies maintained above 98% and 87% throughout five consecutive cycles [75]. For manganese oxide-coated-alumina, the maximum As(III) sorption capacity was 42.48 mg g⁻¹, which is much higher than that of activated alumina (20.78 mg g⁻¹) [76].

2.4.2.6 Layer Double Hydroxide Composites

Layered double hydroxides (LDHs) are widely studied for their ability to adsorb various anions. A new method has been presented to synthesize Mg-Fe LDH nanoplates with controlled Mg/Fe molar ratios (3:1, 4:1, 5:1) using a thermal method. The adsorption capacity of these LDHs for arsenate removal from water has been investigated. The results indicate that the Mg/Fe molar ratio has a significant effect on the adsorption of As(V) on the synthesized LDHs. Among the three different Mg/Fe molar ratios, the LDHs with a 4:1 Mg/Fe molar ratio exhibited the highest adsorption capacity and the fastest adsorption rate due to the higher BET surface area and the presence of metastable iron ions in the brucite-like sheets of the LDHs. Furthermore, the synthesized LDHs were calcined at 350°C for 5 hours, and their As(V) adsorption performance was evaluated. The calcined LDHs showed excellent adsorption performance with a high adsorption rate and capacity. The investigation revealed that the Mg/Fe molar ratio played a vital role in the performance of arsenate adsorption on calcined LDHs. The LDHs with a Mg/Fe molar ratio of 4:1 demonstrated outstanding adsorption properties, reaching adsorption equilibrium within 5 minutes and achieving the highest adsorption capacity of 271 mg g⁻¹, which was attributed to the higher BET surface

area and excess adsorption capacity through the formation of FeAsO_4 from metastable iron in the LDH and arsenate in solutions [77].

In another study of development of a new material called Fe/Mn-C layered double hydroxide composite (Fe/Mn-C-LDH) has been undertaken to remove arsenic from aqueous solutions. To test the efficacy of the composite, batch experiments were conducted to investigate its removal performance toward arsenic ions. Results revealed that Fe/Mn-C-LDH exhibited an exceptional adsorption capacity for both As(III) and As(V) at 318 K, with values of 46.47 mg/g and 37.84 mg g⁻¹, respectively. The release of Fe³⁺ and Mn²⁺ in the process of arsenic adsorption was also investigated, revealing that Fe/Mn-C-LDH exhibited better stability compared to Fe/Mn-layer double hydroxide (Fe/Mn-LDH), with fewer Mn²⁺ and Fe³⁺ releasing under the same conditions. Interestingly, the specific surface area of Fe/Mn-C-LDH decreased after adsorption of As (III) and As (V), according to the BET results. These findings demonstrate the potential of Fe/Mn-C-LDH composite as an effective adsorbent for removing arsenic from contaminated water sources [78].

A bead type LDH (BLDH) mixed with starch was manufactured and evaluated as an As stabilizer in soil by comparing its effectiveness with powdered type LDH (PLDH) in various experiments. Soil samples were collected from farmland near a storage facility for mine tailings generated by gold mining activities, with an average As concentration of 112.523 mg/kg exceeding the South Korean countermeasure standards for soil contamination (75 mg/kg of As concentration in 1 area). The As sorption efficiency of PLDH and BLDH was over 99%, and the pH of the solution after the addition of LDH was within the Korean municipal groundwater standard limit. The As extraction reducing efficiency of BLDH in soil ranged from 43.5% to 80.1%, suggesting that BLDH has the capacity to stabilize As in soil. In continuous column experiments, the As concentration of the solution leached from the As-contaminated soil was maintained below the Korean municipal groundwater standard limit (0.05 mg/L) for 3 years when applied more than 7% of BLDH in the soil, indicating that BLDH

can be used as a stabilizer to stabilize As under non-equilibrium conditions in the real field. Batch experiments with a high concentration of As and several analyses were performed to understand the As stabilization mechanisms of two LDH stabilizers. Results of SEM/EDS and BET analyses indicated that the Mg-Fe LDH used in this study has a sufficient porous structure, and As was fixed on the outer surface of both PLDH and BLDH. FT-IR and XRD analyses identified the presence of carbonate (CO_3^{2-}) and sulfate (SO_4^{2-}) anions at the interlayer spaces of LDH, and some of the anions were replaced by arsenate during the stabilization process [79]. A schematic illustration of the removal mechanism is shown in Figure 2-6.

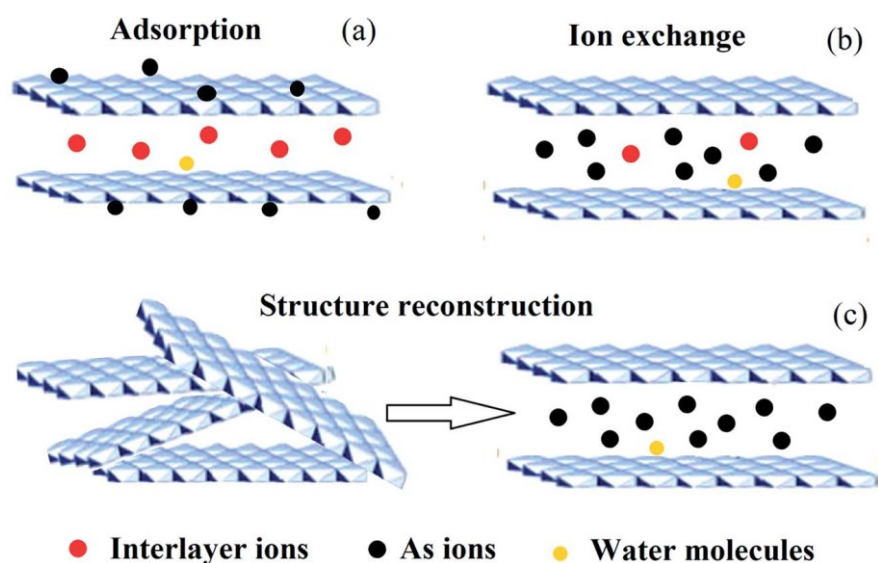


Figure 2-6: A schematic illustration of the As removal mechanism using a LDH.

2.4.2.7 Metal Organic Framework (MOF)

Due to their excellent adsorption capacity, MOFs and MOF-based composites have increasingly been used in the removal of As(III) and As(V) from water, and combining MOFs with other materials can also be used to remove As(III). As(III) adsorption was well-modeled kinetic and isotherm using pseudo-second-order and Langmuir models respectively. In UiO-66 there are zirconium oxide clusters that provide a large contact area and countless active

sites, which are thought to be hydroxyl groups and BDC groups. A solution of arsenic acid (H_3AsO_4) released H^+ ions, binding to the hydroxyl groups in UiO-66 at pH 2, resulting in the formation of arsenic complexes. UiO-66 had the disadvantage of a long equilibrium adsorption time of 48 h, no data regarding possible reuse was reported, and the adsorption mechanism was mainly ion exchange and coordination with metal nodes of MOFs. Due to the fact that few MOF-based materials are reusable, future research and applications need to be concerned with adsorption equilibrium times and regenerations, as well as adsorption capacity [80]. Using crystal Zn-MOF-74 material, the systemic adsorption of arsenic is explored, which results in ultrahigh adsorption capacities of 325 mg g^{-1} for As(V) and 211 mg g^{-1} for As(III). In the synthesized Zn-MOF-74, the BET surface area is $604 \text{ m}^2 \text{ g}^{-1}$, while the uniform pore size is 1.0 nm. Open-metal sites in MOFs serve as the basis for the development of a new adsorption mechanism by Zinc-O-As cross-linking between them, and this suggests a new avenue for the removal of arsenic through open-metal sites. From pH=3-7, As(V) sorption capacity increases rapidly, followed by a rapid fall between pH=10-12, and As(III) sorption capacity increases rapidly between pH=10 and pH=12. Following the above results, pH 7 was chosen for As(V) and pH 12 for As(III). Therefore, the best adsorption on Zn-MOF-74 would be H_2AsO_4^- or H_2AsO_3^- [81].

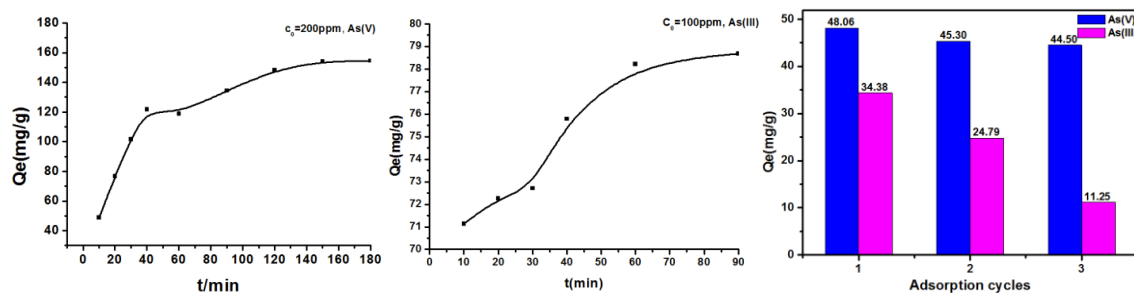


Figure 2-7: adsorption kinetics and cycles result for As(V) and As (III) [81].

2.4.2.8 Graphene Oxide Composites

The removal of heavy metal ions and arsenic (arsenate and arsenite) is very effective with iron oxide-based materials [82]. However, due to their small particle sizes and instability, these adsorbents cannot be used in continuous flow systems because magnetite is highly oxidizing when exposed to the air. In order to overcome this challenge, several researchers have combined iron oxides and carbon nanotubes. Many composite materials have used graphene-based materials such as graphene and chemically modified graphene, such as graphene oxide (GO). As a graphene derivative, graphene oxide (GO) has been extensively explored as an adsorbent, and its ability to bind heavy metal ions is determined by the oxygen-containing functional groups on its surface. Due to their large surface area and stability, magnetite reduced graphene oxide composites for arsenic removal have been synthesized [83]. Figure 2-8 shows Major classification of this materials.

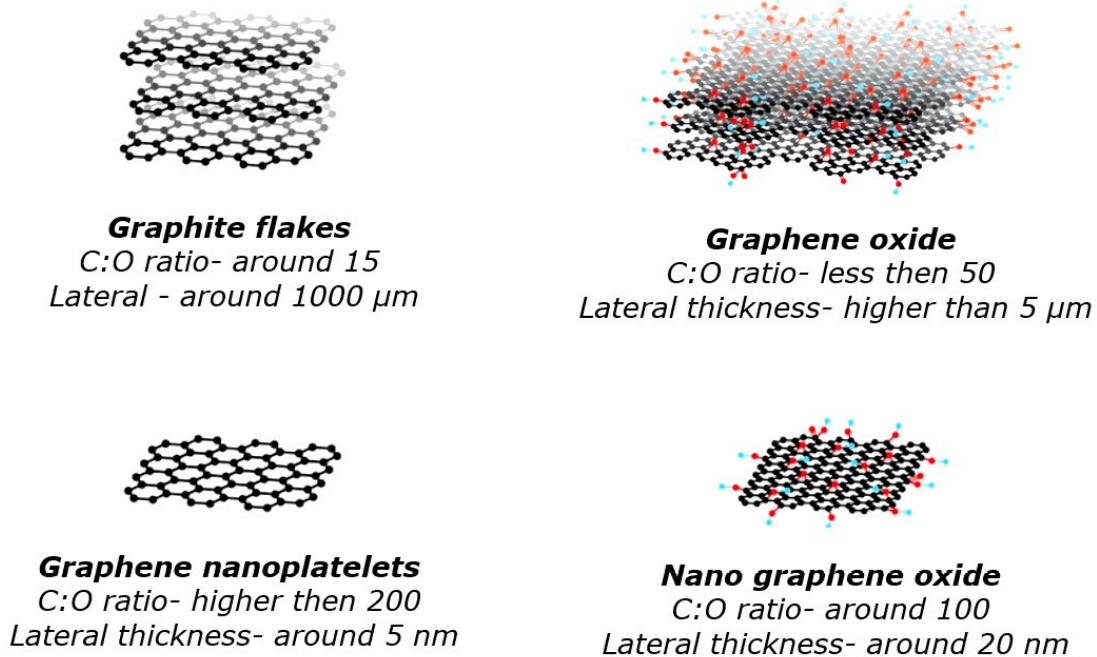


Figure 2-8: Major classification of graphitic materials [84].

An improved Hummers method was used to synthesize GO through the exfoliation of natural graphite flakes [85]. FeO_x-GO composite were synthesized by the co-precipitation by Dr.ye research team on 2017 for removing arsenic from water that shows on Figure 2-9.

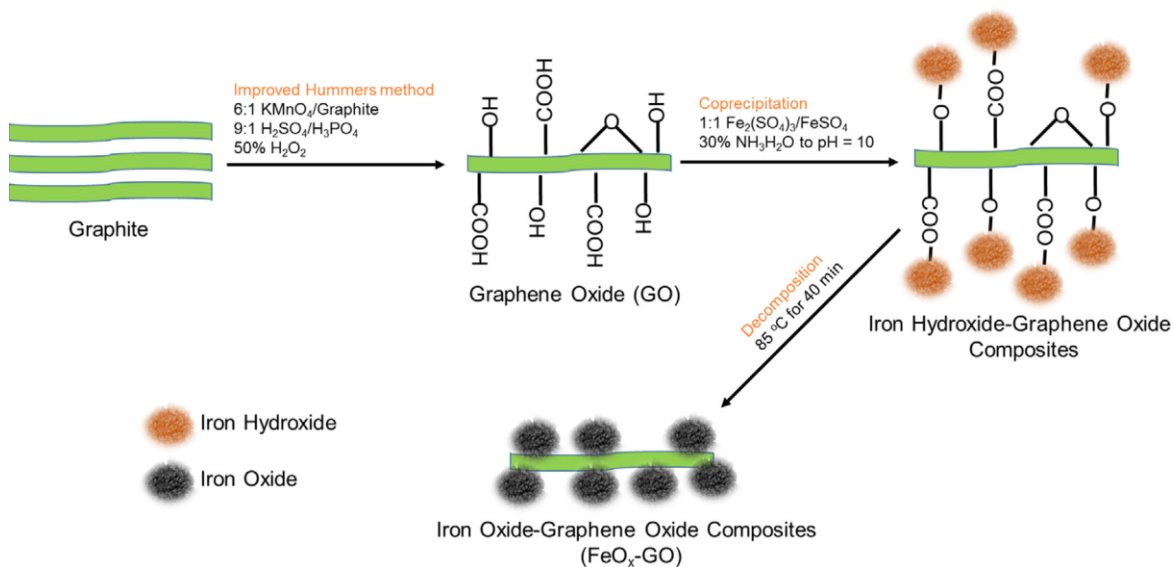


Figure 2-9: Schematic synthesis of FeO_x-GO nanocomposites [86].

both surface area and pore volume show slight increases with the increase of the iron oxide content in adsorbent. FeO_x-GO XRD shows diffraction peaks, which match the diffraction pattern of α -Fe₂O₃. FeO_x-GO-80 shows high adsorption capacity of 147 and 113 mg g⁻¹ for As(III) and As(V), respectively.

a nanocomposite of Fe-Mg oxide synthesized with graphene oxide by one-step coprecipitation. This composite showed adsorption selectivity with high adsorption capacity of 100–600 mg g⁻¹ for heavy metals like Pb²⁺, Cu²⁺, Ag⁺, and Zn²⁺. The adsorption isotherms followed the Langmuir model, indicating monolayer adsorption and the adsorption kinetics followed pseudo-second-order model, suggesting chemisorption. The adsorption is likely to be chemisorption primarily by complexation with certain ion change. The adsorbent could be recycled, maintaining high level of adsorption capacity for heavy metal ions. Thus, the material is potentially useful in treating contaminated water [87]. Figure 2-10 show

adsorption capacity of and FTIR spectra of Fe–Mg (hydr)oxide, GO and Fe–Mg (hydr)oxide@GO.

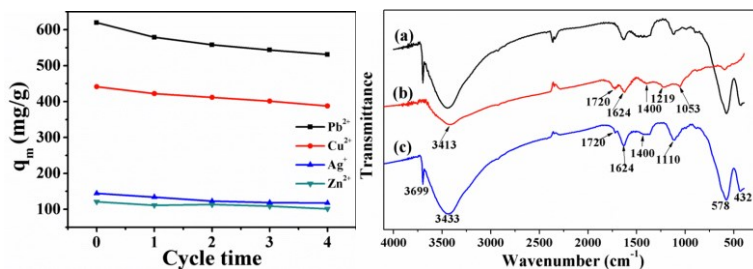


Figure 2-10: adsorption capacity of and FTIR spectra of (a) Fe–Mg (hydr)oxide (b) GO and (c) Fe–Mg (hydr)oxide@GO.

In another research study, the focus was on investigating the efficacy of a novel nanocomposite material, MgO/graphene oxide (MgO/GO), as an adsorbent for the removal of aqueous Congo red (CR) dye. The researchers aimed to explore the potential of MgO/GO in addressing the pressing issue of water pollution caused by dyes. The results of the study revealed that MgO/GO exhibited remarkable adsorption properties, with a rapid adsorption rate and high removal efficiency for CR dye. Equilibration between MgO/GO and CR dye was achieved within a short duration of 10 minutes, with an impressive adsorption percentage of 97.84%. Furthermore, the adsorption quantity reached 684.85 mg g^{-1} , demonstrating the substantial capacity of MgO/GO for CR dye adsorption. The findings of this research highlight the promising prospects of MgO/GO as an effective adsorbent for the treatment of aqueous dyes, emphasizing its potential role in mitigating water pollution and promoting sustainable environmental practices. Figure 2-11 Shows fabrication process of MgO/GO composite [88].

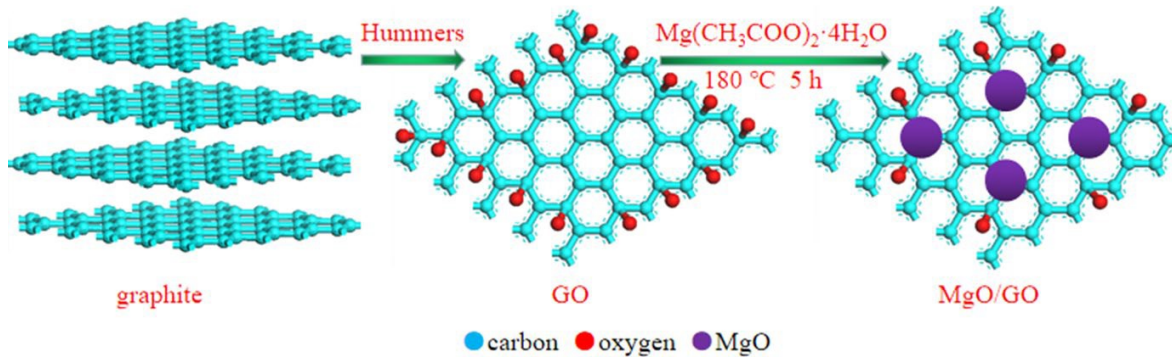


Figure 2-11: Fabrication process of MgO/GO [88].

GO-Fe₃O₄ nanocomposite is synthesized on a large scale by mechanochemical ball milling of graphene oxide and iron powder. The GO-Fe nanocomposites with a 50:50 composition, which were milled for different times, were further characterized by Raman spectroscopy in Figure 2-12 graphene oxide synthesized by Hummer's method showed the D (Defect—structural defects created by the oxidation of Graphene framework) and G (Graphitic—first order scattering of E_{2g}) bands at frequencies ~ 1350 and 1588 cm^{-1} , respectively [89].

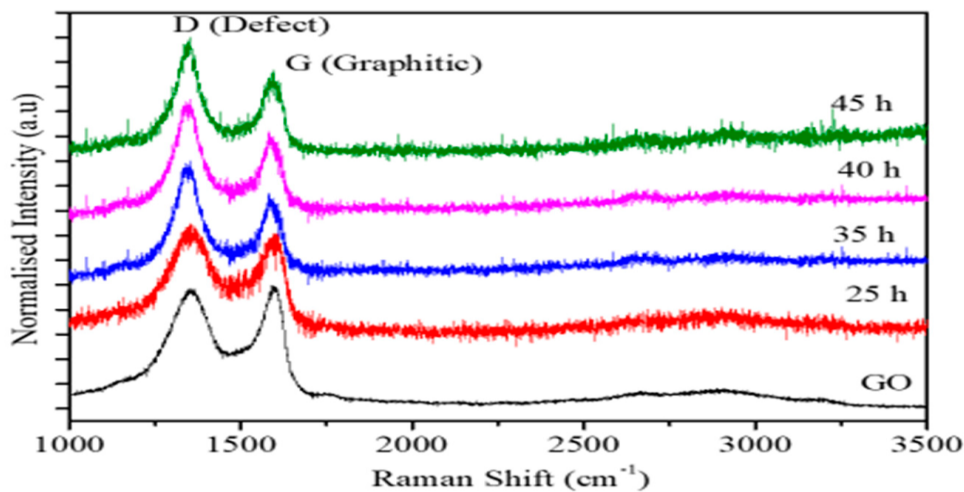


Figure 2-12: Raman spectra obtained from pure GO and GO-Fe nanocomposite for 25, 35, 40, and 45 h [89].

Easy and controllable growth of MgO on the surface of GOs with uniform distribution was synthesized using a simple sol-gel process. The MgO nanoparticles grown on the GOs show

high surface reactivity, and high chemical and thermal stability, which makes MgO a promising material for applications in fields of sensors and catalysis [90]. The pH of point of zero charge (pH_{pzc}) of GO/MgO NCs was determined to be 9.7, 10.5, and 10.5 for ratios 5:1, 1:1, and 1:5, respectively. The GO/MgO nanocomposite with 5:1 ratio demonstrated the highest adsorption capacity as 833 mg g⁻¹ at pH 11 for removal of MB [91]. Figure 2-13 shows XRD patterns of graphene composites.

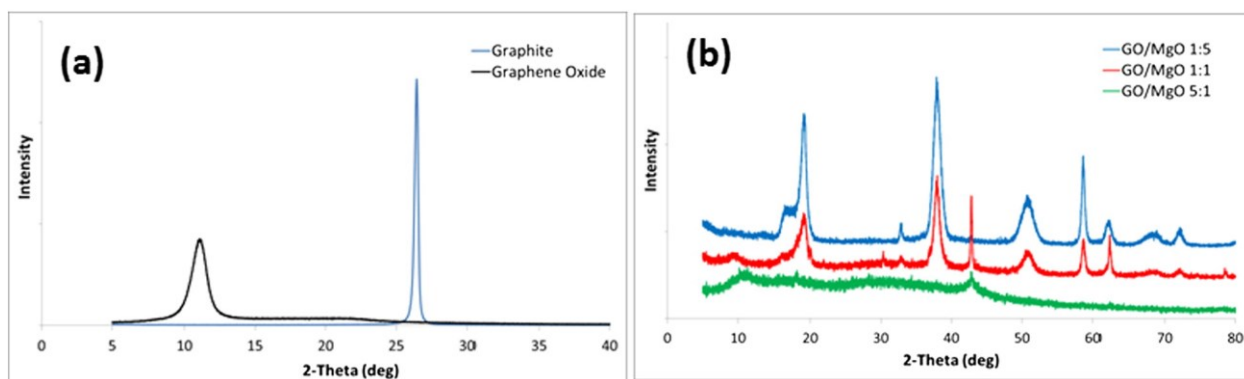


Figure 2-13: XRD patterns: (a) Graphite and Graphene Oxide, (b) GO/MgO NCs for ratios 1:5, 1:1, and 5:1[91].

2.4.3 Challenges and Prospect of Adsorbents

Arsenic is a toxic chemical that can be found in wastewater, and many countries suffer from water that is contaminated with arsenic. WHO has reduced the permissible level of arsenic in water from 50 to 10 ppb, showing that this chemical is a hazard to health and the environment. For removing arsenic from water, a variety of adsorbents are used, such as metal oxides, but they are not suitable for all types of wastewaters due to the wide pH range, so one of the most challenging problems is finding an adsorbent that could be used in a wide range of pH for various types of wastewaters. As another challenge associated with adsorbent is the ability to synthesize low-cost adsorbent; graphene oxide could be used for this purpose so recently graphene oxide is used as an adsorbent for removal impurities from water and wastewater because of its surface area that could be used for removal heavy

metals like arsenic from wastewater. Although graphene oxide has shown excellent adsorption performance, their practical performance still falls short of their potential. To produce high performance adsorbents for the removal of arsenic from wastewater, surface area, regeneration, desorption, and composites with binary metal oxides need to be investigated more. To enhance the performance of graphene oxide composites by enhancing adsorption, the following research directions should be pursued:

- The development of graphene oxide nanocomposites containing layer double hydroxide of Fe/Mg with the purpose of enhancing the adsorption capacity
- Development of techniques for the preparation of adsorbents that are low cost, efficient, scalable, and safe.
- Working with real sample of wastewater and investigating selectivity of the adsorbent for adsorption arsenic from wastewater
- Investigating the ability of regeneration of arsenic from adsorbent to use for cycles during wastewater treatment.
- Increase stability and efficiency of adsorbent during arsenic removal from wastewater.

Graphene oxide composites with unique properties such large surface area, non-toxic nature, good mechanical stability, have shown great promise as active materials for adsorbents. Despite all these distinct features, the graphene oxide nature of these compounds has limited their efficiency. Up to now, numerous graphene oxide nanocomposites with nanoparticles like FeO, MgO have been synthesized to increase their specific surface area and improve the adsorbent capacity. These composites have exhibited higher adsorbent capacitance and stability and reusability compared to other adsorbents. As a new type of adsorbent with high performance, LDH adsorbents for removal arsenic from wastewater will be investigated and for my thesis, graphene oxide with binary metal oxides of iron and magnesium oxide will be synthesized and considered as an adsorbent for removing arsenic from wastewater. Table

0-1 shows the adsorption capacity of different adsorbents for arsenic removal. This table helps to make better comparisons between different adsorbents and the reason why we choose Fe-Mg metal oxide adsorbent for this project.

Table 0-1: Comparison of arsenate adsorption among prevalent adsorbents

Adsorbent	Condition			Adsorption Capacity mg g ⁻¹		Ref.
	BET (m ² g ⁻¹)	pH	Dosage (mg L ⁻¹)	As(III)	As(V)	
Fe-Mg LDH-GO	189	6.8	0.5	186.5	307.7	This work
FeOx-GO-80	341	7	0.8	147	113	[86]
α-Fe2O3	162	neutral	60	95	47	[61]
Fe-Zr binary oxide	339	7	200	120	46.1	[72]
Manganese oxide-coated-alumina	194	7	5	42.48	N.A	[76]
TiO2-Fe2O3 bi-composite	133.5	5	1	N.A	12.4	[53]
γ-Fe2O3 @ carbon	858	7	1	17.9	29.4	[31]
Hydrous TiO2	312	7	0.5	83		[92]
Hydrous TiO2	280	4	0.5		33	[92]
Fe3O4	179		100	46	16.56	[67]
Fe-treated sample	20.9	5.5	3-18		10	[93]
Zn-MOF-74	604	6	1	211	325	[81]
Meso-Al-400	396	7	0.5	115	120	[31]
Magnetite reduced graphene oxide (M_RGO)	148	7	0.2	13	5	[28]
Fe/Mn-C Layered Double Hydroxide Composite	170	2	1.4	46	37	[78]
Mg-Fe layered double hydroxide nanoplates	144	7	0.5	N.A	271	[77]
Mg-Fe-S2O8 LDH	10	4	0.5	75	75	[77]

Chapter 3 Lignin-Polyethylene Composite Adsorbents for Gold Capturing

3.1 Abstract

We report in this paper the synthesis of lignin-polyethylene composite pellet adsorbents for the capturing of Au(III) species from its aqueous solutions and the investigation of their adsorption performances. In this adsorbent design, lignin as an abundant low-cost biopolymer is employed as the active adsorbing material while polyethylene serves as the inert binder that maintain the structural/mechanical integrity of the adsorbents. Systematic characterizations have been undertaken on the composite adsorbents. A thorough investigation on the adsorbent performances has been performed, including the effects of pellet composition, adsorbent dosage, pH, and co-existing ions on the adsorption, as well as the adsorption kinetics, isotherm, and reusability. The highly selective gold capturing has been demonstrated with the composite adsorbent L40-PE60. This work shows the strong potential of the lignin-polyethylene composite pellet adsorbents for the industrial gold capturing in gold mining processes.

Keyword: lignin, polyethylene, adsorbent, composite, gold capturing

3.2 Introduction

Gold mining and use have a history that is as old as human civilization. Gold mining is typically carried out by crushing, grinding, leaching, and adsorption, then by stripping, electrowinning, and recovering of the gold. Currently, cyanide and chloride leaching are the most popular leaching techniques. Cyanide leaching is less prevalent than chloride leaching due to the toxicity of cyanide and its inefficiency in refractory ores and concentrates [9][10]. In the circuit of gold mining, adsorption is often used in a process called Carbon-in-Leach

(CIL) or Carbon-in-Pulp (CIP). In this process, activated carbon is used as an adsorbent to capture gold particles from a solution of gold-containing leachate. The activated carbon is then separated from the leachate, and the gold species is then removed from the activated carbon by a stripping process known as elution. Traditional activated carbon adsorbents are relatively expensive and not very effective in capturing gold in certain conditions. Therefore, alternative cost-effective adsorbents are needed to improve the efficiency of gold capturing in gold mining processes [77].

Lignin is one of the three essential components from wood and also one of the most abundant biopolymers next to cellulose and chitin. The amount of total lignin biomass was estimated to be about 300 billion tons annual production in 2012. Kraft lignin, as the main form of lignin, is separated from the cellulose fibers during the kraft pulping process. Approximately 98% of the produced lignin is utilized as fuel, whereas only a small proportion of 2% is employed for value-added purposes [19][20]. The chemical structure of lignin is complex [18]. Methoxy, hydroxyl, carboxyl, and aldehyde groups are only a few of the functional groups that make up the complex three-dimensional aromatic structure of lignin. These characteristics of lignin indicate that it may be exploited as a potential adsorption material in the elimination of heavy metals from wastewater [22]. A quantitative and mechanistic study on the adsorption of various metal ions, including Cr(VI), Pb(II), Cu(II), Cd(II), Zn(II), and Ni(II), on lignin had been undertaken, demonstrating the affinity of these heavy metal ions towards lignin [24]. In particular, crosslinked lignin-based gels were also demonstrated to show more selective adsorption of Au(III) than activated carbon, with strong promise for the efficient recovery of Au(III) [1].

The use of lignin as a sustainable adsorbent for the recovery of gold, is not only an effective strategy for the extraction of the precious metal, but also offers a value-added application of this abundant industry byproduct [23]. Despite its strong affinity to gold ions, lignin alone, as a brittle material at low temperatures, may not have sufficient structural integrity and

tend to get pulverized in the industrial gold capturing process, rendering difficulties for separation following adsorption. To tackle this, we have herein compounded lignin with polyethylene (PE) to prepare lignin-PE composite adsorbents. As a chemically inert and mechanically strong material, PE acts as a binder for lignin, maintaining the mechanical integrity of the adsorbents. In this study, lignin-PE composite adsorbents have been systematically investigated for their performances towards the adsorption of Au(III), with their potential for industrial gold capturing revealed.

3.3 Experimental

3.3.1 Materials

Lignin (35% moisture) was obtained from Domtar (USA) and was dried overnight in a vacuum oven at 100 °C. Pellets of medium density polyethylene (MDPE) were obtained from Nova Chemicals (Canada), and were used as received without any additional purification. Deionized water was obtained from a MilliporeSigma™ Milli-Q™ ultrapure water purification system. Gold(III) chloride trihydrate ($\geq 99.9\%$, trace metals basis, Aldrich) was selected as the source of Au(III). A stock solution of Au(III) containing 1000 mg L⁻¹ of gold was prepared in deionized water. Various concentrations (1-1000 mg L⁻¹) of gold standard solutions were subsequently prepared by diluting the stock solution with the pH adjusted using HNO₃ or NaOH.

3.3.2 Preparation of adsorbent pellet

In this study, two lignin-PE composites adsorbents, L20-PE80 and L40-PE60 at lignin contents 20 and 40 wt%, respectively, were compounded in the form of pellets by an extrusion method. Generally, each pellet is at about 10 mg with the geometric size of around 4 mm in length and 2 mm in diameter. Figure 0-1 shows the schematic production of the composite pellets and their dimensions. The pellets of PE and lignin were manually dry

blended before feeding to the extruder. The composites were produced on a co-rotating twin-screw extruder Leistritz ZSE-27 (D = 27 mm, L/D = 40; Leistritz, Germany). The screw speed was fixed at 60 rpm with the total follow rate at 4 kg h⁻¹. The temperature profile from the main feed to the die (3 mm) was: 120 /145 /145 /145 /145 /145 /145 /145 /145 /135 °C. The extrudate was cooled down at the die exit using a water bath before being air dried and fed to a pelletizer (Conair model 304 pelletizer; Stanford, USA).

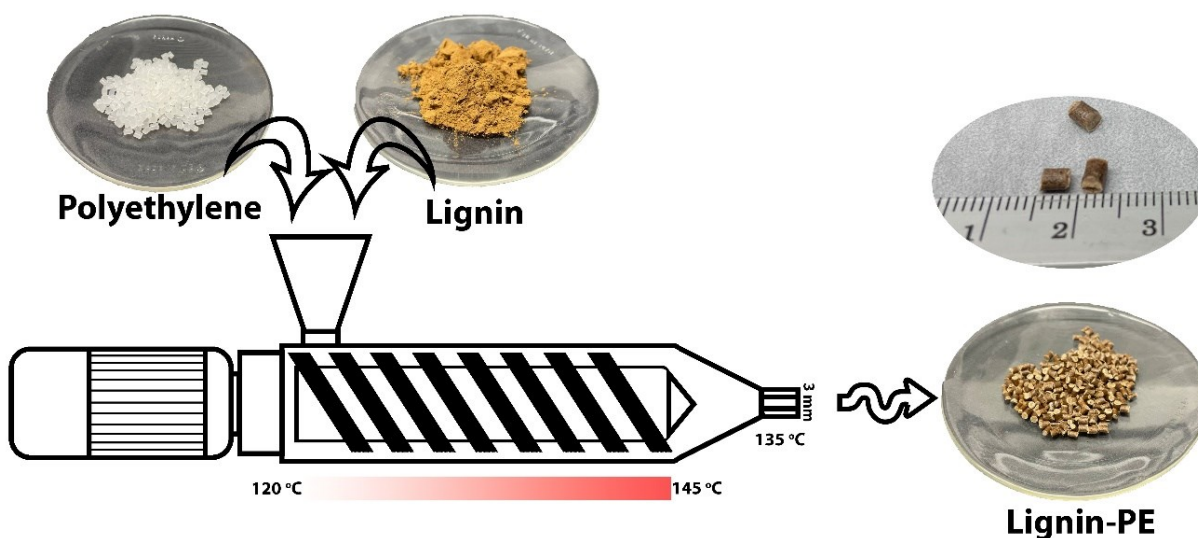


Figure 0-1: Schematic production of lignin-PE composite pellets and pellet dimensions.

3.3.3 Characterization

Braunauer–Emmett–Teller (BET) specific surface area, pore volume, and pore size distribution of the composite samples were determined by N₂ sorption at 77 K on a Micromeritics 3Flex Surface and Catalyst Characterization analyzer. Before the sorption measurements, the samples were degassed under vacuum at 110 °C for at least 12 h. Wide-angle X-ray diffraction (XRD) patterns of the composites were recorded on a Rigaku Smartlab SE X-ray diffractometer with Cu radiation (3 kW; wavelength 1.54 Å) at room temperature.

Fourier-transformed infrared (FTIR) spectra were obtained on a Thermo Scientific Nicolet 6700 Analytical FTIR spectrometer. Thermogravimetric analysis (TGA) of the composite pellets was carried out on a TA Instruments Q50 TGA. Measurements were performed in an air atmosphere. In a typical measurement, the sample (10 mg) was heated to 100 °C at a rate of 10°C min⁻¹, held at 100 °C for 10 min, and then heated to 700 °C at a rate of 10 °C min⁻¹. The concentration of gold was measured with an Agilent 7500ce inductively coupled plasma mass spectrometry (ICP-MS) within the concentration range of 0.01-10 mg L⁻¹. A solution of gold ICP-MS standard was diluted with 5% HNO₃ to prescribed levels, which were measured with ICP-MS to construct a calibration curve.

3.3.4 Gold adsorption

All the adsorption experiments with the composite adsorbents toward Au(III) were carried out in the batch mode at room temperature, i.e., around 23 °C. The effects of process parameters, including pH (1-7), contact time (1-360 min), initial Au(III) concentration (1 µg L⁻¹ -1000 mg L⁻¹) and adsorbent dosage (25-150 mg mL⁻¹) have been evaluated. Moreover, the effects of several interfering ions, including As(III), As(V), Cu²⁺, Mg²⁺ and Na⁺ ions, have also been evaluated. Typically, the composite adsorbent (50-300 mg) was dispersed in 2 mL of Au(III) solution at different initial concentrations (1 µg L⁻¹ -1000 mg L⁻¹) and pH values, followed by magnetic stirring (300 rpm) for 6 h to achieve adsorption equilibrium. Afterward, a 0.2 µm Teflon syringe filter was used to filter the suspension, and the equilibrium concentration of non-adsorbed Au(III) in the filtrate solution was quantified. The equilibrium adsorption uptake (q_e in mg g⁻¹) was calculated by using the mass balance equation [77]:

$$q_e = \frac{c_0 - c_e}{m} V \quad (1)$$

where c_0 (mg L⁻¹) and c_e (mg L⁻¹) are the initial and equilibrium concentration of Au(III), V (L) is the total solution volume and m (g) is the adsorbent mass.

The adsorption isotherms were fitted with different models, with the best fit found with the Freundlich model (Eq. 2). where k_d is the distribution coefficient, and n is a correction factor.

$$q_e = k_d C^{1/n} \quad (2)$$

To obtain the adsorption kinetic curve of L40-PE60, the composite adsorbent (10 mg) was dispersed in a series of Au(III) standard solutions of the same volume (2 mL) at Au(III) concentration (10 mg L⁻¹). After stirred for a different prescribed period of time (from 1 to 360 minutes), each dispersion was rapidly filtered with the filtrate measured for the equilibrium concentrations of Au(III) to determine the time-dependent adsorption uptake. A pseudo-second-order kinetic model was used to fit (Eq. 3 and 4) the adsorption kinetics, based on which the initial adsorption rate was calculated (Eq. 5).

$$\frac{dq_t}{dt} = k_2(q_e - q_t)^2 \quad (3)$$

$$\frac{t}{q_t} = \frac{1}{(k_2 q_e^2) + \frac{t}{q_t}} \quad (4)$$

$$V_0 = k_2 q_e^2 \quad (5)$$

Where q_t is the adsorption uptake (mg g⁻¹) of Au(III) at various time t , k_2 is the rate constant (g mg⁻¹ min⁻¹), q_e is the equilibrium adsorption uptake (mg g⁻¹), and V_0 is the initial adsorption rate (mg g⁻¹ min⁻¹).

3.4 Result and Discussion

Two lignin-polyethylene composite adsorbents, L20-PE80 and L40-PE60 with the lignin content of 20 and 40 wt%, respectively, have been produced in the pellet form with an average size of around 2 mm through melt extrusion compounding followed by pelletization. Figure 3-2 shows the XRD patterns of L40-PE60, pure lignin and PE. In the pattern of the pure lignin, a broad amorphous peak centered at around 22° is observed while with no other distinct peaks, suggesting its amorphous structure [94] [95]. L40-PE60 shows

diffraction peaks at 2θ of 22° , 24° characteristic of orthorhombic crystal structure of polyethylene [25].

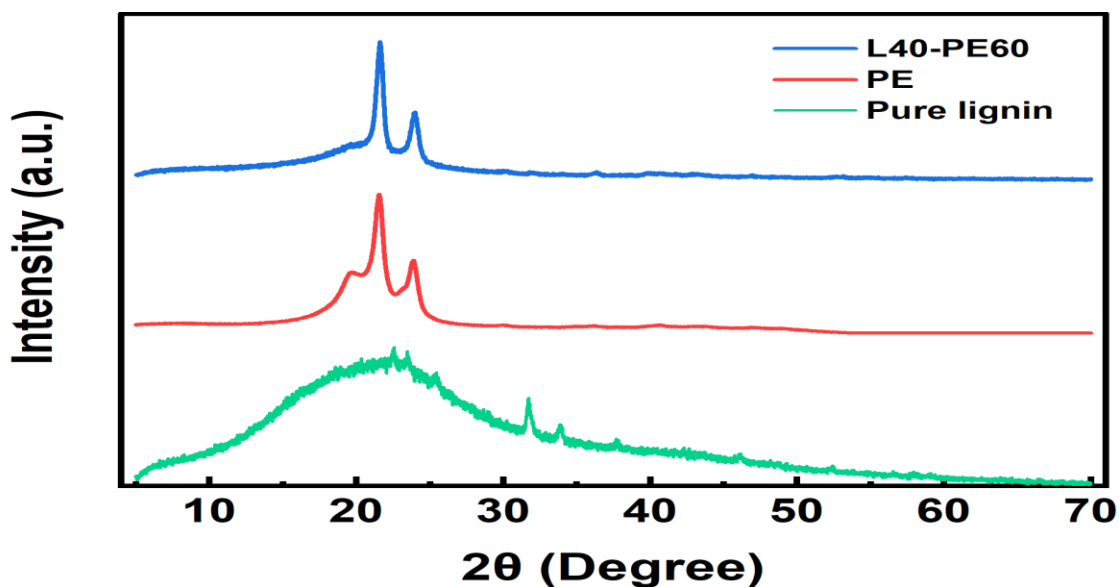


Figure 3-2: Wide-angle XRD patterns of L40-PE60, pure lignin and PE.

Figure 0-3 shows FTIR spectra of pure lignin, polyethylene, and L40-PE60. The pure PE shows three sets of bands, corresponding to C-H stretching, CH_3 bending, and CH_2 vibration at approximately $2900\text{--}2850$, $1490\text{--}1460$, and $750\text{--}720\text{ cm}^{-1}$, respectively [96]. Pure lignin shows a broad strong band at around 3400 cm^{-1} , attributable to the stretching of aliphatic and phenolic hydroxyl groups. Stretching bands of C-H bonds in the methyl and methylene groups of side chains and aromatic methoxyl groups are also seen at around 2930 cm^{-1} . Meanwhile, some characteristic bands arising from the functional groups in lignin are observed in the range of $1000\text{--}1800\text{ cm}^{-1}$. A band at 1704 cm^{-1} corresponds to the stretching vibration of the carbonyl/carboxyl region. Carbonyl group stretching vibrations, aromatic skeleton vibrations, or impurities and water linked to lignin are the causes of the vibration at 1595 cm^{-1} . Another band at 1083 cm^{-1} arises from vibrations of the C-O bond in secondary alcohols and aliphatic ethers [97–99]. These characteristic lignin bands are, somehow,

significantly weakened in L40-PE60, indicating the loss of some functional groups during the extrusion process [99].

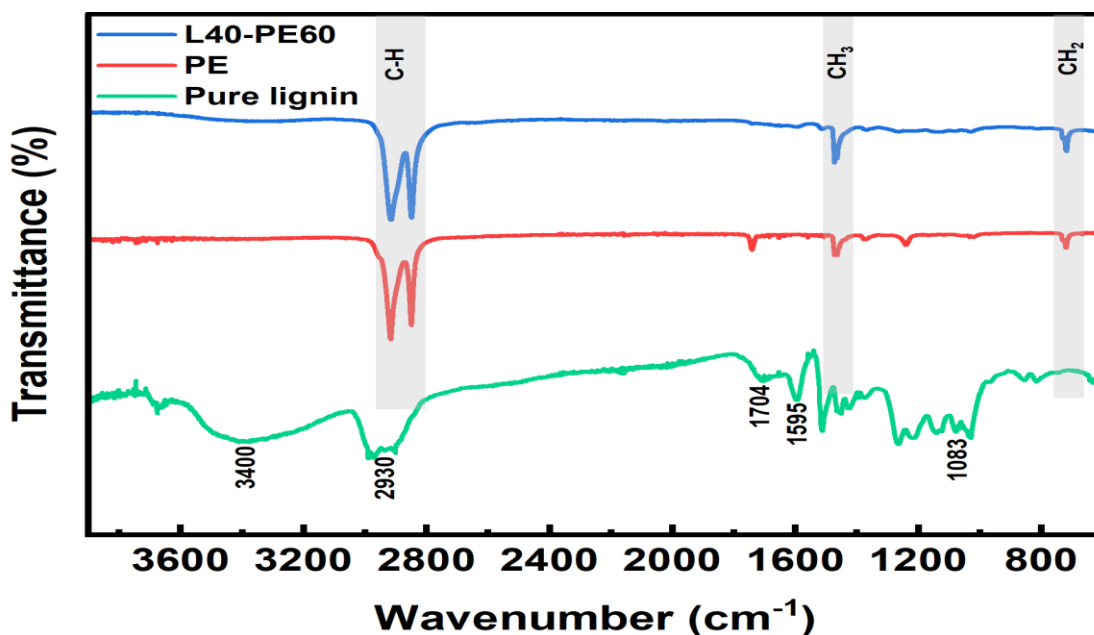


Figure 0-3: FTIR spectra of L40-PE60, pure lignin and PE.

Figure 0-4 shows the TG and corresponding differential curve of L40-PE60 in air, as well as those of pure lignin and PE for comparison. The pure lignin degrades with the continuous weight loss over a very broad temperature range from 100 - 500°C, with the major weight loss attributable to the thermo-oxidative degradation of lignin macromolecular chains within 450-500 °C [94]. For pure PE, the degradation occurs primarily within 300-470 °C. L40-PE60 resembles the degradation profile of the pure lignin, with the gradual weight loss within 100-500 °C and the major loss within 450-500 °C.

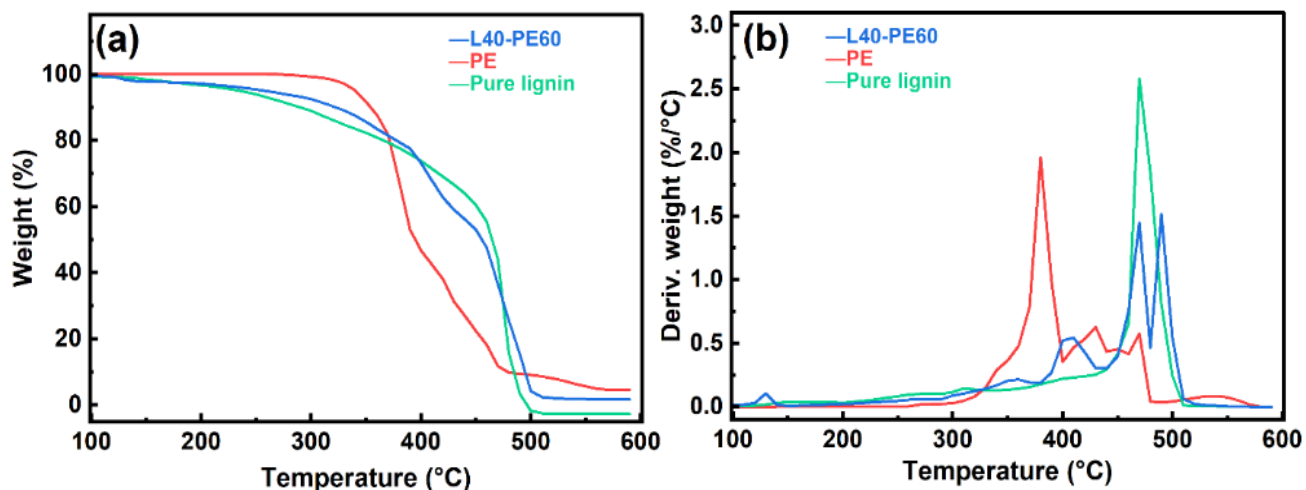


Figure 0-4: TGA curves for pure lignin, PE and pellet composites in the air atmosphere.

N₂ sorption analysis at 77 K reveals that pure lignin and the two composites are nearly nonporous with negligible surface area (2.12 and 1.74 m² g⁻¹ for pure lignin and L40-PE60, respectively) or pore volume.

A systematic investigation on the performance of two lignin-PE composite pellets for the batch adsorption of Au(III) has been undertaken, along with the comparison with pure lignin as the control adsorbent. Figure 0-5 shows the adsorption capacity and percent of Au(III) removal of the three adsorbents toward Au(III) at the initial Au(III) concentration of 515 mg L⁻¹, adsorbent dosage of 100 mg L⁻¹, and pH of 6. Pure lignin has the incredible result with 99.99% of gold capture and 5.15 mg g⁻¹ of adsorption capacity. Although with no significant difference in the surface areas of the three composites, the significant increase in the percentage of adsorption from L20-PE80 to L40-PE60 is seen, which is due to the creation of a greater number of lignin active sites with higher adsorption affinities per unit area due to the increased lignin content. Lignin is a complex polymer that contains many ether linkages, and protonation at these ether groups is known to result in a positive charge on the surface of the lignin matrix. This positive charge is believed to play a role in the adsorption of Au(III)

on lignin in a hydrochloric acid medium. Specifically, it has been proposed that anion exchange occurs between the chloride ion and the chloroaurate anion, followed by an electrostatic interaction between the anionic species of Au(III) and the oxonium center of the adsorbent [23].

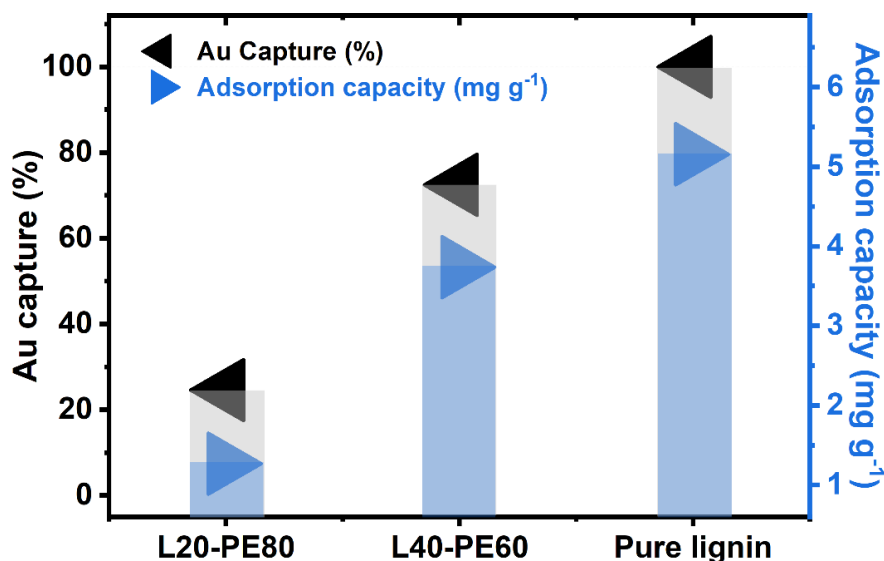


Figure 0-5: Gold adsorption capacity and capturing percentage for various adsorbents towards the adsorption of Au(III) at adsorbent dosage of 100 mg L⁻¹, Au(III) initial concentration of 515 mg L⁻¹ and pH = 6.

We have subsequently investigated the effect of the dosage of L40-PE60 on the adsorption of Au(III). Figure 3-6 shows the adsorption capacity and the percent removal of Au(III) at initial Au(III) concentration of 12 mg L⁻¹ and pH 6. When the adsorbent dosage increases from 27 mg L⁻¹ to 100 mg L⁻¹, the percentage of adsorption increases from 93% to 99%. This results from the greater availability of active sites for ion sorption at higher adsorbent doses. However, when the adsorbent mass was further increased from 100 to 150 mg/mL, there is only a small (less than 1%) difference in the removal percentage. It is worth noting that the adsorption capacity of the pellets decreases with increasing adsorbent dosage, suggesting that an optimal adsorbent dosage of 100 mg L⁻¹ from these tests. Based on the findings, it can be inferred that increasing the adsorbent dosage enhances the availability of active sites for

gold capture, leading to a more efficient medium for gold adsorption. However, the experimental results demonstrated a decrease in adsorption capacity with higher adsorbent dosage. This observed behavior can be attributed to the equation governing adsorption capacity, which indicates an inverse relationship between dosage and adsorption capacity while the number of active adsorption sites increases. The adsorption capacity is influenced by factors such as adsorbent dosage, as well as the initial and final concentration of the solution. Therefore, optimizing the adsorbent dosage becomes crucial to strike a balance between the number of active sites and adsorption capacity, ensuring effective gold capture.

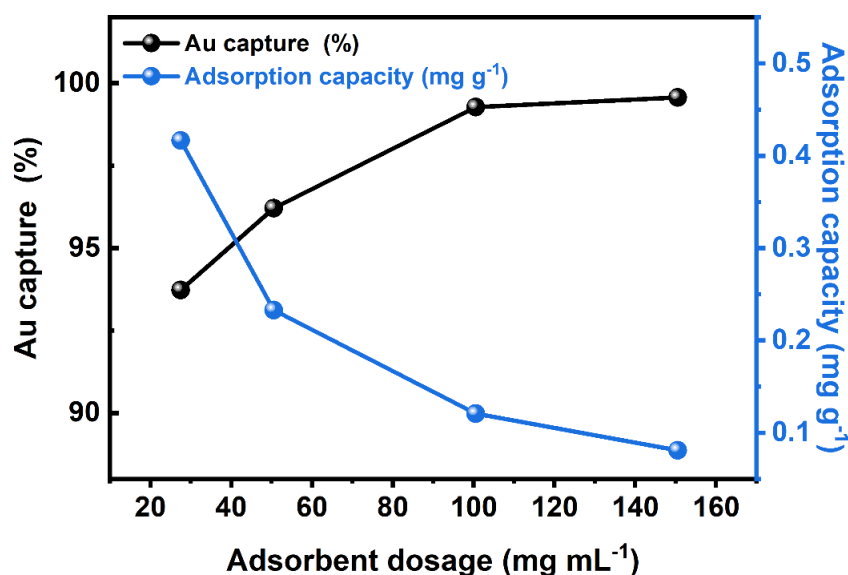


Figure 3-6: Effects of dosage of L40-PE60 on the adsorption capacity and percent removal of Au(III) at initial Au(III) concentration of 12 mgL⁻¹Au(III) and pH 6.

It has been proven that pH is a key parameter in adsorption processes as it affects the adsorbent surface charge and chemistry of the metals in solution. Figure 0-7 shows the influence of pH on the adsorption performance of L40-PE60 at the initial Au(III) concentration of 6 mg L⁻¹ and adsorbent dosage of 100 mg L⁻¹. Since lignin dissolves in a basic media, the pH effect was only investigated in the acidic range. With the increase of pH from 1 to 3, the percentage of adsorption increases slightly from 99 to 99.9. The subsequent

increase in pH from 3 to 7 instead leads to the quick decrease in the percentage of adsorption to %66. The ability of the adsorbent to bind Au(III) improves with increasing pH values and peaks at about pH=3 and then decreases with increasing pH [100]. This finding aligns with previous research on gold adsorption systems. The observed trend can be attributed to the pH-dependent changes in the speciation and surface charge characteristics of both the gold ions and the lignin adsorbent. These findings contribute to our understanding of the pH-mediated adsorption mechanisms involved in gold removal using lignin-based adsorbents and can guide future efforts in designing efficient gold recovery processes [101].

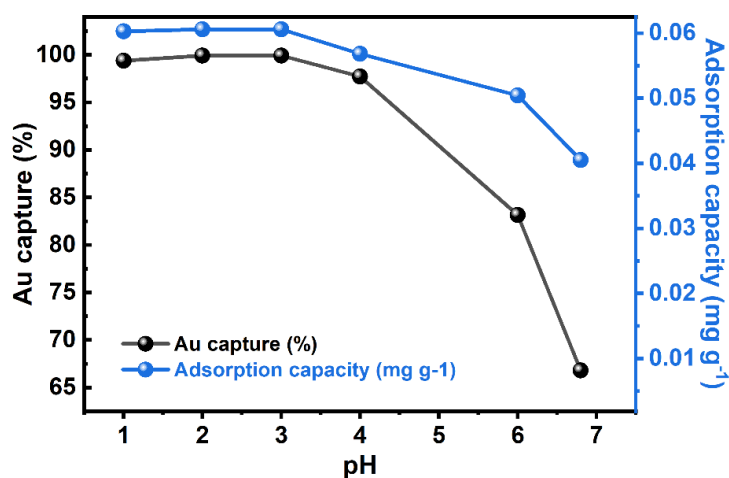


Figure 0-7: Effects of pH on the adsorption capacity and percent removal of Au(III) with L40-PE60 at initial Au(III) concentration of 6 mg L⁻¹ and adsorbent dosage of 100 mg L⁻¹.

The adsorption kinetics with L40-PE60 has been investigated by monitoring the concentration of the adsorbate in the solution at different time intervals. Figure 0-8(a) illustrates the time-dependent adsorption capacity and percent removal of Au(III) with L40-PE60 at the initial Au(III) concentration of 10 mg L⁻¹, adsorbent dosage of 100 mg L⁻¹, and pH=6. The absorption of Au(III) can be separated into two stages: a quick uptake during the first three minutes of contact and a slower uptake after that equilibrium is achieved. The fact that 60% of the gold uptake occurs during the first three minutes highlights the extremely

rapid rate of adsorption. After that, the process moves forward at a slower rate, which is caused by the growth of adsorbed gold ions on the surface of the adsorbent and the consequent reduction in gold ion-accepting sites [23][24]. The adsorption kinetics has been fitted with different models, including pseudo first and second order, Elovich and intra particle diffusion models (see Table 0-1). Figure A1 displays fitting graphs with different kinetic models, while Table S1 provides a summary of the corresponding fitting data and parameters. The best fit with the highest correlation coefficient of 0.999 is achieved with the pseudo-second-order kinetic model (see Figure 0-8(b)). In the pseudo-second-order model, it is assumed that the rate-limiting step of the adsorption process is the chemical interaction between the adsorbate and the adsorbent surface, resulting in the formation of a chemical bond. It thus indicates that the chemical interactions between the adsorbate and adsorbent surface of L40-PE60 dominate over physical interactions, such as Van der Waals forces or electrostatic interactions.

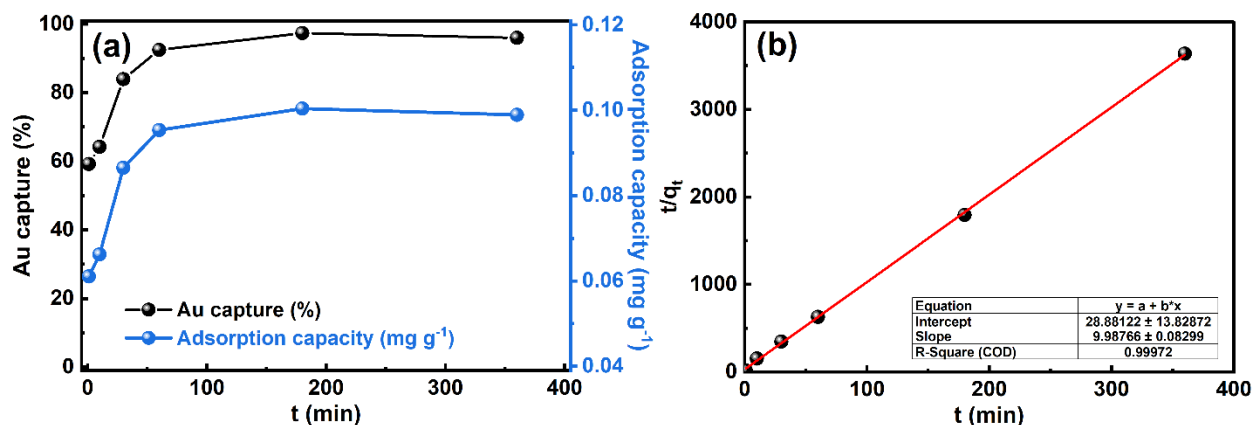


Figure 0-8: (a) Adsorption kinetics with L40-PE60 for Au(III) at initial Au(III) concentration of 10 mg L⁻¹, adsorbent dosage of 100 mg L⁻¹ dosage, and pH of 6 and (b) fitting of the kinetic curves with the pseudo-second-order model.

Table 0-1: List of adsorption kinetic models

Kinetic models	Equation
Pseudo-first order	$\ln(q_e - q_t)/q_e = -kt$
Pseudo-second order	$t/q_t = 1/h + t/q_e$ $h = k_2 q_e^2$
Elovich	$q_t = \frac{1}{\beta} \ln(\alpha\beta) + \frac{1}{\beta} \ln(t)$
Intra Particle Diffusion	$q_t = C + K_D t^{0.5}$

The adsorption isotherm with L40-PE60 has been established by measuring the equilibrium adsorption capacity of Au(III) at different initial Au(III) concentrations but at the same adsorbent dosage of 100 mg L⁻¹ and pH of 6. The isotherm has been fitted with three different models (see Table 3-2). Figure A2 shows the fitting curves. All the constants and parameters for these models are shown in Table A2. The Freundlich model on the assumption of multilayer adsorption on a homogeneous surface provides the best fit for the isotherm. The data and Freundlich model fitting are shown in Figure 0-9(a) and b for Au(III).

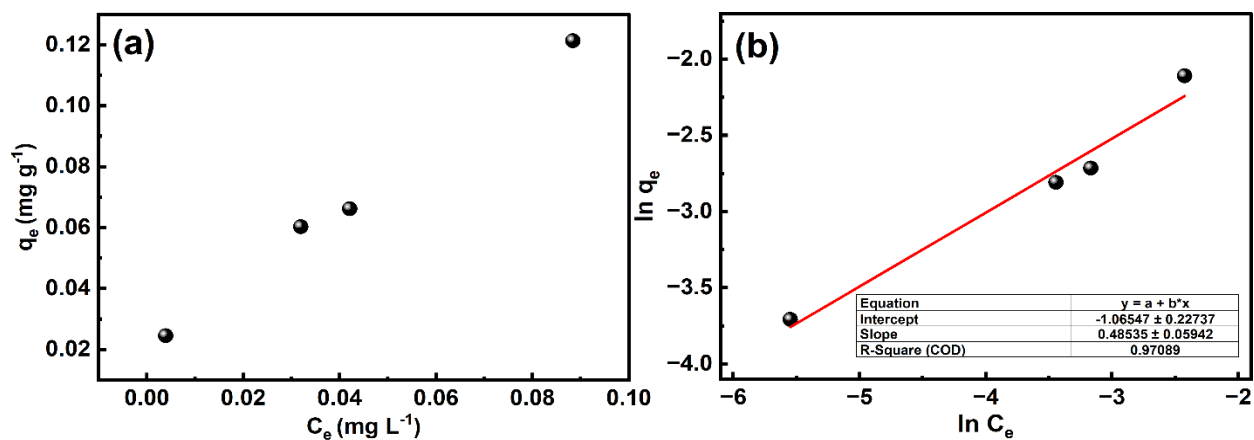


Figure 0-9: (a) Adsorption isotherms of L40-PE60 for both Au(III) at pH 6, and (b) fitting with Freundlich model.

Table 3-2: List of adsorption isotherm models

Isotherm	Equation
Langmuir	$\frac{C_e}{q_e} = \frac{1}{q_m} C_e - \frac{1}{K_L q_m}$
Freundlich	$\ln q_e = \ln K_F + \left(\frac{1}{n}\right) \ln C_e$
Tempkin	$q = \frac{RT}{b_T} \ln K_T C_e$

The effects of coexisting ions (As(III), As(V), Cu²⁺, Mg²⁺, and Na⁺) on the batch adsorption of Au(III) have also been investigated with L40-PE60 at the initial Au(III) concentration of around 6 mg L⁻¹ and adsorbent dosage of 200 mg in 2 mL. The concentration of the coexisting ions, including NaAsO₂, Na₂HAsO₄, Mg(NO₃)₂, CuCl₂ and NaNO₃, was set excessively at 10 times of that of Au(III). Each adsorption underwent for 6 h under stirring. Afterwards, the suspension was filtered, and the filtrate was analyzed with ICP-MS for equilibrium gold concentration. Table 3 summarizes the percentage of adsorption of L40-PE60 for gold ions

in the presence of the various interfering ions. It is obvious that these coexisting ions have only negligible/minor effects on the capturing of gold ions with L40-PE60.

Table 3-3: Effects of interfering metal ions on the adsorption capacity of L40-PE60 for Au(III).

Co-existing ions	Initial concentration (mg L ⁻¹)		Final concentration (mg L ⁻¹)		Capture %	
	Each element	Au (III)	Each element	Au (III)	Co-existing element	Au(III)
None	-	10.31	-	0.004	-	99
AsO ₂ ⁻ (III)	53	10.31	53	0.135	0	99
HAsO ₄ ²⁻ (V)	70.5	10.31	70	0.21	0	98
Cu ²⁺	65.96	10.31	49.5	0.005	25	99
Na ⁺	83.6	10.31	76.9	0.004	8	99
Mg ²⁺	49.52	10.31	49	0.004	1	99

Figure 0-10 presents a comparison between the first and second cycles of gold capture percentages at different initial concentrations of gold. Following the initial adsorption cycle, where the adsorbent is immersed in deionized (DI) water and subsequently dried for reuse in the second cycle, there is a slight decrease in gold adsorption at each initial concentration. This finding suggests that the adsorbent utilized in this study exhibits a level of stability in aqueous environments and retains its effectiveness in absorbing Au(III). This characteristic of the adsorbent holds significant implications for its potential practical application. The ability to reuse the adsorbent multiple times is advantageous from an economic and environmental standpoint. Furthermore, its stability in aqueous environments promotes its longevity and durability in real-world applications. Further research and development in this area could lead to the optimization and refinement of the adsorbent's capabilities, contributing to more sustainable and efficient gold extraction methods in the future.

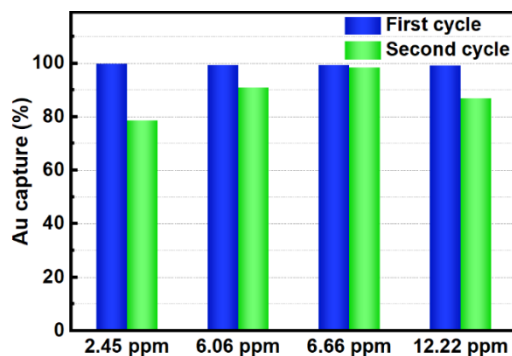


Figure 0-10: First and second cycle gold adsorption by L40-PE60 in different initial concentration, 100 mg L⁻¹ dosage and pH=6.

3.5 Conclusion

In conclusion, this study has demonstrated the potential of lignin-PE composites as a cost-effective and environmentally friendly alternative for capturing gold ions in aqueous media. Two lignin-PE composite adsorbents with two different compositions, L40-PE60 and L20-PE80, have been compounded and evaluated for gold capturing. The composite adsorbents have been characterized with TGA, FTIR, XRD and BET. The adsorption results show that the composite adsorbents can effectively adsorb gold ions from aqueous solutions, with a high adsorption capacity and fast kinetics. Also, it is revealed that the composition of the composite plays a critical role in determining the adsorption capacity, with L40-PE60 of the higher content of active lignin showing higher capacity relative to L20-PE80. A study on the effect of pH shows that L40-PE60 has the better uptake of gold in the acidic media with pH below 4 since the positively charged surface of lignin is beneficial to the adsorption of negatively charged gold complex. An increase in pH above 4 leads to the reduced adsorption. It is discovered that the adsorption kinetics follows the pseudo-second order chemisorption and the adsorption isotherm follows the Freundlich model. Moreover, L40-PE60 displays high selectivity towards Au(III) adsorption in the presence of other co-existing metal ions. In consideration of the high adsorption performance and the low costs

of both lignin and polyethylene, this class of composite adsorbents have high potential for the industrial capturing of gold in gold mining processes.

Chapter 4 Mg–Fe Layered Double Hydroxide-Graphene Oxide Nanocomposite Adsorbents for Arsenic Removal

4.1 Abstract

We report in this paper the synthesis of a range of Mg–Fe layered double hydroxide (LDH)-graphene oxide (GO) nanocomposite adsorbents for arsenic removal. Synthesized by a coprecipitation method, the LDH-GO composites are featured with 2-dimensional GO nanosheets decorated with LDH particles, which are designed with different Fe/(Fe+Mg) molar ratios ($x = 0.26, 0.42, \text{ and } 0.6$), at different mass contents (20, 50, and 80 wt%). In parallel, $\alpha\text{-Fe}_2\text{O}_3\text{-GO}$ and $\text{Mg}(\text{OH})_2\text{-GO}$ counter composites have also been synthesized for the purpose of comparison. All the composite adsorbents have been thoroughly characterized for their structural, textural, and physiochemical properties, and systematically investigated for their performances towards the adsorption of both As(III) and As(V) with the objective of establishing their structure-performance relationships. Among them, the best-performing LDH-GO composite, LDH0.42-80-GO20 that has the optimum x of 0.42 and LDH content of 80 wt%, shows the highest As(V) adsorption capacity and second highest As(III) adsorption capacity (only second to F80-GO20, the $\alpha\text{-Fe}_2\text{O}_3\text{-GO}$ composite with $\alpha\text{-Fe}_2\text{O}_3$ content of 80 wt%) due to its high surface area and high zeta potential. In particular, its enhanced zeta potential results from the incorporation of Mg-based hydroxide known for higher point of zero charge within the LDH structure, benefiting the adsorption of As(V) that is often present in the form of anions. The arsenic adsorption capacities of LDH0.42-80-GO20 compares very well relative to some best-performing hydroxide- and oxide-based adsorbents reported to date. This work provides valuable insights towards the rational design of high-capacity adsorbents for arsenic removal.

Keyword: Graphene oxide, layered double hydroxide, composite, adsorbent; arsenic; water treatment

4.2 Introduction

Groundwater contamination with arsenic has become a severe problem for humanity due to its high toxicity. Mining is one of the main causes of arsenic (As) in groundwater. As-containing minerals are frequently found in gold (Au)-bearing ore deposits, therefore gold mining in particular produces significant amounts of As in wastes [102]. According to the 2019 priority list of hazardous compounds, arsenic is ranked as the highest-priority pollutant [103]. As(V) and As(III) are the two main forms of arsenic found in natural water, with the latter being more toxic and more difficult to remove than the former [29]. The concentration of arsenic in fresh waters typically ranges from 1–10 mg L⁻¹ to 100–5000 mg L⁻¹ in areas of sulfide mineralization and mining [27]. Approximately 60 million people drink groundwater contaminated with arsenic at above 10 µg L⁻¹ [28]. Among various methods for arsenic removal [33], the adsorption process is most common due to its simplicity, ease of operation, sludge-free operation, and regeneration capability [104][68].

A variety of adsorbents has been developed for arsenic removal [105]. Iron oxide-based adsorbents are particularly noted for their superior performance and their capability of forming stable complexes with arsenic. Iron oxides in various forms have been extensively developed and studied for arsenic adsorption [61]. Among them, amorphous iron oxides are most effective, with high adsorption capacities due to high specific surface area. However, amorphous iron oxide adsorbents are difficult for separation due to their small sizes and tend to form low-surface-area crystalline iron oxides during preparation. One way to overcome this challenge is to use iron oxide-based composite adsorbents by loading iron oxides on various substrates, such as activated carbon, graphene oxide (GO) and cellulose. In particular, our group has demonstrated the superior performance of amorphous iron

oxide-GO nanocomposite adsorbents with high adsorption capacities (147 and 113 mg g⁻¹ for As(III) and As(V), respectively) and high efficiency for arsenic removal [86].

Layered double hydroxides (LDHs), a class of 2-dimensional ionic lamellar compounds with the general formula of $[M(II)_{1-x}M(III)_x(OH)_2]_x+(An^-)_x/n \cdot mH_2O$, where M(II) represent bivalent metal cations, M(III) represents trivalent metal cations, and x is the molar ratio of M(III)/(M(II)+M(III)), have also received significant interest as adsorbents for wastewater treatment due to their stability, substantial surface area, porous structure, and functional groups. Arsenic is present as oxyanions in aqueous solutions. Hence, surface ions and functional groups with a positive charge are important in arsenic adsorption. LDHs can absorb anions due to their hydrophilicity with abundant hydroxyl groups and high capacity for anion exchange [106–109][78]. However, the multilayer packing and bulk particle sizes limit the adsorption capability of LDHs [78]. In this regard, loading LDHs on GO as a substrate is hypothesized to increase the surface area of the adsorbent for improved arsenic adsorption, following our earlier work on iron oxide-GO composite adsorbents [86].

Herein, we report the synthesis of a range of Mg–Fe LDH-GO nanocomposite adsorbents at various Mg/Fe ratios and GO contents and their performances toward arsenic adsorption. In our design of the LDHs, we hypothesize that the incorporation Mg(OH)₂ will lead to the enhanced surface charge, on the basis of the higher point-of-zero charge (PZC) of MgO compared to iron oxide [110], which is beneficial to the adsorption of arsenic oxyanions. A systematic investigation on the relationship between the composition of the adsorbents and their adsorption performances towards both As(III) and As(V) has been undertaken, with the optimum composites identified. Our results suggest their high potential for arsenic removal from both drinking water and industrial wastewater.

4.3 Experimental Section

4.3.1 Chemicals and Materials

Chemicals and materials, including natural graphite flake (325 mesh particle size: $\geq 99\%$, Aldrich), potassium permanganate (99.0+%, Aldrich), hydrogen peroxide (30%, Fisher Scientific), sulfuric acid (96.9 wt%, Fisher Scientific), phosphoric acid (85+%, Acros), ferric sulfate hydrate (97%, Fe 21.6%, Aldrich), magnesium nitrate hexahydrate (99+%, Aldrich), ammonium hydroxide solution (28–30%, Aldrich), hydrochloric acid (37%, Fisher Scientific), and ethanol (ACS reagent, Fisher Scientific) were used as received without any additional purification. Deionized water was obtained from a MilliporeSigma™ Milli-Q™ ultrapure water purification system. Sodium (meta) arsenite (NaAsO_2 , $\geq 90\%$, Aldrich) and sodium arsenate dibasic heptahydrate ($\text{Na}_2\text{HAsO}_4 \cdot 7\text{H}_2\text{O}$, $\geq 98\%$, Aldrich) were selected as the source of As(III) and As(V), respectively. Stock solutions of As(III) and As(V) containing 1000 mg L⁻¹ of arsenic were prepared in deionized water. Various concentrations of arsenic standard solutions were diluted from the stock solutions with the pH adjusted using HNO_3 or NaOH.

4.3.2 Synthesis of Graphene Oxide

Graphene oxide (GO) was synthesized from natural graphite flakes by using an improved Hummers method reported by Tour et al. [85]. A typical process involved the preparation of a mixture of concentrated $\text{H}_2\text{SO}_4/\text{H}_3\text{PO}_4$ (120 mL: 13 mL) acids in a round-bottom flask, followed by the addition of 1 g of graphite flakes into the acid mixture. The mixture was stirred vigorously for 10 min to obtain a dark-colored suspension. Subsequently, 6 g of KMnO_4 was added slowly to the suspension in an ice bath. The mixture was then stirred at 50 °C for 36 h, rendering a viscous reddish-brown slurry. After cooling to room temperature, the mixture was slowly poured into 134 mL of cold deionized water containing 2 mL of H_2O_2 (30%). Following that, the suspension was washed once with aqueous HCl solution (10%

w/w), and then multiple times with deionized water (DI) till the pH reached 6. Finally, the suspension was washed once with ethanol. The solid product (1.2 g total) was dried and collected for use.

4.3.3 Synthesis of nanocomposite adsorbents

In this study, 15 different adsorbents were synthesized, including nine Mg–Fe LDH-GO nanocomposites with iron and magnesium hydroxides immobilized on GO at different ratios and GO contents (termed as LDH_x-y-GO-z, with x standing for the molar ratio of Fe(III)/(Mg(II)+Fe(III)) in the LDH, and y and z standing for weight percentages of LDH and GO, respectively, in the nanocomposite), and six composites with either iron oxide or magnesium hydroxide immobilized on graphene oxide (termed as F_y-GO_z for a α -Fe₂O₃-GO composite with α -Fe₂O₃ at a weight percentage of y and GO at the balancing weight percentage of z, or M_y-GO_z for a Mg(OH)₂-GO composite with Mg(OH)₂ at a weight percentage of y and GO at the balancing percentage of z). The α -Fe₂O₃-GO and Mg(OH)₂-GO composite adsorbents are included for the purpose of comparison. All the composites were synthesized by the coprecipitation method.

Representatively, the following is a procedure for the synthesis of the α -Fe₂O₃-GO composite with 80 wt% of iron oxide (F80-GO20). A Fe₂(SO₄)₃ solution (0.3 g of Fe₂(SO₄)₃ in 10 mL of DI water) was slowly poured into a GO suspension (0.03 g in 20 mL of DI water) at room temperature. Subsequently, 6 mL of 30% ammonia solution was added dropwise under stirring to reach a pH of 10. The suspension was heated at 85 °C for 40 min under rapid stirring and was then cooled to room temperature, followed by filtration. The resulting solid was washed with DI water several times and then with ethanol and was finally dried at 60 °C overnight under vacuum, yielding 125 mg of F80-GO20. Two other α -Fe₂O₃-based nanocomposites containing different iron oxide contents (F20-GO80 and F50-GO50) were similarly prepared. Mg(OH)₂-based composites (for example, M80-GO20) were similarly synthesized but with the pH of 12 used in the coprecipitation.

In our design of the LDH-GO composite adsorbents, the total weight content of iron and magnesium hydroxides in the nanocomposites was controlled at about 20, 50, or 80 wt%, while at different molar fractions of Fe (x, i.e., the molar ratio of Fe(III)/(Fe(III)+Mg(II))). Representatively, the following is a procedure for the synthesis of LDH0.42-80-GO20 with the content of hydroxides at 80% and Fe molar fraction of 0.42. Ferric sulfate hydrate (0.1 g) and magnesium nitrate (0.176 g) were dissolved in 10 mL of DI water. The solution was slowly added to a dispersion of GO (0.02 g) in 10 mL of DI water at room temperature. Subsequently, 8 mL of 30% ammonia solution was added dropwise under stirring to this suspension to reach a pH of 12. The suspension was heated to 85 °C under rapid stirring for 40 min. After cooling to room temperature, the suspension was filtered, washed several times with water and then once with ethanol, and finally dried overnight under vacuum at 60 °C to yield LDH0.42-80-GO20 (98 mg). LDH-GO composites of LDH0.42-50-GO50 and LDH0.42-20-GO80 with the total Fe(OH)₃/Mg(OH)₂ contents of 50 and 20 wt%, respectively, were similarly synthesized. Figure 0-1 shows the schematic synthesis of three types of nanocomposite adsorbents.

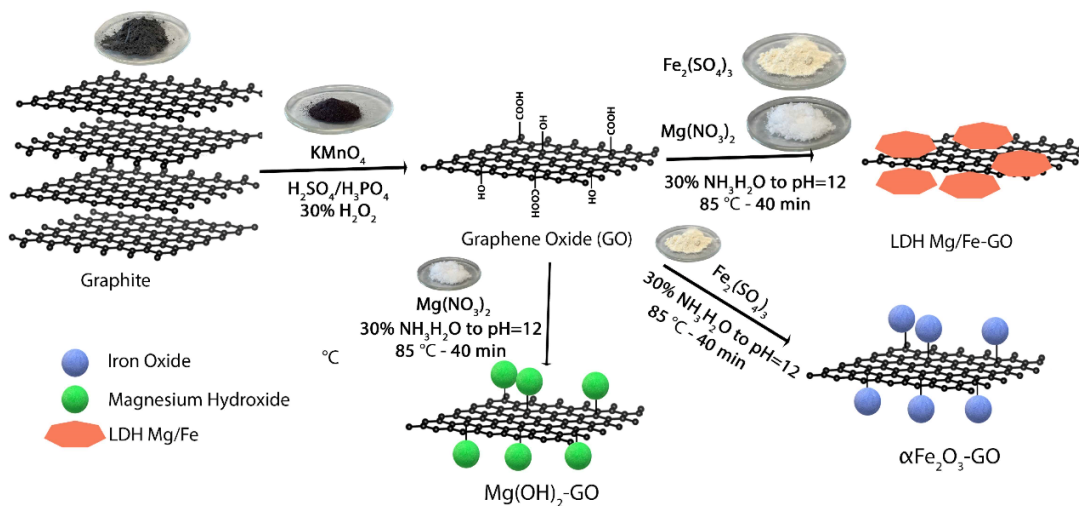


Figure 0-1: Schematic synthesis of LDH-GO, $\alpha\text{-Fe}_2\text{O}_3$ -GO, and $\text{Mg}(\text{OH})_2$ -GO nanocomposite adsorbents.

4.3.4 Characterization

Braunauer–Emmett–Teller (BET) specific surface area, pore volume, and pore size distribution of the nanocomposite samples were determined by N₂ sorption at 77 K on a Micromeritics 3Flex Surface and Catalyst Characterization analyzer. Before the sorption measurements, the samples were degassed under vacuum at 110 °C for 12 h. Wide-angle X-ray diffraction (XRD) patterns of the nanocomposites were recorded on an Rigaku Smartlab SE X-ray diffractometer with Cu K α radiation at room temperature. Fourier-transformed infrared (FTIR) spectra were obtained on a Thermo Scientific Nicolet 6700 Analytical FTIR spectrometer. The samples were prepared as pellets with the use of spectroscopic-grade KBr. Zeta potential measurements of dilute dispersions (0.1 mg mL⁻¹) of the nanocomposites were performed on an Anton Paar Litesizer 500 dynamic light scattering instrument at room temperature. The concentration of arsenic was quantified with an Agilent 7500ce inductively coupled plasma mass spectrometry (ICP-MS) within the concentration range of 0.01-10 mg L⁻¹. A solution of arsenic ICP standard (concentration of 1000 ppm; Catalog # EMD 170303 from Aldrich) was diluted with 5% HNO₃ to different extents, which were used for the calibration of the instruments. Raman spectra (excitation at 532 nm) were recorded on a Fergie spectrometer by Princeton instrument. Thermogravimetric analysis (TGA) of the nanocomposites was carried out on a Q50 TGA from TA instruments. Measurements were performed in the air atmosphere. In a typical measurement, the sample (10 mg) was heated to 100 °C at a rate of 10°C min⁻¹, held at 100 °C for 10 min, and then heated to 700 °C at a rate of 10 °C min⁻¹. TEM characterizations were performed on a Thermo Scientific Talos 200X transmission electron microscope operating at 200 kV.

4.3.5 Arsenic adsorption

All arsenic adsorption experiments were undertaken in a batch mode at room temperature, i.e., around 23 °C. To measure the sorption capacity of various adsorbents for removal of

As(III) and As(V), 3 mL of As solutions with different initial concentrations (0.1–1000 mg L⁻¹) were in contact with 1.5 mg of each adsorbent at a constant stirring rate of 300 rpm at pH of 6.8. After 24 h, the suspensions were filtered with a syringe filter and the equilibrium concentration of non-adsorbed arsenic concentration in the filtrate solutions were measured. The equilibrium sorption uptake was calculated by using the mass balance equation [111]:

$$q_e = \frac{C_0 - C_e}{m} V \quad (1)$$

where q_e (mg g⁻¹) is the equilibrium adsorption uptake, C_0 (mg L⁻¹) and C_e (mg L⁻¹) are the initial and equilibrium arsenic concentration, V (L) is the solution volume and m (g) is the mass of the adsorbent.

The adsorption isotherms of the various composite adsorbents were fitted with the Langmuir model

$$q_e = \frac{abC_e}{(1+bC_e)} \quad (2)$$

where a is the saturated/maximum adsorbed capacity (mg g⁻¹) and b is the Langmuir constant that directly relates to the adsorption affinity (L mg⁻¹).

Adsorption kinetic curves were obtained with an LDH-GO composite adsorbent having a total metal hydroxides content of 80 wt%, LDH0.42-80-GO20. In the experiment, 1.5 mg of the composite was dispersed in a range of As(III) and As(V) standard solutions of the same volume (3 mL) and concentration [568 and 645 mg L⁻¹ for As(III) and As(V), respectively]. After stirring for a prescribed period of time (from 10 min to 24 h), each dispersion was rapidly filtered and the equilibrium arsenic concentration in the filtrate was measured to determine the time-dependent adsorption capacity. A pseudo-second-order kinetic model

was used to fit the adsorption kinetics (Eq. 3 and 4), rendering the initial adsorption rate (Eq. 5) [28].

$$\frac{dq_t}{dt} = k_2(q_e - q_t)^2 \quad (3)$$

$$\frac{t}{q_t} = \frac{1}{(k_2q_e^2) + \frac{t}{q_t}} \quad (4)$$

$$V_0 = k_2q_e^2 \quad (5)$$

Where q_t is the amount (mg g^{-1}) of arsenic adsorbed on the adsorbent at various time t , k_2 is the rate constant ($\text{g mg}^{-1} \text{min}^{-1}$), q_e is the equilibrium adsorption capacity (mg g^{-1}), and V_0 is the initial adsorption rate ($\text{mg g}^{-1} \text{min}^{-1}$).

Moreover, the effects of several interfering ions including CO_3^{2-} , SO_4^{2-} , and NO_3^- (100 mg L^{-1}) on the batch adsorption of As(III) and As(V) with LDH0.42-80-GO20 have also been evaluated. Each adsorption was performed at the adsorbent loading of 1.5 mg in 3 mL (i.e., 0.5 mg mL^{-1}) and initial arsenic concentration of around $250 \mu\text{g L}^{-1}$ at the pH of 6.8. The concentration of the co-existing anions was set excessively at around 1000 times that of arsenic (i.e., 100 mg L^{-1} for K_2CO_3 , Na_2SO_4 , and NaNO_3). Each adsorption underwent for 24 h under stirring at room temperature. Afterwards, the suspension was filtered, and the filtrate was analyzed with ICP-MS for equilibrium arsenic concentration and the subsequent calculation of the equilibrium adsorption capacity.

4.4 Result and discussion

4.4.1 Synthesis and Characterizations of Nanocomposite Adsorbents

A range of LDH-GO nanocomposite adsorbents with different Fe/(Fe+Mg) molar ratios ($x = 0.26, 0.42, \text{ or } 0.6$) and LDH mass contents (20, 50 and 80 wt%, respectively) have been synthesized herein to investigate the effects of the composition on their adsorption

performance. In parallel, α -Fe₂O₃-GO and Mg(OH)₂-GO nanocomposites at α -Fe₂O₃ or Mg(OH)₂ mass content of 20, 50, and 80 wt%, respectively, have also been synthesized and compared for their performances with those of LDH-GO nanocomposite adsorbents. In the composites, GO is used as the substrate for the loading of metal hydroxide/oxide nanostructures. All the composites have been synthesized through the co-precipitation method and have been systematically characterized.

Figure 0-2(a) shows the XRD patterns of representative LDH-GO composites, as well as those of GO, and representative F-GO and M-GO samples. The pattern of GO displays an intense peak of (002) reflection with an interlayer spacing of 0.86 nm, which corresponds to the interlayer spacing between stacked GO sheets and is much larger than that of pristine graphite (0.34 nm). It demonstrates the oxidation of graphite to GO due to the introduction of oxygen containing functional groups on the graphene sheets. This peak is absent in all the composites, suggesting the complete exfoliation of GO sheets following the loading of the hydroxides/iron oxide. In addition, a very weak and broad peak at about 43° is also seen in the pattern of GO, which is attributed to the (100) peak of graphitic structures [85][86].

Despite significant content of α -Fe₂O₃, the binary composite F80-GO20 shows weak (012), (104), (101), (113), (024), (116), (214) and (300) diffraction peaks characteristic of α -Fe₂O₃ (JCPDS Card #80-2377). In the patterns of other iron oxide-containing composites, these peaks are even weaker due to the lower α -Fe₂O₃ contents. In the binary Mg(OH)₂-GO composites, diffraction peaks attributed to (001), (101), (102), (110), (111), (103) and (201) planes of the hexagonal Mg(OH)₂ phase (JCPDS no. 44-1482) [112][57]. can be clearly seen. All the LDH composites with LDH content of 80 wt% show (003), (006), (012), (015), (018), (110), and (113) diffraction peaks characteristic of Mg-Fe LDHs despite their different Fe/Mg molar ratios [109][113]. This confirms the presence of LDH structures. Moreover, the interlayer distance of the LDHs is estimated to be approximately 0.8 nm based on the

position of (d003) peak. These characteristic LDH peaks are very weak in the LDH-GO composites with lower LDH contents of 50 and 20 wt%.

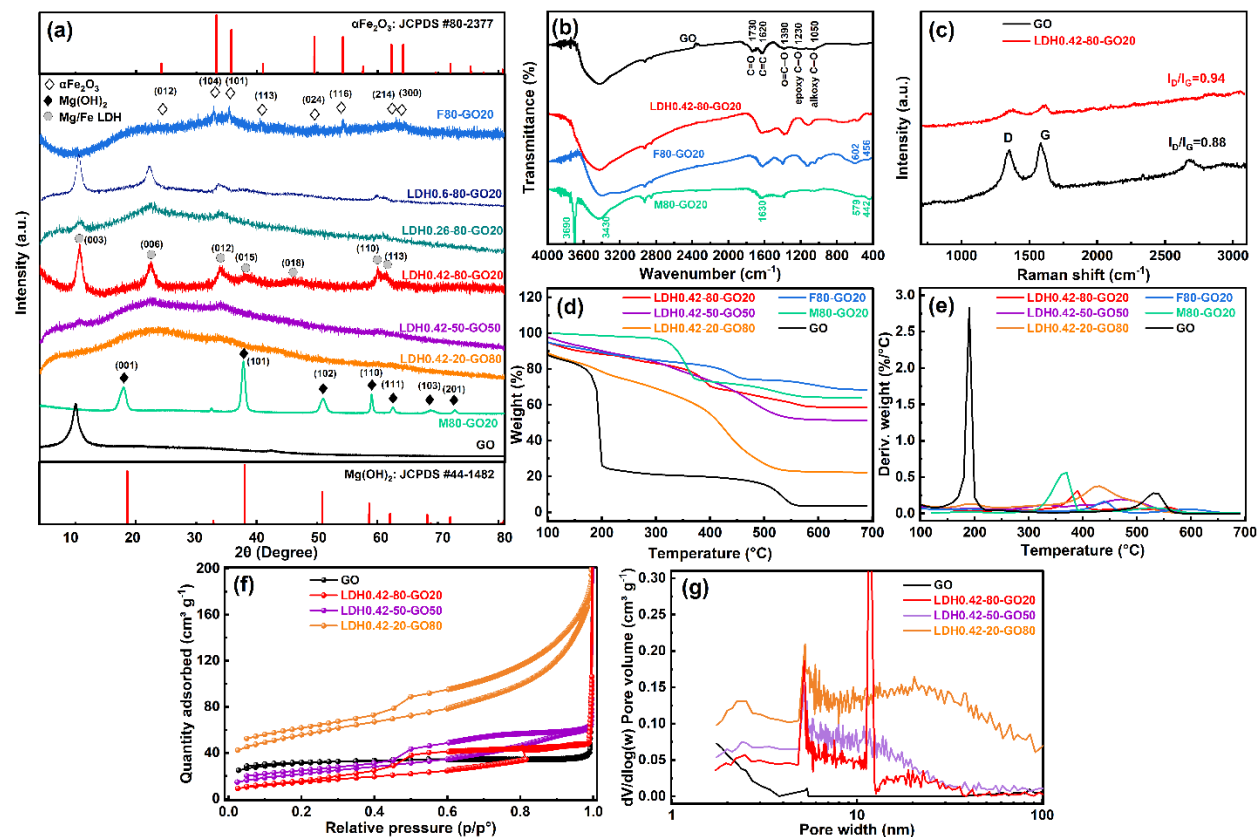


Figure 0-2: (a) Wide-angle XRD patterns, (b) FTIR spectra, (c) Raman spectra, (d) TGA curves and (e) differential curves, (f) N₂ sorption isotherms, and (g) NLDTF meso-/macro-pore size distribution curves of GO and representative LDH-GO, α -Fe₂O₃-GO and Mg(OH)₂-GO composites.

Figure 0-2(b) shows the FTIR spectra of representative LDH-GO composites, as well as those of binary composite (F80-GO20 and M80-G20) and GO as the control samples. In the spectrum of GO, characteristic stretching vibrations of C=O (1730 cm⁻¹), aromatic C=C (1620 cm⁻¹), carboxyl O=C-O (1390 cm⁻¹), epoxy C-O (1230 cm⁻¹), alkoxy C-O (1050 cm⁻¹), and -OH (3100–3500 cm⁻¹) are observed. The spectra of all the composites show broad bands within 400-1800 cm⁻¹. The distinct aromatic C=C stretching in GO at 1620 cm⁻¹ is seen with the

composites. Meanwhile, some weak bands are observed within the low frequency range of 400-800 cm^{-1} in the spectra of the composites, attributable to stretching of metal-oxygen-metal bonds in LDH, $\alpha\text{-Fe}_2\text{O}_3$, or $\text{Mg}(\text{OH})_2$ in the composites [86][88]. The broad band at around 3430 cm^{-1} is also seen in all the composites, attributable to -OH groups or adsorbed water molecules in the composites.

Figure 0-2(c) shows the Raman spectra of GO and LDH0.42-80-GO20 as a representative LDH-GO composite. Both spectra are dominated by two strong peaks at 1353 cm^{-1} and 1584 cm^{-1} corresponding to the D and G bands, respectively, of GO. In the spectrum of GO, a 2D band at about 2700 cm^{-1} is also observed. Compared to that of GO (0.88), a slightly higher ID/IG ratio of 0.94 is found with LDH0.42-80-GO20, indicating the slight reduction GO during the synthesis of the composite [86].

Figure 0-2(d) shows the TGA curves of representative composites and GO, as well as their differential curves. GO shows the typical two-step weight loss. The first step (loss of ca. 70%) occurs within 150–205 °C with the peak weight loss at 190 °C, which is attributed to the evaporation of adsorbed water and the decomposition of thermally labile oxygen-containing functional groups [85][88]. The second step of weight loss takes place within 470–570 °C (peak loss at 530 °C) with negligible char yield at 600 °C, which is ascribed to the decomposition of more stable oxygen functionalities and the combustion of GO framework. F80-GO20 shows the gradual weight loss within 100-460 °C with a total weight loss of around 20% at 600 °C, which corresponds to the complete loss of GO in consistency with the designed composition. M80-GO20 shows the predominant one-step weight loss weight within 300–375 °C with the final loss of around 30% at 600 °C, attributable to the loss of GO and the partial decomposition of $\text{Mg}(\text{OH})_2$ by dehydration. Three LDH-GO composites show the gradual weight loss from 100 to about 550 °C, along with a distinct step loss at different temperature ranges depending on the composite. The peak temperature of the step weight

loss of the LDH-GO composites shows a trend of increase from about 390 °C for LDH0.42-80-GO20 to 425 °C for LDH0.42-20-GO80, along with the increase of percentage weight loss. This indicates the step weight loss arises from GO. As expected, the char yield of the LDH-GO composites at 600 °C decreases from around 73% for LDH0.42-80-GO20 to about 35% for LDH0.42-20-GO80 with the increase of GO content in the composites.

The textural properties of representative composites and GO have been characterized with N₂ sorption analysis at 77 K. Figure 0-2(f) shows the N₂ sorption curves of the representative LDH-GO composites and GO. Figure 0-2(g) shows their NLDFT meso-/macro-pore size distribution curves. Table 0-1 summarizes the characterization results, including surface area, pore volume, and average pore size. A type IV sorption isotherm is observed with all synthesized composites, with a steep adsorption in the low relative pressure range (0-0.1) and a hysteresis loop in the medium to high relative pressure range (0.4-0.9). The composites are primarily featured with mesopores with negligible/minor micropores. The BET surface area and pore volume of GO are 100 m² g⁻¹ and 0.24 cm³ g⁻¹, respectively, with pores of average size of 98 Å arising from the packing of the GO sheets. α-Fe₂O₃-GO composites show increasing surface area (from 70 to 227 m² g⁻¹) and pore volume (from 0.12 to 0.21 cm³ g⁻¹) with the increase of iron oxide content from 20 to 80 wt%, along with the decreasing average pore size (from 70 to 41 Å). These results from the loading of small-sized α-Fe₂O₃ nanoparticles. With the increase of Mg(OH)₂ content from 20 to 80 wt%, Mg(OH)₂-GO composites also show increasing surface area (from 72 to 101 m² g⁻¹) and pore volume (from 0.27 to 0.59 cm³ g⁻¹), but with much bigger average pore sizes that also increase from 147 to 233 Å. These suggest that Mg(OH)₂ particles loaded on GO have much bigger sizes than α-Fe₂O₃ particles in the α-Fe₂O₃-GO composites. Figure A3 shows the N₂ sorption results for other synthesized composites.

With the LDH-GO composites at a given Fe/(Mg+Fe) molar ratio (i.e., x), a similar general trend of increasing surface area and pore volume is noticed with the increase of LDH content. For example, at x of 0.42, the surface area and pore volume increase from 54 m² g⁻¹ and 0.09 cm³ g⁻¹, respectively, for LDH0.42-20-GO80 to 78 m² g⁻¹ and 0.1 cm³ g⁻¹ for LDH0.42-50-GO50, and to 101 m² g⁻¹ and 0.59 cm³ g⁻¹ for LDH0.42-80-GO20. This is also accompanied with the decrease in average pore size from 68 to 51 and to 57 Å. Clearly, the loading of LDH nanoparticles at an increasing amount generates more interparticle pores and thus surface area. Meanwhile, comparing each set of LDH-GO composites at a given LDH content, one can see that those with x of 0.60 have lowest surface area and pore volume within the set, along with the highest average pore size. For example, in the set LDHx-80-GO20, LDH0.60-80-GO20 shows the lowest surface area of 27 m² g⁻¹ and lowest pore volume of 0.06 cm³ g⁻¹, along with the highest average pore size of 85 Å. This suggests that the LDH with x of 0.6 shows the largest particle size. Among all the LDH-GO composites, LDH0.42-80-GO20 has the highest surface area and pore volume of 189 m² g⁻¹ and 0.27 cm³ g⁻¹, respectively.

Table 0-1: BET surface area, pore volume, and average pore size of representative composites and GO.

Sample	Surface Area (m ² g ⁻¹)			Pore Volume (cm ³ g ⁻¹)			Average pore size (Å)
	S _{BET}	S _{d<2 nm}	S _{d>2 nm}	V _{Total}	V _{d<2 nm}	V _{d>2 nm}	
GO	100	51	48	0.24	0.03	0.21	98
F80-GO20	227	39	88	0.23	0.02	0.21	41
F50-GO50	167	18	149	0.19	~0	0.19	45
F20-GO80	70	8	62	0.12	~0	0.12	70
M80-GO20	101	5	96	0.59	~0	0.59	233
M50-GO50	82	~0	82	0.44	~0	0.44	213

M20-GO80	72	~0	72	0.27	~0	0.27	147
LDH0.60-80-GO20	27	~0	27	0.06	~0	0.06	85
LDH0.42-80-GO20	189	45	144	0.27	0.02	0.25	57
LDH0.26-80-GO20	145	3	142	0.12	~0	0.12	32
LDH0.60-50-GO50	50	~0	50	0.22	~0	0.22	179
LDH0.42-50-GO50	78	1	77	0.1	~0	~0.1	51
LDH0.26-50-GO50	105	4	101	0.2	~0	0.2	77
LDH0.60-20-GO80	25	~0	25	0.14	~0	0.14	408
LDH0.42-20-GO80	54	~0	61	0.09	~0	~0.09	68
LDH0.26-20-GO80	60	~0	60	0.27	~0	0.27	182

Figure 0-3 shows the TEM images of GO, LDH0.42-80-GO20 as a representative LDH-GO composite, and corresponding Fe₂O₃-GO and Mg(OH)₂-GO composites (F80-GO20 and M80-GO20), as well as elemental mapping images of the LDH-GO composite. GO shows transparent wrinkled sheets (a, b). In all the composites, GO sheets are decorated with the nanoparticles of hydroxides or oxide. From the images of LDH0.42-80-GO20 composite (Figure 0-3g,h), LDH particles are uniformly distributed within the composite. The elemental mapping images confirm the uniform distributions of C, O, Fe, and Mg elements within the investigated domain.

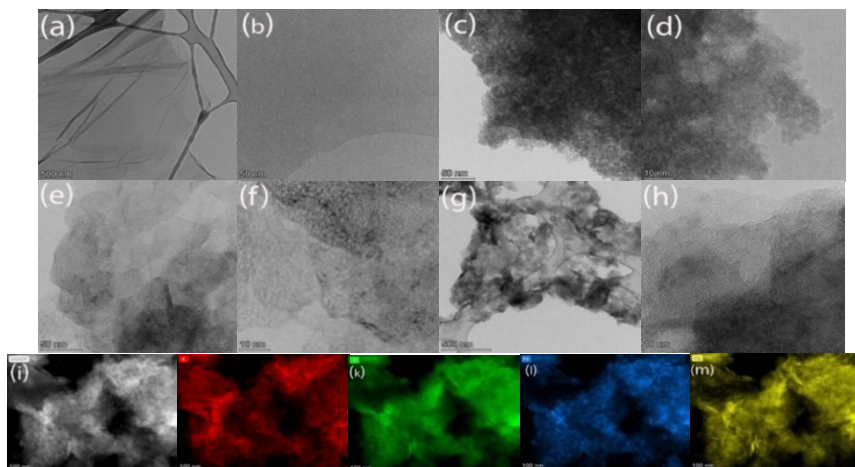


Figure 0-3: Transmission electron microscopy of GO (a, b), F80-GO20 (c, d), M80-GO20 (e, f), and the LDH-GO composite LDH0.42-80-GO20 (g, h). Dark field scanning transmission electron microscopy (DF-STEM) image (i) and the corresponding C (j), O (k), Fe (l) and Mg (m) elemental maps of LDH0.42-80-GO20.

4.4.2 Arsenic adsorption

To screen out the optimum composites and study the structure-performance relationships, we have systematically evaluated the performance of the LDH-GO composite adsorbents for batch adsorption of As(III) and As(V), along with those of GO and Fe₂O₃-GO and Mg(OH)₂-GO composites for comparison. Figure 0-4 compares the equilibrium adsorption capacities (q_e) of the various adsorbents toward As(V) at the identical initial arsenic concentration of 132 mg L⁻¹, adsorbent loading of 1 mg mL⁻¹, and pH of 6.8. Meanwhile, composite adsorbents at hydroxide/oxide content of 80 wt% are also compared for their adsorption capacities toward As(III) at otherwise identical conditions. Table A3 in Supporting Information summarizes the adsorption capacity results, along with the BET surface area and zeta potential of the composites. Among them, GO shows the lowest adsorption capacities (4.3 and 12.2 mg g⁻¹, respectively) for both As(III) and As(V). With α -Fe₂O₃-GO adsorbents, one can see that the As(V) adsorption capacities increase with the increase of α -Fe₂O₃ content in the composites, for example, 52.7 mg g⁻¹ with F80-GO20 and 17.2 mg g⁻¹ with F20-GO80 towards As(V), which is in agreement with our earlier report [86].

This is ascribed to the increasing surface area (from 70.5 to 227 m² g⁻¹) with the increase of iron oxide content. Meanwhile, the increasing zeta potential (from -30 to -2.3 mV) with the increase of iron oxide content may also contribute to that as As(V) is present in a negative ionic form (H₂AsO₄⁻ at pH = 2.2–6.5, HAsO₄²⁻ at pH = 6.5–11.5) [86].

The As(V) adsorption capacity of Mg(OH)₂-GO adsorbents only shows marginal changes (21.2–15.2 mg g⁻¹) with the increase of Mg(OH)₂ content from M20-GO80 to M80-GO20 given their similar surface areas (72.8–88.8 m² g⁻¹).

For each set of LDH-GO composites at a given x, the increase of the LDH content generally leads to the increased adsorption capacities for As(V) due to the increases in surface area and zeta potential. For example, in the set with x of 0.42, the As(V) adsorption capacity increases from 21.5 mg g⁻¹ for LDH0.42-20-GO80 (surface area, 54.3 m² g⁻¹; zeta potential, -16.6 mV) to 56.1 mg g⁻¹ for LDH0.42-80-GO20 (189.4 m² g⁻¹; 2.1 mV). Meanwhile, the set of LDH-GO composites of the LDH content of 20 wt% shows similar adsorption capacities though with three different x values. However, in each set at the higher LDH contents of 50 and 80 wt%, the LDH-GO composite at the x value of 0.42 (i.e., LDH0.42-50-GO50 and LDH0.42-80-GO20, respectively) has the highest As(V) adsorption capacities, indicating that the LDH composition is optimum for the adsorption. Among all the adsorbents, LDH0.42-80-GO20 shows the highest adsorption capacity (56.1 mg g⁻¹) towards As(V) at the applied adsorption condition with its high surface area and highest zeta potential, followed by F80-GO20 (52.7 mg g⁻¹). With respect to the adsorption of As(III), only the composites with the highest hydroxides/oxide content of 80 wt% were investigated. Among them, F80-GO20 instead shows the highest As(III) adsorption capacity of 89.5 mg g⁻¹, followed by LDH0.42-80-GO20 (63.4 mg g⁻¹). Clearly, surface area is the dominant factor affecting the adsorption of As(III) as As(III) is present in a neutral form (H₃AsO₃) at pH below 9.2 [86]. With its best adsorption capacity among the LDH-GO composites based on the above screening

experiments, the subsequent investigation on arsenic adsorption has thus been focused exclusively on LDH0.42-80-GO20.

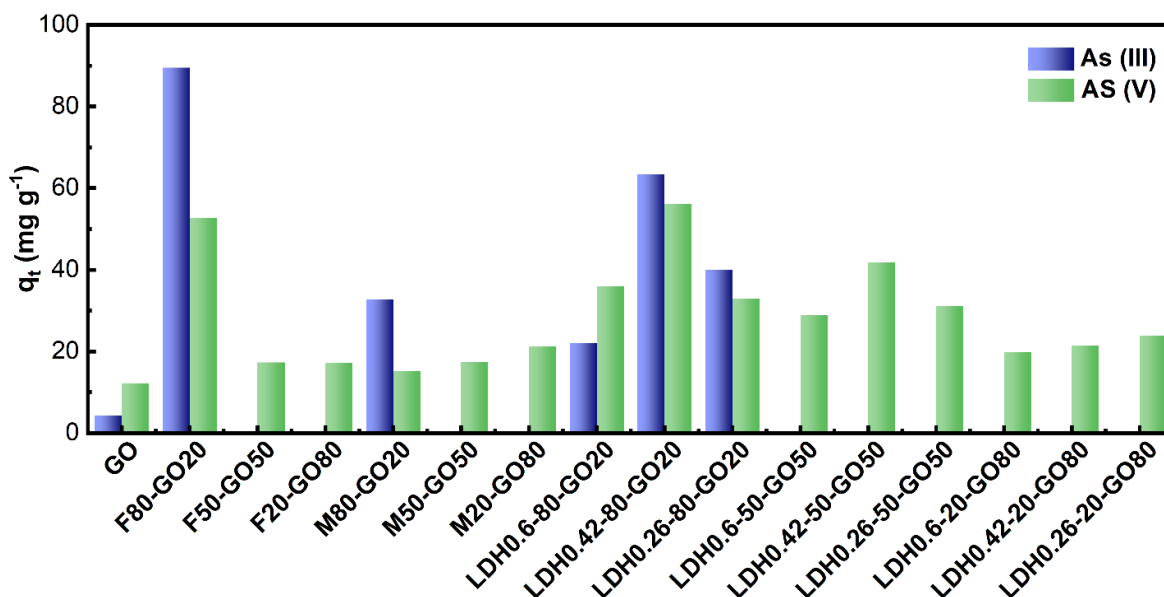


Figure 0-4: Adsorption capacity for composites for As(III) and As(V) removal at adsorbent dosage of 1 mg mL^{-1} and pH of 6.8.

With LDH0.42-80-GO20, we have subsequently examined the effect of adsorbent dosage ($0.5\text{--}2 \text{ mg mL}^{-1}$) on the adsorption of As(V) at an initial concentration of 248 mg L^{-1} . Figure 0-5a shows the dependences of equilibrium adsorption capacity (q_e) and percent removal of As(V) on the adsorbent dosage. With the increase of the adsorbent dosage from 0.5 to 2 mg mL^{-1} , a drop in q_e from 292 to 94 mg g^{-1} is seen, while the percentage removal only shows a minor increase from 59 to 75% . In consequence, the adsorbent dosage of 0.5 mg mL^{-1} has been chosen for all the following experiments.

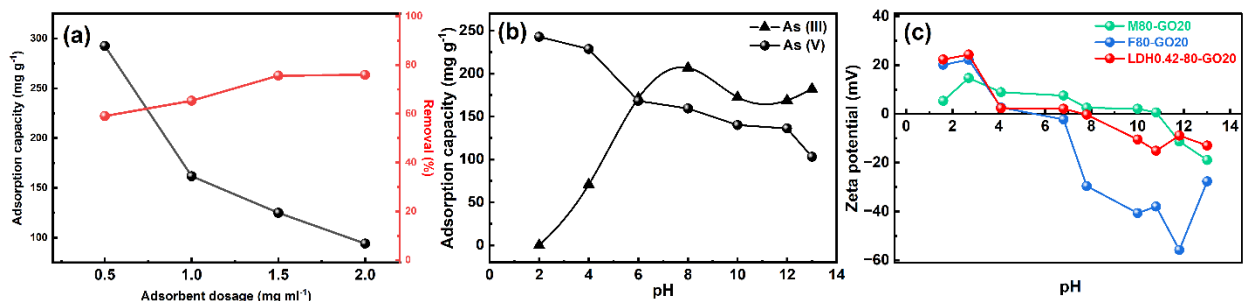


Figure 0-5: (a) Effects of the dosage of LDH0.42-80-GO20 on equilibrium adsorption capacity and percent removal of As(V) at the initial concentration of 248 mg L⁻¹; (b) effects of pH on adsorption capacity of LDH0.42-80-GO20 towards As(III) and As(V) at the initial arsenic concentration of 141 mg L⁻¹ and adsorbent dosage of 0.5 mg mL⁻¹; (c) effects of pH on zeta potential of LDH0.42-80-GO20, F80-GO20, and M80-GO20.

It has been proven that pH is a key parameter in adsorption processes as it affects the adsorbent surface charge and chemistry of the metals in solution [114][47]. Figure 4(b) shows the effects of pH (within 2-14) on q_e of LDH0.42-80-GO20 for both As(III) and As(V). In the case for As(III), the increase of pH from 2 to 8 leads to a drastic increase in q_e from nearly zero to 207 mg g⁻¹, which stays nearly at a plateau (around 180 mg g⁻¹) with the further increase of pH from 8 to 14. A similar trend has been seen with α -Fe₂O₃-GO adsorbents in our earlier study [86]. In the case of As(V) at the initial concentration of 141 mg g⁻¹, the increase of pH from 2 to 13 leads to a gradual decrease of q_e from 243 to 103 mg g⁻¹. Similar trends of change have been observed with iron oxide-based adsorbents and are explained by changes in surface charge and arsenic speciation [38][67]. LDH are formed by the intercalation of anions within hydrated interlayer regions, which balance the positive charges in brucite-like sheets [77]. Figure 0-5c shows the effects of pH on the zeta potential of three composites, LDH0.42-80-GO20, F80-GO20, and M80-GO20. The increase of pH leads to the decrease of the zeta potential for all three composites. The point of zero charge (PZC) of the three composites increases in the order from 5.7 for F80-GO20 to 7.7 for LDH0.42-80-GO20 and to 10.9 for M80-GO20 [88][93]. When pH < pHPZC, the electrostatic interactions between the negatively charged As(V) species and the positively charged composite surface

cause the strong adsorption of As(V) species. With $\text{pH} > \text{pHPZC}$, the composite surface is negatively charged, resisting the adsorption of negatively charged As(V) species. Hence, increasing pH leads to the decrease in q_e for As(V). The higher PZC of LDH0.42-80-GO20 and in consequence the higher surface charge within the pH range contribute to its higher adsorption capacity towards As(V) relative to F80-GO20. M80-GO20 has the highest PZC among the three, with a zeta potential value greater than those of LDH0.42-80-GO20 and F80-GO20 within pH of 4-11. However, its significantly lower surface area compromises the As(V) adsorption capacity, despite the high surface charge values [93].

Figure 4-6(a) shows As(III) and As(V) adsorption isotherms obtained with LDH0.42-80-GO20 at pH of 6.8 with initial concentrations within 2–1150 mg L^{-1} for As(III) and 2.5–1290 mg L^{-1} for As(V). The isotherms have been fitted with different models, including Langmuir, Freundlich, and Temkin models (see Table A4 in Supporting Information). Figures A4 and A5 show the fitting curves and Table A5 summarizes fitting constants and resulting parameters with the different models for As(III) and As(V) respectively.

It can be observed that both As(III) and As(V) adsorption data exhibit a better fit to the Freundlich model, as evidenced by high correlation coefficients. The Freundlich isotherms suggest multi-layer coverage over a heterogeneous surface with identical sites for adsorption of arsenic on the surface of adsorbent. However, the Langmuir model also provides a satisfactory fit, with maximum adsorption capacities of 186 mg g^{-1} for As(III) and 307 mg g^{-1} for As(V). The data and Freundlich model fitting are shown in Figure 4-6(b) and c for As(III) and As(V), respectively.

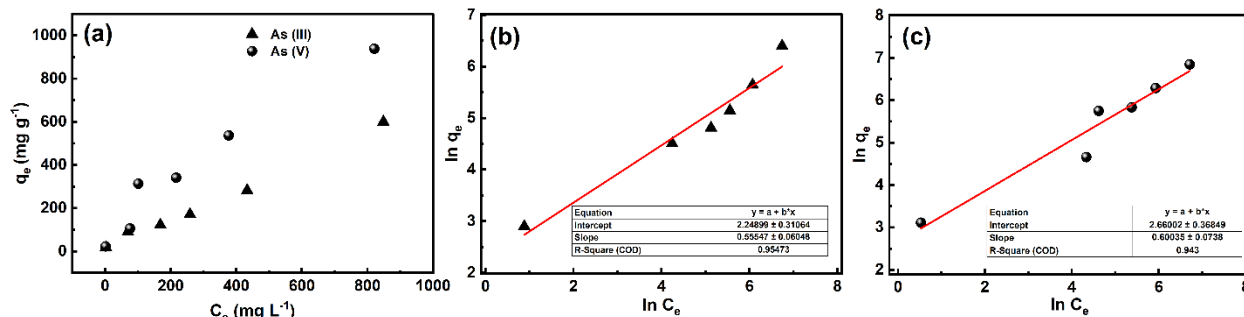


Figure 4-6: (a) Adsorption isotherms of LDH0.42-80-GO20 for both As(III) and As(V) at pH 6.8, and fitting with Freundlich model for (b) As(III) and (c) As(V).

The maximum arsenic adsorption capacities obtained herein with LDH0.42-80-GO20 through the Langmuir model are comparable to those reported in the literature for various best-performing adsorbents. Table 0-2 compares the maximum arsenic adsorption capacities achieved in the literature with various iron oxide-GO/RGO and LDH composite adsorbents, along with their surface area and adsorption conditions. One can find that LDH0.42-80-GO20 has higher maximum adsorption capacities compared to other LDH and iron oxide-based adsorbents. Clearly, loading LDH on GO is beneficial to render more active sites for arsenic adsorption. Meanwhile, compared to iron oxide-based adsorbents, the Mg-Fe LDH-based adsorbents have the added advantage of raised PZC and enhanced surface charge due to the incorporation of magnesium hydroxide, which is beneficial to the adsorption of As(V) often present in the anionic forms.

Table 0-2: BET Comparison of maximum arsenic adsorption capacities reported for various nanocomposite adsorbents.

Adsorbents	BET surface area (m ² g ⁻¹)	Conditions		Maximum adsorption Capacity (mg g ⁻¹)		Ref.
		pH	Dosage (mg mL ⁻¹)	As (III)	As(V)	
LDH0.42-80-GO20	189	6.8	0.5	186	307	This work

FeO _x -GO-80	341	7	0.8	147	113	[86]
α-Fe ₂ O ₃	162	neutral	60	95	47	[61]
Fe-Zr binary oxide	339	7	200	120	46.1	[72]
Manganese oxide-coated-alumina	194	7	5	42.48	N.A	[76]
TiO ₂ -Fe ₂ O ₃ bi-composite	133.5	5	1	N.A	12.4	[53]
γ-Fe ₂ O ₃ @ carbon	858	7	1	17.9	29.4	[31]
Hydrous TiO ₂	312	7	0.5	83		[92]
Hydrous TiO ₂	280	4	0.5		33	[92]
Fe ₃ O ₄	179		100	46	16.56	[67]
Fe-treated sample	20.9	5.5	3-18		10	[93]
Zn-MOF-74	604	6	1	211	325	[81]
Meso-Al-400	396	7	0.5	115	120	[31]
Magnetite reduced graphene oxide (M_RGO)	148	7	0.2	13	5	[28]
Fe/Mn-C Layered Double Hydroxide Composite	170	2	1.4	46	37	[78]
Mg-Fe layered double hydroxide nanoplates	144	7	0.5	N.A	271	[77]
Mg-Fe-S ₂ O ₈ LDH	10	4	0.5	75	75	[113]

In adsorption processes, kinetics is also of primary importance, especially in large-scale applications, where it is vital for establishing economically efficient systems. Figure 0-7 shows the adsorption curves with LDH0.42-80-GO20 for both As(III) and As(V) at initial arsenic concentration of 568 and 645 mg L⁻¹, respectively. A two-stage adsorption is seen for both As(III) and As(V), with a rapid uptake within the first 10 min of contact followed by a slow uptake to reach an equilibrium. In particular, the majority of the arsenic uptake, 81% and 82% for As(III) and As(V), respectively, occurs within the first 10 min, indicating the very fast adsorption rate. Subsequently, the process proceeds at a lower rate, which is due to the increment of adsorbed arsenic species on the surface of adsorbent and whereby fewer available sites for further adsorption. The curves have been found to be well fit with the

pseudo-second-order kinetic model (see Figure 0-7(b) and (c)) at high correlation coefficients of 0.999 and 0.989 for As(III) and As(V). The pseudo-second-order model is widely used to describe metal ion adsorption at solid-liquid interfaces [114][77]. Other kinetic models have also been used to fit the results (see Figure A6 and Figure A7 in Supporting Information), but with significantly lower correlation coefficients. The kinetic models and parameters of kinetic models are listed in Table A6 and Table A7 respectively.

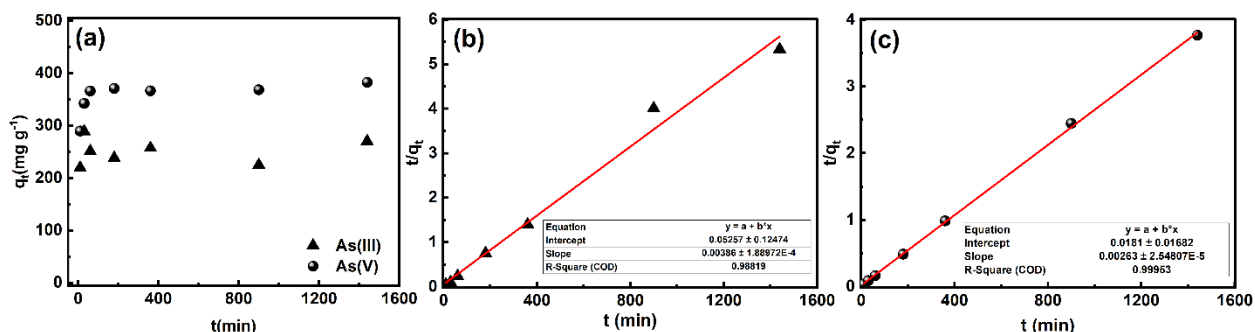


Figure 0-7: (a) kinetic data for adsorption of As(III) and As(V) with LDH0.42-80-GO20 at initial arsenic concentration of 568 and 645 mg L⁻¹, respectively; (b) fitting of the kinetic curves with the pseudo-second-order model.

The effects of coexisting anions (CO₃²⁻, SO₄²⁻, and NO₃⁻) on the batch adsorption of As(III) and As(V) with LDH0.42-80-GO20 have been investigated at the initial arsenic concentration of around 250 µg L⁻¹ at the pH of 6.8 and the excessive concentration of the co-existing anions at 100 mg L⁻¹. Figure 0-8 compares the residual arsenic concentrations after the adsorption. Despite their extremely high concentrations, the co-existing anions do not have significant effects on the arsenic adsorption. In each case except the adsorption of As(III) in the presence of co-existing CO₃²⁻, arsenic concentration has been successfully reduced with LDH0.42-80-GO20 to well below 10 µg L⁻¹, thus meeting the World Health Organization guidelines for drinking water. Only in the case of adsorption of As(III) in the presence of CO₃²⁻, a minor hindering effect by the co-existing anion is noticed, with the residual As(III) concentration at 23.7 µg L⁻¹. A higher adsorbent dosage is thus needed in this case in order to bring As(III)

concentration down to the required level. Table A8 provides initial and final concentration of As(III) and As(V) in presence of coexistence and without coexisting anions.

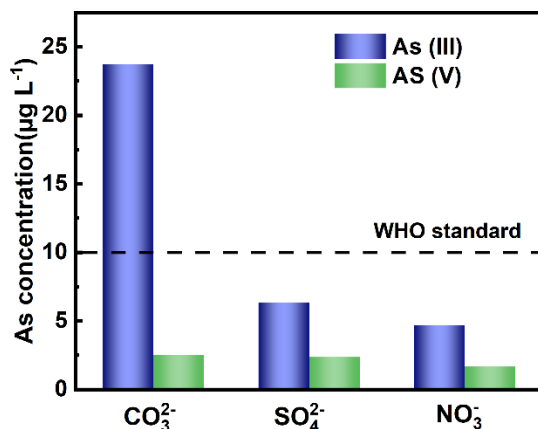


Figure 0-8: Residual arsenic concentration in the water containing different co-existing ions following adsorption with LDH0.42-80 -GO20 at the initial arsenic concentration of around 250 µg L⁻¹ at pH of 6.8 and co-existing anion concentration at 100 mg L⁻¹.

4.5 Conclusion

In this work, we have synthesized a range of Mg–Fe LDH-GO nanocomposite adsorbents with LDH particles loaded on 2-dimensional GO nanosheets at various designed Fe/(Fe+Mg) molar ratios ($x = 0.26, 0.42, \text{ and } 0.6$) and LDH mass contents (20, 50, and 80 wt%), along with $\alpha\text{-Fe}_2\text{O}_3\text{-GO}$ and $\text{Mg}(\text{OH})_2\text{-GO}$ counter adsorbents for the purpose of comparison. A systematic study on their structures and performances towards arsenic adsorption has been undertaken, with the aim of elucidating their structure-performance relationships. From the nitrogen sorption study, LDH-GO composites with x of 0.26 have the optimum textural properties, with highest surface area and pore volume at a given LDH content. For LDH-GO composites with a given x , increasing the LDH content improves the surface area and pore volume, which are important parameters affecting arsenic adsorption capacities. Meanwhile, the incorporation of Mg-based hydroxide into the LDH enhances the zeta potential of the composites relative to $\alpha\text{-Fe}_2\text{O}_3\text{-GO}$ composites, due to the known high point of zero charge

for MgO. This is beneficial to the adsorption of As(V), which is often present in the anion forms. By screening all the composites, we have found that LDH0.42-80-GO20 with the optimum x of 0.42 and LDH content of 80 wt% shows notably the highest As(V) adsorption capacity and second highest As(III) adsorption capacity (only second to F80-GO20) due to its high surface area and high zeta potential. A thorough investigation on the effects of adsorbent dosage and pH on the adsorption with LDH0.42-80-GO20 has been carried out, along with the establishment of the adsorption isotherms and kinetics. Moreover, LDH0.42-80-GO20 has also been demonstrated to effectively reduce arsenic concentration to well below $10 \mu\text{g L}^{-1}$ from $250 \mu\text{g L}^{-1}$ despite the presence of excessive coexisting anions (such as SO_4^{2-} , and NO_3^-). This work thus offers some important guidelines towards the rational design of high-performance adsorbents towards arsenic removal.

Chapter 5 Conclusion

The objectives of this work were to design and develop new adsorbents with enhanced performance for applications in industrial gold mill processes. Specifically, two sub-projects were defined to address the challenges in gold capture and arsenic removal.

5.1 Project on lignin-PE composite adsorbents for gold capturing

The study utilized various characterization techniques, including thermogravimetric analysis (TGA), Fourier-transform infrared spectroscopy (FTIR), X-ray diffraction (XRD), and Brunauer–Emmett–Teller (BET) surface area analysis, to understand the physical and chemical properties of the lignin-PE composites. These techniques helped to identify the different components of the composites and provided information on their surface area, porosity, and other physical and chemical characteristics that can influence their adsorption performance. The researchers found that the lignin-PE composites exhibited high adsorption capacity and fast kinetics for gold ions in aqueous solutions. The adsorption process was found to be dependent on the pH of the solution, with higher adsorption observed at lower pH values. This is because the surface of lignin is positively charged, and gold ions in solution are negatively charged, which promotes adsorption at lower pH values. The study also examined the adsorption isotherm of the lignin-PE composites, which describes the relationship between the concentration of gold ions in solution and the amount of gold adsorbed onto the composite. The researchers found that the Freundlich adsorption isotherm model provided a good fit to the data, indicating that the adsorption process involved the formation of multiple layers of gold ions on the surface of the composite. This suggests that the lignin-PE composite adsorbent can be used to effectively capture gold ions in high concentrations. Additionally, the researchers evaluated the performance of the lignin-PE composite in the presence of other cations, including As(III), As(V), Cu²⁺, Na⁺, and

Mg²⁺. Despite the presence of these competing cations, the composite still exhibited good adsorption performance towards gold ions. This suggests that the lignin-PE composite has good selectivity for gold ions and can effectively capture gold even in the presence of other metals. The study also investigated the possibility of regenerating the lignin-PE composite for reuse. The researchers found that the composite could be regenerated using a combination of HCl and NaOH solutions. This regeneration process removed the adsorbed gold ions from the composite and restored its adsorption capacity, making it possible to reuse the composite for further gold adsorption.

Overall, the research provides strong evidence for the potential of lignin-PE composites as a cost-effective, environmentally friendly, and highly selective adsorbent for gold ions in aqueous media. The findings suggest that this material has significant potential for use in gold recovery and other applications requiring selective metal capture. Further research is needed to optimize the composition of the lignin-PE composite and to evaluate its performance in real-world applications. However, this study provides an important foundation for future work in this area.

5.2 Project on LDH-GO composite adsorbents for arsenic removal

LDH-GO composite adsorbents have shown great potential for the removal of arsenic from water. The synthesized composites were characterized in detail using various techniques such as TGA, FTIR, XRD, Raman, and BET. The results showed that the iron hydroxide in the composites was primarily in the form of amorphous iron oxide nanoparticles along with crystalline α -Fe₂O₃ particles, while the magnesium complex completely matched Mg(OH)₂. These composites displayed a significantly higher arsenic adsorption capacity compared to iron oxide composites, magnesium hydroxide composites, and LDH composites.

The addition of magnesium hydroxide to the composite resulted in increased adsorption amounts of As(III) and As(V) when compared to iron oxide composites. Furthermore, the

LDH0.42-80-GO20 LDH-GO composite exhibited remarkable ability to reduce the arsenic concentration to below the WHO's drinking water limit. In terms of kinetics, the LDH-GO composite rapidly uptakes arsenic. The pH study showed that by adding magnesium complexes to the structure, we increased the pH_{PZC} of the LDH-GO composite, making it suitable for a wide range of pH levels in water and wastewater treatment. In addition, the maximum adsorption was observed at the pH of point zero charge for the LDH-GO composite. The Langmuir adsorption isotherm analysis confirmed that there was a monolayer of arsenic molecules at the surface of the composite, indicating that each site could hold only one molecule. Despite the presence of anions such as SO_4^{2-} , CO_3^{2-} , and NO_3^- , the LDH-GO composite showed good adsorption performance towards As(III) and As(V). The low cost of GO, which can be produced cost-effectively from natural graphite, and the convenient synthesis of the composites make this class of LDH-GO composites highly promising for the removal of arsenic in practical water treatment, particularly in drinking water purification. Further research is needed to optimize the synthesis and application of these composites for arsenic removal in larger-scale water treatment applications. Further analysis of the LDH-GO composite could involve exploring the effect of different metal hydroxide complexes on the composite's arsenic adsorption performance. Additionally, the study could investigate the effect of temperature and solution chemistry on the arsenic adsorption capacity of the composite. Further, experiments can be conducted on the regeneration of the used composite, to investigate its reuse potential in practical applications.

Future work could also include the development of more efficient and sustainable synthesis methods for LDH-GO composites. For instance, the use of green chemistry approaches such as microwave-assisted synthesis, sonochemistry, or biogenic synthesis could be explored. Finally, the LDH-GO composite has demonstrated excellent potential for the removal of arsenic from water sources. However, before considering practical applications, further studies on the stability of the composite in different water matrices and the potential impact

on water quality should be conducted. Additionally, further research on the optimization of the composite's synthesis and application could pave the way for its commercial production and large-scale application in water treatment.

References

- [1] gold nrcan. Gold Facts; Natural Resources Canada, <https://www.nrcan.gc.ca/our-natural-resources/minerals-mining/minerals-metals-facts/gold-facts/20514>
- [2] Hmidi N. Production and Characterization of Polystyrene Resins Containing Fine Activated Carbon Particles. Doctoral Thesis, Laurentian university, 2017
- [3] Lukey GC, Deventer JSJ van, Shallcross DC. Equilibrium Model for The Selective Sorption of Gold Cyanide On Different Ion-Exchange Functional Groups*. vol. 13. 2000.
- [4] Smedley PL, Kinniburgh DG. A review of the source, behaviour and distribution of arsenic in natural waters. *Applied Geochemistry*.2001; S0883-2927(02)00018-5.
- [5] Riveros PA, Dutrizac JE, Spencer P. Arsenic disposal practices in the metallurgical industry. *Canadian Metallurgical Quarterly* 2001;40:395–420.
<https://doi.org/10.1179/cmq.2001.40.4.395>.
- [6] Arsenic health. <https://www.canada.ca/en/health-canada/services/publications/healthy-living/guidelines-canadian-drinking-water-quality-guideline-technical-document-arsenic.html> n.d.
- [7] Mohan D, Pittman CU. Arsenic removal from water/wastewater using adsorbents-A critical review. *J Hazard Mater* 2007;142:1–53.
<https://doi.org/10.1016/j.jhazmat.2007.01.006>.
- [8] Tang SCN, Lo IMC. Magnetic nanoparticles: Essential factors for sustainable environmental applications. *Water Res* 2013;47:2613–32.
<https://doi.org/10.1016/j.watres.2013.02.039>.

- [9] Parajuli D, Adhikari CR, Kuriyama M, Kawakita H, Ohto K, Inoue K, et al. Selective recovery of gold by novel lignin-based adsorption gels. *Ind Eng Chem Res* 2006;45:8–14. <https://doi.org/10.1021/ie050532u>.
- [10] Kotte P, Yun YS. L-cysteine impregnated alginate capsules as a sorbent for gold recovery. *Polym Degrad Stab* 2014;109:424–9. <https://doi.org/10.1016/j.polymdegradstab.2014.02.014>.
- [11] An FQ, Li M, Guo XD, Wang HY, Wu RY, Hu TP, et al. Selective adsorption of AuCl₄⁻ on chemically modified D301 resin with containing N/S functional polymer. *J Environ Chem Eng* 2017;5:10–5. <https://doi.org/10.1016/j.jece.2016.11.010>.
- [12] Fan R, Xie F, Guan X, Zhang Q, Luo Z. Selective adsorption and recovery of Au(III) from three kinds of acidic systems by persimmon residual based bio-sorbent: A method for gold recycling from e-wastes. *Bioresour Technol* 2014;163:167–71. <https://doi.org/10.1016/j.biortech.2014.03.164>.
- [13] Shen YF, Xue WY. Recovery palladium, gold and platinum from hydrochloric acid solution using 2-hydroxy-4-sec-octanoyl diphenyl-ketoxime. *Sep Purif Technol* 2007;56:278–83. <https://doi.org/10.1016/j.seppur.2007.02.001>.
- [14] Ogata T, Nakano Y. Mechanisms of gold recovery from aqueous solutions using a novel tannin gel adsorbent synthesized from natural condensed tannin. *Water Res* 2005;39:4281–6. <https://doi.org/10.1016/j.watres.2005.06.036>.
- [15] Torres E, Mata YN, Blázquez ML, Muñoz JA, González F, Ballester A. Gold and silver uptake and nanoprecipitation on calcium alginate beads. *Langmuir* 2005;21:7951–8. <https://doi.org/10.1021/la046852k>.
- [16] Gomes CP, Almeida MF, Loureiro JM. Gold recovery with ion exchange used resins. *Separation and Purification Technology*, vol. 24. 2001.

- [17] Dwivedi AD, Dubey SP, Hokkanen S, Fallah RN, Sillanpää M. Recovery of gold from aqueous solutions by taurine modified cellulose: An adsorptive-reduction pathway. *Chemical Engineering Journal* 2014;255:97–106.
<https://doi.org/10.1016/j.cej.2014.06.017>.
- [18] Duan Y, Freyburger A, Kunz W, Zollfrank C. Lignin/Chitin Films and Their Adsorption Characteristics for Heavy Metal Ions. *ACS Sustain Chem Eng* 2018;6:6965–73.
<https://doi.org/10.1021/acssuschemeng.8b00805>.
- [19] Sahoo S, Misra M, Mohanty AK. Enhanced properties of lignin-based biodegradable polymer composites using injection moulding process. *Compos Part A Appl Sci Manuf* 2011;42:1710–8. <https://doi.org/10.1016/j.compositesa.2011.07.025>.
- [20] Luo S, Cao J, Sun W. Evaluation of Kraft lignin as natural compatibilizer in wood flour/polypropylene composites. *Polym Compos* 2017;38:2387–94.
<https://doi.org/10.1002/pc.23821>.
- [21] Luo F, Ning N-Y, Chen L, Su R, Cao J, Zhang Q, et al. Effects of Compatibilizers on The Mechanical Properties of Low-Density Polyethylene/Lignin Blends , *Chinese Journal of Polymer Science*. vol. 27. 2009.
- [22] Lalvani SB, Hübner A, Wiltowski TS. Chromium adsorption by lignin. *Energy Sources* 2000;22:45–56. <https://doi.org/10.1080/00908310050014207>.
- [23] Adhikari BB, Gurung M, Alam S, Tolnai B, Inoue K. Kraft mill lignin - A potential source of bio-adsorbents for gold recovery from acidic chloride solution. *Chemical Engineering Journal* 2013;231:190–7. <https://doi.org/10.1016/j.cej.2013.07.016>.
- [24] Guo X, Zhang S, Shan X quan. Adsorption of metal ions on lignin. *J Hazard Mater* 2008;151:134–42. <https://doi.org/10.1016/j.jhazmat.2007.05.065>.

- [25] Zhang X, Zhao G, Shi X, Yuan B, Zhao K, Tian Z, et al. Loading ferric lignin on polyethylene film and its influence on arsenic-polluted soil and growth of romaine lettuce plant. *Environmental Science and Pollution Research* 2022;29:50362–75. <https://doi.org/10.1007/s11356-022-19490-7>.
- [26] He J, Ni F, Cui A, Chen X, Deng S, Shen F, et al. New insight into adsorption and co-adsorption of arsenic and tetracycline using a Y-immobilized graphene oxide-alginate hydrogel: Adsorption behaviours and mechanisms. *Science of the Total Environment* 2020;701. <https://doi.org/10.1016/j.scitotenv.2019.134363>.
- [27] Mandal BK, Suzuki KT. Arsenic round the world: a review. vol. 58. 2002.
- [28] Chandra V, Park J, Chun Y, Lee JW, Hwang IC, Kim KS. Water-dispersible magnetite-reduced graphene oxide composites for arsenic removal. *ACS Nano* 2010;4:3979–86. <https://doi.org/10.1021/nn1008897>.
- [29] Shankar S, Shanker U, Shikha. Arsenic contamination of groundwater: A review of sources, prevalence, health risks, and strategies for mitigation. *Scientific World Journal* 2014;2014. <https://doi.org/10.1155/2014/304524>.
- [30] Choong TSY, Chuah TG, Robiah Y, Gregory Koay FL, Azni I. Arsenic toxicity, health hazards and removal techniques from water: an overview. *Desalination* 2007;217:139–66. <https://doi.org/10.1016/j.desal.2007.01.015>.
- [31] Li W, Chen D, Xia F, Tan JZY, Huang PP, Song WG, et al. Extremely high arsenic removal capacity for mesoporous aluminium magnesium oxide composites. *Environ Sci Nano* 2016;3:94–106. <https://doi.org/10.1039/c5en00171d>.
- [32] Sullivan C, Tyrer M, Cheeseman CR, Graham NJD. Disposal of water treatment wastes containing arsenic - A review. *Science of the Total Environment* 2010;408:1770–8. <https://doi.org/10.1016/j.scitotenv.2010.01.010>.

- [33] Chen L, Xin H, Fang Y, Zhang C, Zhang F, Cao X, et al. Application of metal oxide heterostructures in arsenic removal from contaminated water. *J Nanomater* 2014;2014. <https://doi.org/10.1155/2014/793610>.
- [34] Yuan T, Luo QF, Hu JY, Ong SL, Ng WJ. A study on arsenic removal from household drinking water. *J Environ Sci Health A Tox Hazard Subst Environ Eng* 2003;38:1731–44. <https://doi.org/10.1081/ESE-120022875>.
- [35] Jia Y, Zhang D, Pan R, Xu L, Demopoulos GP. A novel two-step coprecipitation process using Fe(III) and Al(III) for the removal and immobilization of arsenate from acidic aqueous solution. *Water Res* 2012;46:500–8. <https://doi.org/10.1016/j.watres.2011.11.045>.
- [36] Li Z, Jean JS, Jiang WT, Chang PH, Chen CJ, Liao L. Removal of arsenic from water using Fe-exchanged natural zeolite. *J Hazard Mater* 2011;187:318–23. <https://doi.org/10.1016/j.jhazmat.2011.01.030>.
- [37] Vaclavikova M, Gallios GP, Hredzak S, Jakabsky S. Removal of arsenic from water streams: An overview of available techniques. *Clean Technol Environ Policy* 2008;10:89–95. <https://doi.org/10.1007/s10098-007-0098-3>.
- [38] Pokhrel D, Viraraghavan T. Arsenic removal from an aqueous solution by modified *A. niger* biomass: Batch kinetic and isotherm studies. *J Hazard Mater* 2008;150:818–25. <https://doi.org/10.1016/j.jhazmat.2007.05.041>.
- [39] Taghipour S, Hosseini SM, Ataie-Ashtiani B. Engineering nanomaterials for water and wastewater treatment: Review of classifications, properties and applications. *New Journal of Chemistry* 2019;43:7902–27. <https://doi.org/10.1039/c9nj00157c>.
- [40] Soner Altundogae H, Altundogae S, Bildik M. Arsenic removal from aqueous solutions by adsorption on red mud n.d.

- [41] Pollard SJT, Fowler GD, Sollars CJ, Perry R. Low-cost adsorbents for waste and wastewater treatment: a review. 1992.
- [42] Lee CK, Low KS, Liew SC, Choo CS. Removal of arsenic(v) from aqueous solution by quaternized rice husk. *Environmental Technology (United Kingdom)* 1999;20:971–8. <https://doi.org/10.1080/09593332008616892>.
- [43] Manju GN, Raji C, Anirudhan TS. Evaluation of coconut husk carbon for the removal of arsenic from water n.d.
- [44] Aloysius U. Baes. Adsorption and ion exchange of some groundwater anion contaminants in an amine modified coconut coir. *Elsevier Science Ltd* 1997;35:89–95.
- [45] Ghimire KN, Inoue K, Makino K, Miyajima T. Adsorptive removal of arsenic using orange juice residue. *Sep Sci Technol* 2002;37:2785–99. <https://doi.org/10.1081/SS-120005466>.
- [46] Murugesan GS, Sathishkumar M, Swaminathan K. Arsenic removal from groundwater by pretreated waste tea fungal biomass. *Bioresour Technol* 2006;97:483–7. <https://doi.org/10.1016/j.biortech.2005.03.008>.
- [47] Guo X, Chen F. Removal of arsenic by bead cellulose loaded with iron oxyhydroxide from groundwater. *Environ Sci Technol* 2005;39:6808–18. <https://doi.org/10.1021/es048080k>.
- [48] Clara M, Magalhães F. Arsenic. An environmental problem limited by solubility*. vol. 74. 2002.
- [49] Giles DE, Mohapatra M, Issa TB, Anand S, Singh P. Iron and aluminium based adsorption strategies for removing arsenic from water. *J Environ Manage* 2011;92:3011–22. <https://doi.org/10.1016/j.jenvman.2011.07.018>.

- [50] Jiang J-Q. Removing arsenic from groundwater for the developing world-a review 2001.
- [51] Han C, Li H, Pu H, Yu H, Deng L, Huang S, et al. Synthesis and characterization of mesoporous alumina and their performances for removing arsenic(V). *Chemical Engineering Journal* 2013;217:1–9. <https://doi.org/10.1016/j.cej.2012.11.087>.
- [52] Pena M, Meng X, Korfiatis GP, Jing C. Adsorption mechanism of arsenic on nanocrystalline titanium dioxide. *Environ Sci Technol* 2006;40:1257–62. <https://doi.org/10.1021/es052040e>.
- [53] Ashraf S, Siddiqa A, Shahida S, Qaisar S. Titanium-based nanocomposite materials for arsenic removal from water: A review. *Heliyon* 2019;5. <https://doi.org/10.1016/j.heliyon.2019.e01577>.
- [54] Purwajanti S, Zhang H, Huang X, Song H, Yang Y, Zhang J, et al. Mesoporous Magnesium Oxide Hollow Spheres as Superior Arsenite Adsorbent: Synthesis and Adsorption Behavior. *ACS Appl Mater Interfaces* 2016;8:25306–12. <https://doi.org/10.1021/acsami.6b08322>.
- [55] Liu Y, Li Q, Gao S, Shang JK. Exceptional As(III) sorption capacity by highly porous magnesium oxide nanoflakes made from hydrothermal synthesis. *Journal of the American Ceramic Society* 2011;94:217–23. <https://doi.org/10.1111/j.1551-2916.2010.04043.x>.
- [56] Tresintsi S, Simeonidis K, Katsikini M, Paloura EC, Bantsis G, Mitrakas M. A novel approach for arsenic adsorbents regeneration using MgO. *J Hazard Mater* 2014;265:217–25. <https://doi.org/10.1016/j.jhazmat.2013.12.003>.
- [57] Purwajanti S, Huang X, Liu Y, Yang Y, Noonan O, Song H, et al. Mg(OH)₂-MgO@reduced graphene oxide nanocomposites: The roles of composition and

- nanostructure in arsenite sorption. *J Mater Chem A Mater* 2017;5:24484–92.
<https://doi.org/10.1039/c7ta07629k>.
- [58] Kameda K, Hashimoto Y, Ok YS. Stabilization of arsenic and lead by magnesium oxide (MgO) in different seawater concentrations. *Environmental Pollution* 2018;233:952–9. <https://doi.org/10.1016/j.envpol.2017.09.067>.
- [59] Sikdar S, Ghosh A, Saha R. Synthesis of MgO micro-rods coated with charred dextrose and its application for the adsorption of selected heavy metals from synthetic and real groundwater. *Environmental Science and Pollution Research* 2020;27:17738–53. <https://doi.org/10.1007/s11356-020-08106-7>.
- [60] Thirunavukkarasu OS, Viraraghavan T, Subramanian KS. Arsenic Removal From Drinking Water Using Iron Oxide-Coated Sand 2003.
- [61] Tang W, Li Q, Gao S, Shang JK. Arsenic (III,V) removal from aqueous solution by ultrafine α -Fe₂O₃ nanoparticles synthesized from solvent thermal method. *J Hazard Mater* 2011;192:131–8. <https://doi.org/10.1016/j.jhazmat.2011.04.111>.
- [62] Zhong LS, Hu JS, Liang HP, Cao AM, Song WG, Wan LJ. Self-assembled 3D flowerlike iron oxide nanostructures and their application in water treatment. *Advanced Materials* 2006;18:2426–31. <https://doi.org/10.1002/adma.200600504>.
- [63] Mamindy-Pajany Y, Hurel C, Marmier N, Roméo M. Arsenic adsorption onto hematite and goethite. *Comptes Rendus Chimie* 2009;12:876–81.
<https://doi.org/10.1016/j.crci.2008.10.012>.
- [64] Hlavay J, Polyák K. Determination of surface properties of iron hydroxide-coated alumina adsorbent prepared for removal of arsenic from drinking water. *J Colloid Interface Sci* 2005;284:71–7. <https://doi.org/10.1016/j.jcis.2004.10.032>.

- [65] Lin YF, Chen JL. Synthesis of mesoporous maghemite (γ -Fe₂O₃) nanostructures with enhanced arsenic removal efficiency. *RSC Adv* 2013;3:15344–9. <https://doi.org/10.1039/c3ra41596a>.
- [66] Babu CM, Palanisamy B, Sundaravel B, Palanichamy M, Murugesan V. A novel magnetic Fe₃O₄/SiO₂ core-shell nanorods for the removal of arsenic. *J Nanosci Nanotechnol* 2013;13:2517–27. <https://doi.org/10.1166/jnn.2013.7376>.
- [67] Feng L, Cao M, Ma X, Zhu Y, Hu C. Superparamagnetic high-surface-area Fe₃O₄ nanoparticles as adsorbents for arsenic removal. *J Hazard Mater* 2012;217–218:439–46. <https://doi.org/10.1016/j.jhazmat.2012.03.073>.
- [68] Maji SK, Kao YH, Liao PY, Lin YJ, Liu CW. Implementation of the adsorbent iron-oxide-coated natural rock (IOCNR) on synthetic As(III) and on real arsenic-bearing sample with filter. *Appl Surf Sci* 2013;284:40–8. <https://doi.org/10.1016/j.apsusc.2013.06.154>.
- [69] Tang W, Su Y, Li Q, Gao S, Shang JK. Mg-doping: A facile approach to impart enhanced arsenic adsorption performance and easy magnetic separation capability to α -Fe₂O₃ nanoadsorbents. *J Mater Chem A Mater* 2013;1:830–6. <https://doi.org/10.1039/c2ta00271j>.
- [70] Zhang G, Liu H, Qu J, Jefferson W. Arsenate uptake and arsenite simultaneous sorption and oxidation by Fe-Mn binary oxides: Influence of Mn/Fe ratio, pH, Ca²⁺, and humic acid. *J Colloid Interface Sci* 2012;366:141–6. <https://doi.org/10.1016/j.jcis.2011.09.058>.
- [71] Yue X, Zhao J, Shi H, Chi Y, Salam M. Preparation of composite adsorbents of activated carbon supported MgO/MnO₂ and adsorption of Rhodamine B. *Water Science and Technology* 2020;81:906–17. <https://doi.org/10.2166/wst.2020.172>.

- [72] Ren Z, Zhang G, Paul Chen J. Adsorptive removal of arsenic from water by an iron-zirconium binary oxide adsorbent. *J Colloid Interface Sci* 2011;358:230–7. <https://doi.org/10.1016/j.jcis.2011.01.013>.
- [73] Gupta K, Biswas K, Ghosh UC. Nanostructure iron(III)-zirconium(IV) binary mixed oxide: Synthesis, characterization, and physicochemical aspects of arsenic(III) sorption from the aqueous solution. *Ind Eng Chem Res* 2008;47:9903–12. <https://doi.org/10.1021/ie8002107>.
- [74] Zhang Y, Yang M, Dou XM, He H, Wang DS. Arsenate adsorption on an Fe-Ce bimetal oxide adsorbent: Role of surface properties. *Environ Sci Technol* 2005;39:7246–53. <https://doi.org/10.1021/es050775d>.
- [75] Shan C, Tong M. Efficient removal of trace arsenite through oxidation and adsorption by magnetic nanoparticles modified with Fe-Mn binary oxide. *Water Res* 2013;47:3411–21. <https://doi.org/10.1016/j.watres.2013.03.035>.
- [76] Maliyekkal SM, Philip L, Pradeep T. As(III) removal from drinking water using manganese oxide-coated-alumina: Performance evaluation and mechanistic details of surface binding. *Chemical Engineering Journal* 2009;153:101–7. <https://doi.org/10.1016/j.cej.2009.06.026>.
- [77] Peng F, Luo T, Yuan Y. Controllable synthesis of Mg-Fe layered double hydroxide nanoplates with specific Mg/Fe ratios and their effect on adsorption of As(v) from water. *New Journal of Chemistry* 2014;38:4427–33. <https://doi.org/10.1039/c4nj00548a>.
- [78] Wang Y, Gao Y, Zhu Z, Zhang L, Zhao N, Fang Y, et al. Enhanced Arsenic Removal from Aqueous Solution by Fe/Mn-C Layered Double Hydroxide Composite. *Adsorption Science and Technology* 2021;2021. <https://doi.org/10.1155/2021/8891643>.

- [79] Kim S. Stabilization effect of Mg-Fe layered double hydroxide (LDH) for arsenic-contaminated soil. 2022.
- [80] Chen Y, Bai X, Ye Z. Recent progress in heavy metal ion decontamination based on metal-organic frameworks. *Nanomaterials* 2020;10:1-23.
<https://doi.org/10.3390/nano10081481>.
- [81] Yu W, Luo M, Yang Y, Wu H, Huang W, Zeng K, et al. Metal-organic framework (MOF) showing both ultrahigh As(V) and As(III) removal from aqueous solution. *J Solid State Chem* 2019;269:264-70. <https://doi.org/10.1016/j.jssc.2018.09.042>.
- [82] Hua M, Zhang S, Pan B, Zhang W, Lv L, Zhang Q. Heavy metal removal from water/wastewater by nanosized metal oxides: A review. *J Hazard Mater* 2012;211-212:317-31. <https://doi.org/10.1016/j.jhazmat.2011.10.016>.
- [83] Sherlala AIA, Raman AAA, Bello MM. Synthesis and characterization of magnetic graphene oxide for arsenic removal from aqueous solution. *Environmental Technology (United Kingdom)* 2019;40:1508-16.
<https://doi.org/10.1080/09593330.2018.1424259>.
- [84] Mohan VB. Handling and Risk Mitigation of Nanoscale Graphene and Related Materials: Some Considerations and Recommendations. *C (Basel)* 2019;5:36.
<https://doi.org/10.3390/c5030036>.
- [85] Marcano DC, Kosynkin D v., Berlin JM, Sinitskii A, Sun Z, Slesarev A, et al. Improved synthesis of graphene oxide. *ACS Nano* 2010;4:4806-14.
<https://doi.org/10.1021/nn1006368>.
- [86] Su H, Ye Z, Hmidi N. High-performance iron oxide-graphene oxide nanocomposite adsorbents for arsenic removal. *Colloids Surf A Physicochem Eng Asp* 2017;522:161-72. <https://doi.org/10.1016/j.colsurfa.2017.02.065>.

- [87] Huang D, Li B, Wu M, Kuga S, Huang Y. Graphene Oxide-Based Fe-Mg (Hydr)oxide Nanocomposite as Heavy Metals Adsorbent. *J Chem Eng Data* 2018;63:2097–105. <https://doi.org/10.1021/acs.jced.8b00100>.
- [88] Guo T, Bulin C. Facile preparation of MgO/graphene oxide nanocomposite for efficient removal of aqueous Congo red: adsorption performance and interaction mechanism. *Research on Chemical Intermediates* 2021;47:945–71. <https://doi.org/10.1007/s11164-020-04310-9>.
- [89] Narayanaswamy V, Obaidat IM, Kamzin AS, Latiyan S, Jain S, Kumar H, et al. Synthesis of graphene oxide-Fe₃O₄ based nanocomposites using the mechanochemical method and in vitro magnetic hyperthermia. *Int J Mol Sci* 2019;20. <https://doi.org/10.3390/ijms20133368>.
- [90] Lee JR, Koo HY. Growth of magnesium oxide nanoparticles onto graphene oxide nanosheets by sol-gel process. *Carbon Letters* 2013;14:206–9. <https://doi.org/10.5714/cl.2013.14.4.206>.
- [91] Heidarizad M, Şengör SS. Synthesis of graphene oxide/magnesium oxide nanocomposites with high-rate adsorption of methylene blue. *J Mol Liq* 2016;224:607–17. <https://doi.org/10.1016/j.molliq.2016.09.049>.
- [92] Xu Z, Li Q, Gao S, Shang JK. As(III) removal by hydrous titanium dioxide prepared from one-step hydrolysis of aqueous TiCl₄ solution. *Water Res* 2010;44:5713–21. <https://doi.org/10.1016/j.watres.2010.05.051>.
- [93] Doušová B, Grygar T, Martaus A, Fuitová L, Koloušek D, Machovič V. Sorption of AsV on aluminosilicates treated with FeII nanoparticles. *J Colloid Interface Sci* 2006;302:424–31. <https://doi.org/10.1016/j.jcis.2006.06.054>.

- [94] Gupta AK, Kumar Gupta A, Mohanty S, Nayak SK. Preparation and Characterization of Lignin Nanofibre by Electrospinning Technique. *International Journal of Scientific Engineering and Applied Science (IJSEAS)* 2015.
- [95] Goudarzi A, Lin LT, Ko FK. X-ray diffraction analysis of kraft lignins and lignin-derived carbon nanofibers. *J Nanotechnol Eng Med* 2014;5.
<https://doi.org/10.1115/1.4028300>.
- [96] Alnaimi S, Elouadi B, Kamal I. Structural, Thermal and Morphology Characteristics of Low Density Polyethylene Produced by QAPCO. *Structural, Thermal and Morphology Characteristics of Low Density Polyethylene Produced by QAPCO*. 2015.
- [97] Serna DL, Martínez PE, González MÁR, Cadena AAZ, Contreras EAZ, Anguiano MGS. Synthesis and characterization of a lignin-styrene-butyl acrylate based composite. *Polymers (Basel)* 2019;11. <https://doi.org/10.3390/POLYM11061080>.
- [98] Zhao J, Xiuwen W, Hu J, Liu Q, Shen D, Xiao R. Thermal degradation of softwood lignin and hardwood lignin by TG-FTIR and Py-GC/MS. *Polym Degrad Stab* 2014;108:133–8. <https://doi.org/10.1016/j.polymdegradstab.2014.06.006>.
- [99] Tang Y, Jean M, Pourebrahimi S, Rodrigue D, Ye Z. Influence of lignin structure change during extrusion on properties and recycling of lignin-polyethylene thermoplastic composites. *Canadian Journal of Chemical Engineering* 2021;99:S27–38. <https://doi.org/10.1002/cjce.23960>.
- [100] Celik A, Demirbaş A. Removal of heavy metal ions from aqueous solutions via adsorption onto modified lignin from pulping wastes. *Energy Sources* 2005;27:1167–77. <https://doi.org/10.1080/00908310490479583>.

- [101] He ZW, He LH, Yang J, Lü QF. Removal and recovery of Au(III) from aqueous solution using a low-cost lignin-based biosorbent. *Ind Eng Chem Res* 2013;52:4103–8. <https://doi.org/10.1021/ie303410g>.
- [102] Angai JU, Ptacek CJ, Pakostova E, Bain JG, Verbuyst BR, Blowes DW. Removal of arsenic and metals from groundwater impacted by mine waste using zero-valent iron and organic carbon: Laboratory column experiments. *J Hazard Mater* 2022;424. <https://doi.org/10.1016/j.jhazmat.2021.127295>.
- [103] Zhang W, Che J, Xia L, Wen P, Chen J, Ma B, et al. Efficient removal and recovery of arsenic from copper smelting flue dust by a roasting method: Process optimization, phase transformation and mechanism investigation. *J Hazard Mater* 2021;412. <https://doi.org/10.1016/j.jhazmat.2021.125232>.
- [104] Rathi BS, Kumar PS. A review on sources, identification and treatment strategies for the removal of toxic Arsenic from water system. *J Hazard Mater* 2021;418. <https://doi.org/10.1016/j.jhazmat.2021.126299>.
- [105] Carneiro MA, Pintor AMA, Boaventura RAR, Botelho CMS. Efficient removal of arsenic from aqueous solution by continuous adsorption onto iron-coated cork granulates. *J Hazard Mater* 2022;432. <https://doi.org/10.1016/j.jhazmat.2022.128657>.
- [106] Guan X, Yuan X, Zhao Y, Bai J, Li Y, Cao Y, et al. Adsorption behaviors and mechanisms of Fe/Mg layered double hydroxide loaded on bentonite on Cd (II) and Pb (II) removal. *J Colloid Interface Sci* 2022;612:572–83. <https://doi.org/10.1016/j.jcis.2021.12.151>.
- [107] Elmoubarki R, Mahjoubi FZ, Elhalil A, Tounsadi H, Abdennouri M, Sadiq M, et al. Ni/Fe and Mg/Fe layered double hydroxides and their calcined derivatives: Preparation, characterization and application on textile dyes removal. *Journal of*

- Materials Research and Technology 2017;6:271–83.
<https://doi.org/10.1016/j.jmrt.2016.09.007>.
- [108] Halajnia A, Oustan S, Najafi N, Khataee AR, Lakzian A. The adsorption characteristics of nitrate on Mg-Fe and Mg-Al layered double hydroxides in a simulated soil solution. *Appl Clay Sci* 2012;70:28–36. <https://doi.org/10.1016/j.clay.2012.09.007>.
- [109] Benselka-Hadj Abdelkader N, Bentouami A, Derriche Z, Bettahar N, de Ménorval LC. Synthesis and characterization of Mg-Fe layer double hydroxides and its application on adsorption of Orange G from aqueous solution. *Chemical Engineering Journal* 2011;169:231–8. <https://doi.org/10.1016/j.cej.2011.03.019>.
- [110] Nagpal M, Kakkar R. Facile synthesis of mesoporous magnesium oxide–graphene oxide composite for efficient and highly selective adsorption of hazardous anionic dyes. *Research on Chemical Intermediates* 2020;46:2497–521.
<https://doi.org/10.1007/s11164-020-04103-0>.
- [111] Najafi M, Sadeghi Chevinli A, Srivastava V, Sillanpää M. Augmentation of Neodymium Ions Removal from Water Using Two Lanthanides-Based MOF: Ameliorated Efficiency by Synergistic Interaction of Two Lanthanides. *J Chem Eng Data* 2019;64:3105–12. <https://doi.org/10.1021/acs.jced.9b00207>.
- [112] Bhargava R, Khan S. Effect of reduced graphene oxide (rGO) on structural, optical, and dielectric properties of Mg(OH)₂/rGO nanocomposites. *Advanced Powder Technology* 2017;28:2812–9. <https://doi.org/10.1016/j.apt.2017.08.008>.
- [113] Lu H, Zhu Z, Zhang H, Qiu Y. In Situ Oxidation and Efficient Simultaneous Adsorption of Arsenite and Arsenate by Mg-Fe-LDH with Persulfate Intercalation. *Water Air Soil Pollut* 2016;227. <https://doi.org/10.1007/s11270-016-2828-9>.

[114] Khan SU, Zaidi R, Shaik F, Farooqi IH, Azam A, Abuhimd H, et al. Evaluation of fe-mg binary oxide for as (Iii) adsorption—synthesis, characterization and kinetic modelling. *Nanomaterials* 2021;11:1–16. <https://doi.org/10.3390/nano11030805>.

Appendix

Chapter 3

Supporting information of Chapter 3

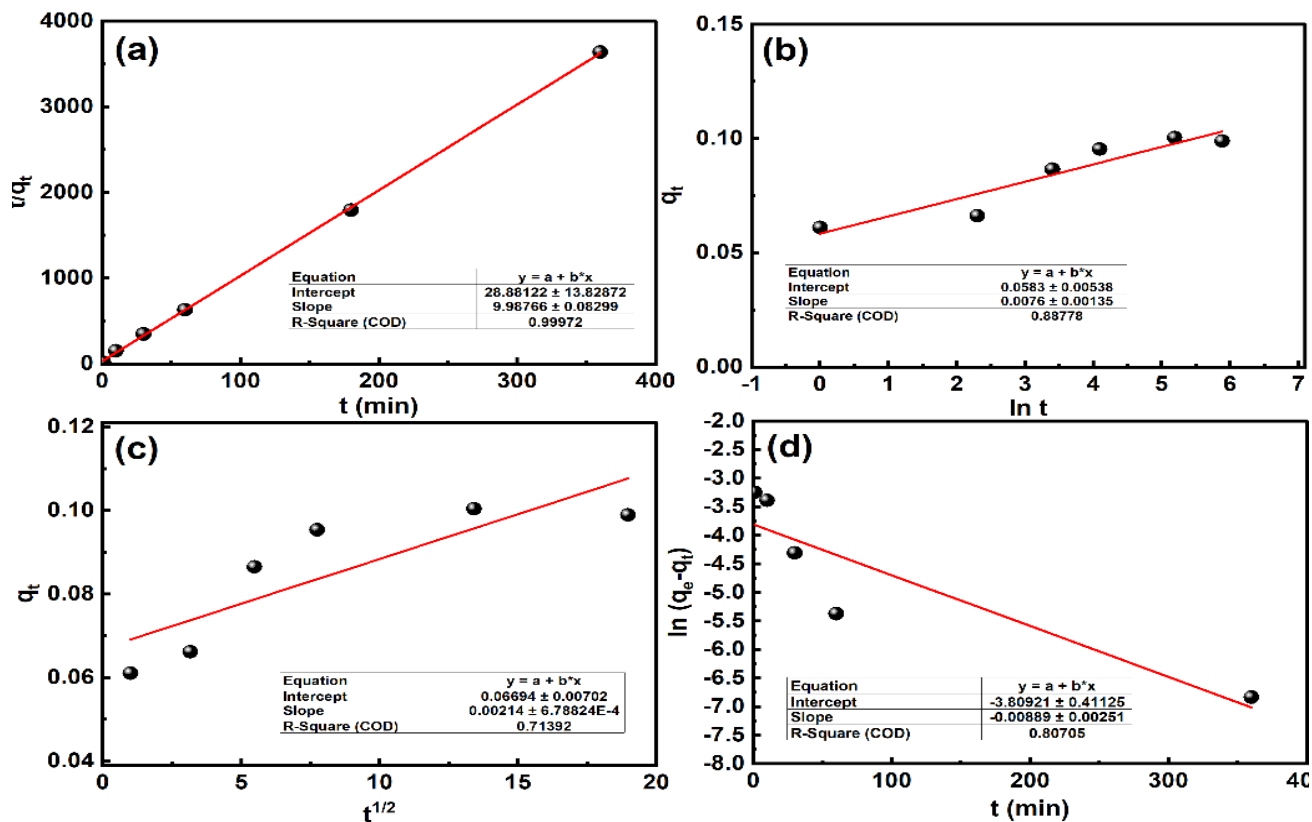


Figure 0-1: Fitting of the adsorption kinetics of L40-PE60 with different kinetic models: (a) pseudo second order, (b) Elovich, (c) intraparticle diffusion, (d) pseudo first order models. The adsorption took place at initial Au(III) concentration of 10 mg L⁻¹, adsorbent dosage of 100 mg L⁻¹, and pH=6.8.

Table A-1: Fitting parameters of Au(III) adsorption kinetic of L40-PE60 with different models

Model	Parameters	Au(III)
Pseudo-first order	q_e (mg g ⁻¹)	0.0182
	K (min ⁻¹)	0.0083
	R ²	0.8054
Pseudo-second order	q_e (mg g ⁻¹)	0.1001
	K (g mg ⁻¹ .min ⁻¹)	3.4539
	R ²	0.9997
Diffusion	C (mg g ⁻¹)	0.0669
	K(mg/g.min ^{1/2})	0.0021
	R ²	0.7139
Elovich	α (mg/g.min)	0.0076
	β (g mg ⁻¹)	0.0583
	R ²	0.8878

Table 0-2: Fitting parameters of Au(III) adsorption isotherms with L40-PE60

Isotherm	Parameters	Au(III)
Langmuir	q_m (mg/g)	0.095
	K_L (L/mg)	89.28
	R ²	0.9641
Freundlich	K_F (mg/g)	0.3446
	n	2.06
	R ²	0.9709
Temkin	K_T (L/g)	480.14
	b_T (J/mol)	90222
	R ²	0.8194

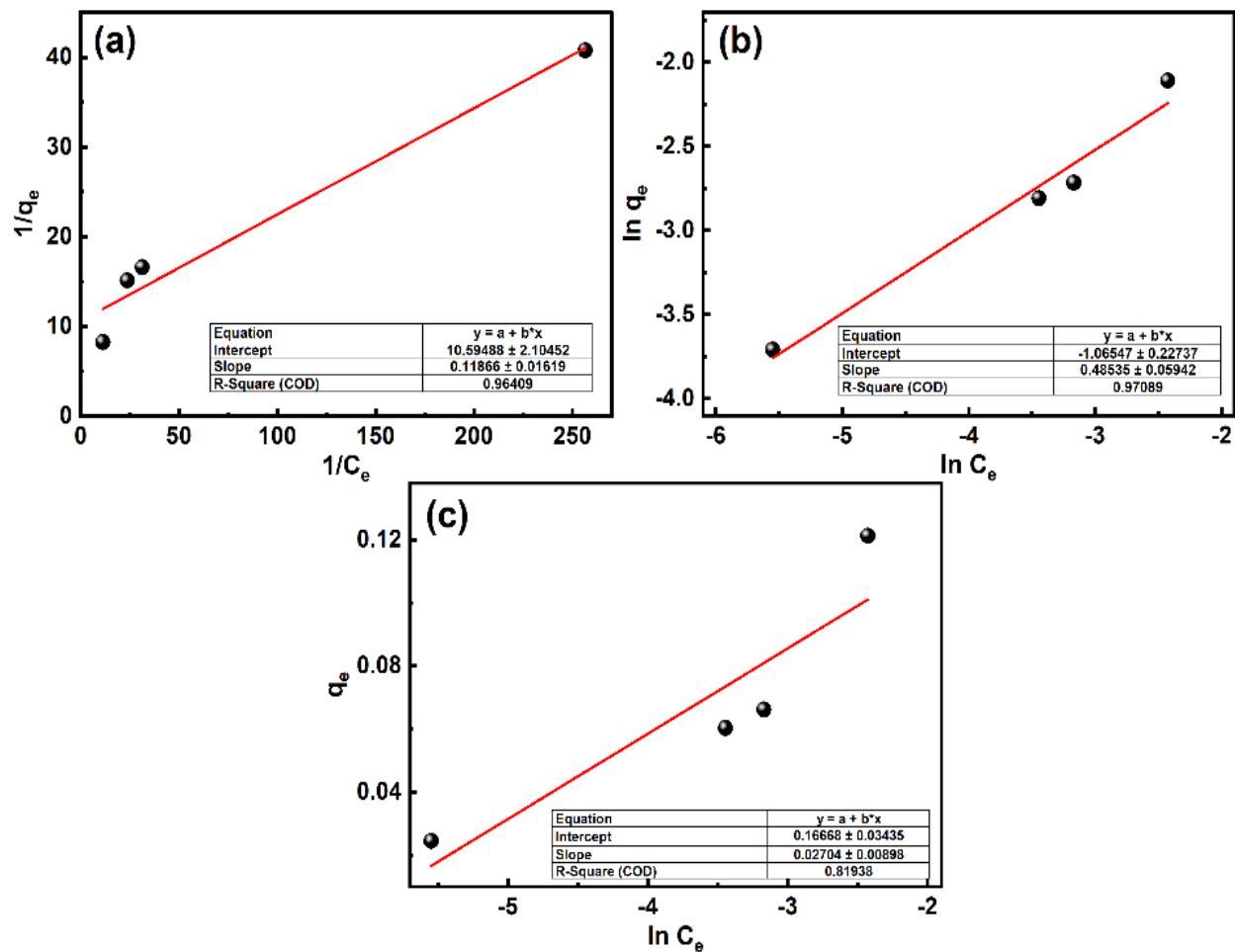


Figure 0-2: Fitting of the adsorption isotherm of L40-PE60 toward Au(III) with different models: (a) Langmuir, (b) Freundlich, (c) Temkin. The isotherm was obtained at the adsorbent dosage of 100 mg L⁻¹ and pH of 6.8.

Chapter 4

Supporting information of second paper

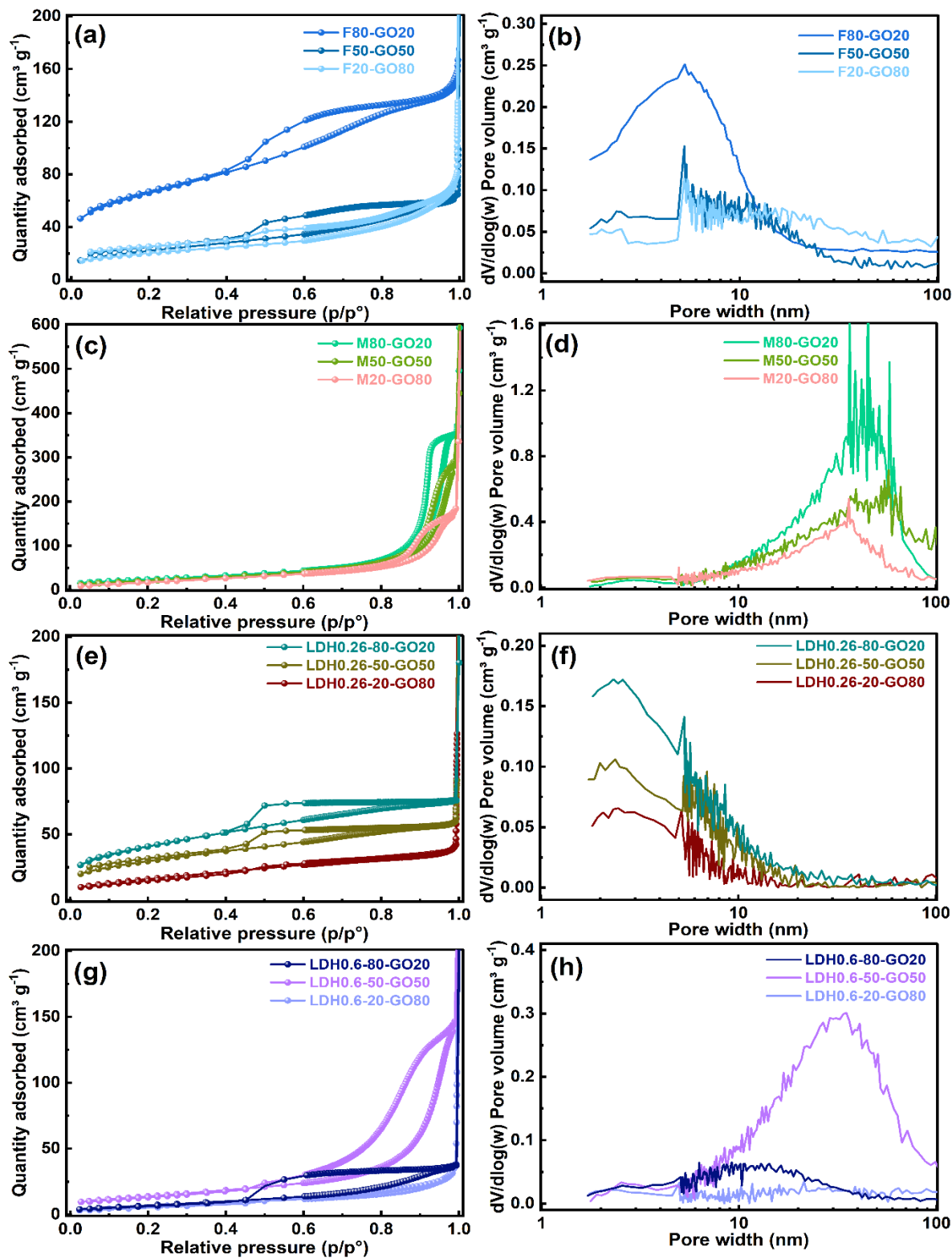


Figure 0-3: N₂ sorption isotherms of α -Fe₂O₃-GO (a), Mg(OH)₂-GO (c), LDH-GO composites (e, g) and their NLDFT meso-/macro-pore size distribution curves(b, d, f, h).

Table 0-3: BET surface area, adsorption capacity, and zeta potential of representative composites and GO.

Composite	BET (m ² g ⁻¹)	Adsorption Capacity (mg g ⁻¹)		Zeta potential (mV)
		As(III)	As(V)	
GO	100	4.3	12.2	-39
F20-GO80	70.5		17.2	-30
F50-GO50	167		17.3	-21
F80-GO20	227	89.5	52.7	-2.3
M20-GO80	72.8		21.2	-7.6
M50-GO50	81.8		17.4	-6.5
M80-GO20	88.8	32.7	15.2	7.5
LDH0.60-80-GO20	27.2	22	36	-26.3
LDH0.42-80-GO20	189.4	63.4	56.1	2.1
LDH0.26-80-GO20	145.6	40	33	0.1
LDH0.60-50-GO50	50.3		28.9	-29.8
LDH0.42-50-GO50	78.5		41.8	-14
LDH0.26-50-GO50	105.6		31.2	-23
LDH0.60-20-GO80	25.2		19.8	-29.6
LDH0.42-20-GO80	54.3		21.5	-16.6
LDH0.26-20-GO80	60.3		23.8	-32

Table 0-4: List of adsorption isotherm models.

Isotherm	Equation
Langmuir	$\frac{C_e}{q_e} = \frac{1}{q_m} C_e + \frac{1}{K_L q_m}$
Freundlich	$\ln q_e = \ln K_F + \left(\frac{1}{n}\right) \ln C_e$
Tempkin	$q = \frac{RT}{b_T} \ln K_T C_e$

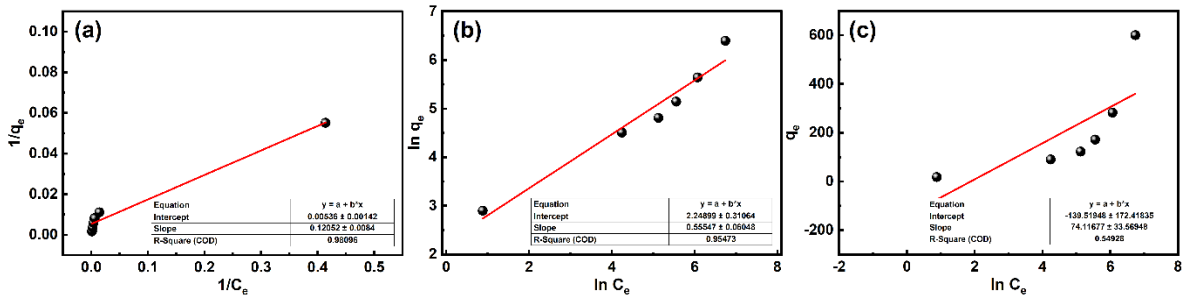


Figure A-4: Fittings of the As(III) adsorption isotherm of LDH0.42-80-GO20 with (a) Langmuir, (b) Freundlich, and (c) Temkin models.

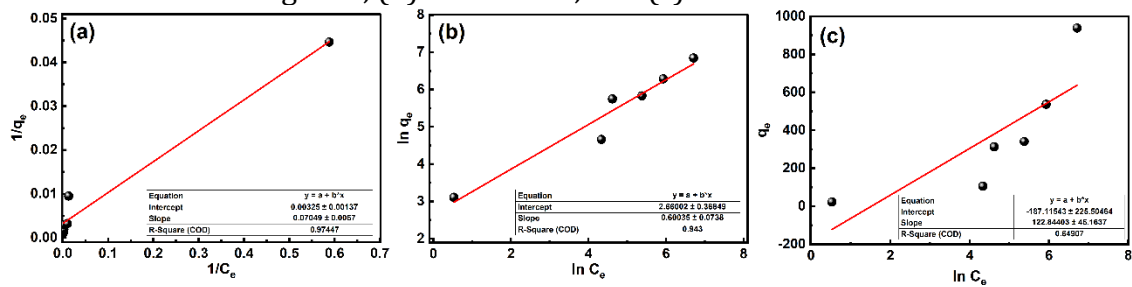


Figure 0-5: Fittings of the As(V) adsorption isotherm of LDH0.42-80-GO20 with (a) Langmuir, (b) Freundlich, and (c) Temkin models.

Table 0-5: Fitting parameters of arsenic adsorption isotherms with LDH0.42-80-GO20

Isotherm	Parameters	As(III)	As(V)
Langmuir	$q_m(\text{mg/g})$	186.5	307.7

	$K_L(\text{L/mg})$	0.044	0.046
	R^2	0.981	0.975
Freundlich	$K_F(\text{mg/g})$	9.477	14.296
	n	1.8	1.667
	R^2	0.954	0.943
Temkin	$K_T(\text{L/g})$	0.152	0.218
	$b_T(\text{J/mol})$	32.867	19.83
	R^2	0.549	0.649

Table 0-6: List of adsorption kinetic models.

Kinetic models	Equation
Pseudo-first order	$\ln(q_e - q_t)/q_e = -kt$
Pseudo-second order	$t/q_t = 1/h + t/q_e$ $h = k_2 q_e^2$
Elovich	$q_t = \frac{1}{\beta} \ln(\alpha\beta) + \frac{1}{\beta} \ln(t)$
Inert Particle Diffusion	$q_t = C + K_D t^{0.5}$

Table 0-7: A summary of the fitting parameters of As adsorption kinetic with LDH0.42-80-GO20.

Model	Parameters	As(III)	As(V)
Pseudo-first order	$q_e (\text{mg g}^{-1})$	-	38.8768
	$K (\text{min}^{-1})$	-	0.0017
	R^2	0.1519	0.6926
Pseudo-second order	$q_e (\text{mg g}^{-1})$	256.41	384.61
	$K (\text{g mg}^{-1} \cdot \text{min}^{-1})$	0.0002	0.0003
	R^2	0.9882	0.999
Diffusion	$C (\text{mg g}^{-1})$	248.15	328.04
	$K(\text{mg/g} \cdot \text{min}^{1/2})$	0.1058	1.6082
	R^2	0.0032	0.719

	$\alpha(\text{mg/g}\cdot\text{min})$	1.1479	14.39
Elovich	$\beta(\text{g mg}^{-1})$	244.18	283.01
	R^2	0.0071	0.928

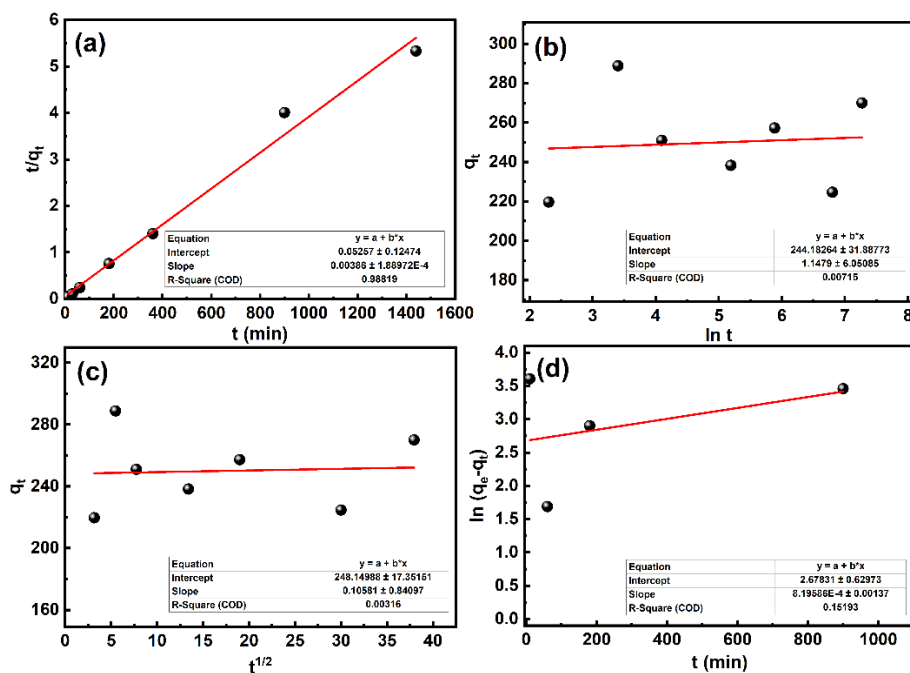


Figure 0-6: Fitting of As(III) adsorption kinetics of LDH0.42-80-GO20 with (a) pseudo second order, (b) Elovich, (c) intraparticle diffusion, and (d) pseudo first order models.

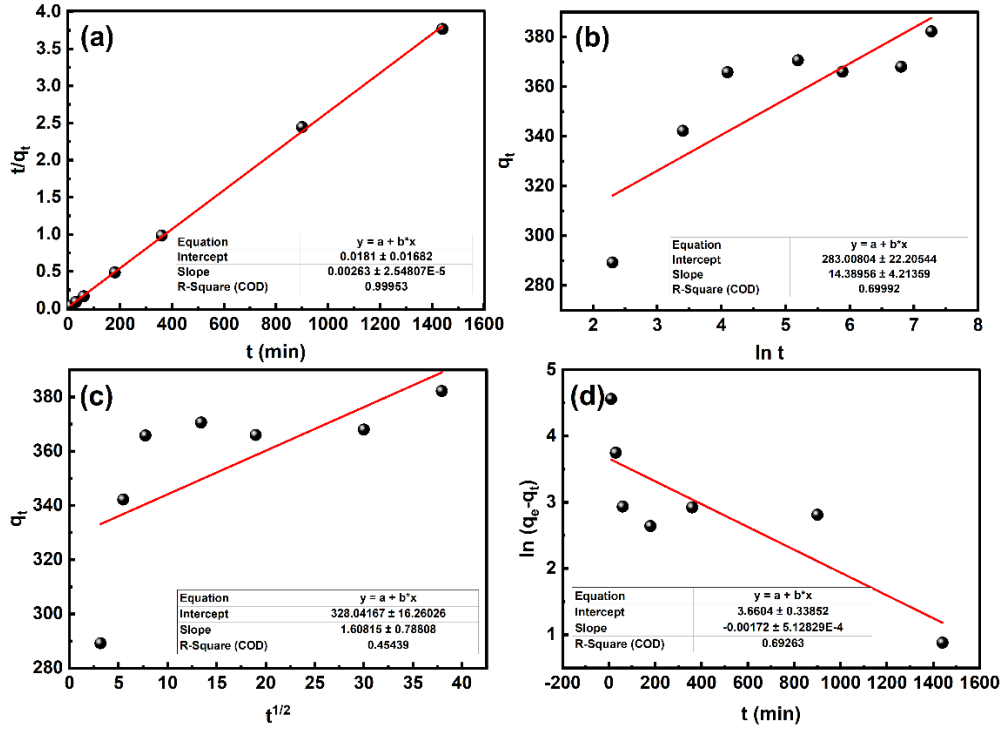


Figure 0-7: Fitting of As(V) adsorption kinetics of LDH0.42-80-GO20 with (a) pseudo second order, (b) Elovich, (c) intraparticle diffusion, and (d) pseudo first order models.

Table 0-8: Effects of interfering ions on the adsorption capacity of LDH0.42-80-GO20 for arsenic

Interfering ions	As(III) final concentration ($\mu\text{g L}^{-1}$)		As(V) final concentration ($\mu\text{g L}^{-1}$)	
	Without coexisting	With coexisting	Without coexisting	With coexisting
CO_3^{2-}	3.42	23.71	3.65	2.526
SO_4^{2-}		6.31		2.359
NO_3^-		4.661		1.658